Parameter Identification of Structural Systems Possessing One or Two Nonlinear Normal Modes

Sean O'Flaherty Fahey

Dissertation submitted to the Faculty of the Virginia Polytechnic Institute and State University in partial fulfillment of the requirements for the degree of

Doctor of Philosophy
in
Engineering Mechanics

Ali H. Nayfeh, Chair
Jean-Guy L. Béliveau
Muhammad R. Hajj
Daniel J. Inman
Liviu Librescu
Alfred L. Wicks

October 30, 2000
Blacksburg, Virginia

Keywords: Nonlinear dynamics, structural dynamics, building dynamics, vibration, modal analysis, line spectrum, signal processing, system identification

Parameter Identification of Structural Systems Possessing One or Two Nonlinear Normal Modes

Sean O'Flaherty Fahey

(ABSTRACT)

In this Dissertation, we develop, and provide proof of principle for, parameter identification techniques for structural systems that can be described in terms of one or two nonlinear normal modes. We model the dynamics of these modes by second-order ordinary-differential equations based on the principles of mechanics, past experience, and engineering judgment. We perform a number of separate experiments on a two-mass structure using several different types of excitation. For the linear tests, the theoretical system response is known in closed-form. For the nonlinear test, we use the method of multiple scales to determine second-order uniform expansions of the model equations and hence determine the approximations to responses of the structure. Then, we estimate the linear and nonlinear parameters by regressive fits between the theoretically and experimentally obtained response relations. We report deviations and agreements between model and experiment.

To the memory of my father Kevin Paul Fahey, Esq.

ACKNOWLEDGMENTS

I thank my parents Marilyn Gibby Machia and Kevin Paul Fahey, Esq. (Late) for all what they have given and instilled within me. I also thank my brother Jon Gibby Fahey (Jon X. Filthé) and the rest of my immediate family Larry T. Machia, Margaret Calaba Wardlaw, and Joelle, Julie, and Shaun for their generous and continuing support.

I thank my maternal grandparents Grace Hall Gibby and George S. Gibby for instilling within me a sense of God and an understanding of fair play. I thank the rest of the Gibbys for their consistent support. I thank my paternal grandparents Col. Paul V. Fahey and Virginia Goodrich Fahey (late), my Great Aunt Helen Goodrich Tynan, and my Great Uncle Julian Wayne Goodrich and his wife Patricia (late) for their contributions to my life through the years.

I thank my hometown friends Jason Schroeder, Michael Lantagne, David Treybal, Melanie Nunnick, Ingrid Hedbor, and the Hedbors for being there for me. I also thank the Faculty at the University of Vermont, in particular, Drs. Jean-Guy L. Béliveau, Dryver R. Huston (M.S.M.E. Advisor), Clarke Hermance (B.S.M.E. Advisor), John O. Outwater, Kenneth I. Gross, and Branimir F. von Turkovich for their encouragement from high school through the completion of my Doctorate.

I thank James Burke and Alec Allison, who were my technical mentor and engineering supervisor for my first job as an engineer with the Electric Boat Corporation. I also thank Matt King, Rene van Erven, Dennis Power, Mike Lotito, Kevin Detweiler, Jeff Cohen, David Pratt, Al Beebe and the Tech Aids, Tom Berry, Dr. Mark Bennett, Stu Dom, Randy Porterfield, Mike Coughlin, and the rest of the gang for making it an enjoyable experience.

I thank Drs. Conor D. Johnson, David A. Kienholz, and Eric H. Anderson, Eric M. Flint, and Karen Angell of CSA Engineering, Inc. for their efforts with regard to engineering employment on the other side of the Continent.

I thank my doctoral committee, Drs. Ali H. Nayfeh, Jean-Guy L. Béliveau, Muhammad R. Hajj, Daniel J. Inman, Liviu Librescu, and Alfred L. Wicks for their efforts. They each directly contributed significant and personal time, effort, and advise to the preparation of this Dissertation.

I owe a large debt of gratitude to Dr. Ali H. Nayfeh for serving as my doctoral advisor and for his strong encouragement to pursue my Doctorate. Without his encouragement, it is doubtful that I would have completed my Doctorate at this point in my life. On a personal note, I have found him to be a remarkable, compassionate, and fair man.

Dr. Béliveau served on the committee for my master's thesis and also introduced me to Virginia Tech through a joint project on the axial compression of rails with Dr. Thomas Murray of Civil Engineering. While at UVM, I also took courses dealing with dynamics and structures with Dr. Béliveau. Dr. Hajj and I worked together closely on several topics dealing with signal processing and dynamics. I also took courses dealing with signal processing and fluid dynamics with Dr. Hajj. Drs. Inman and Wicks helped finance and facilitate my efforts with the Virginia Tech booth at the International Modal Analysis Conference, including short *vacations* in Memphis and New Orleans. I also took courses dealing with signal processing and modal analysis from, and enjoyed many cups of coffee with, Dr. Wicks. Dr. Librescu offered a challenging course on the theory of plates and shells, which included many discussions.

I thank my contemporaries: at Virginia Tech Dr. Jon R. Pratt, Dr. Char-Ming Chin, Dr. Shafic Oueini, Dr. Ayman El-Badawy, Dr. Adel Jilani, Dr. Walter Lacarbonera, Dr. Randy Soper, Dr. Axinte Ionita, Dr. Eihab Abdel-Rahman, Dr. Haider N. Arafat, Dr. Joe N. Howard, Dr. Eric Austin, Silvio Alessandroni, Muhammad Al-Fayyoumi, Khaled Alhazza, Osama Ashour, Samir Emam, Waleed Faris, Jimmy Fung, Benjamin Hall, Ryan Krauss, Pramod Malatkar, Piergiovanni Marzocca, Ziyad Masoud, Sudip Mazumder, Nader Nayfeh, Tomoya Ochinero, Hanafy Omar, Maurizio Porfiri, Baha Suleiman, and Ilhan Tuzcu. My experience at Virginia Tech would not have been complete without them.

I owe special mention to Dr. Ali H. Nayfeh, Dr. Muhammad R. Hajj, Dr. Jean-Guy L. Béliveau, Dr. Char-Ming Chin, Dr. Jon R. Pratt, Sally Shrader, Jimmy Fung, Baha Suleiman, Waleed Feris, Piergiovanni Marzocca, and Margaret Calaba Wardlaw for their review of the various sections of this manuscript.

Thank you.

Sean O'Flaherty Fahey
Blacksburg, Virginia
October 30, 2000

Contents

List of Figures

List of Tables

Chapter 1

Introduction

1.1 Background and Motivation

The Romans employed impressive arches as integral parts of many civil structures, which have endured for two-thousand years or more [83]. Since Roman times, stress analysis has facilitated the sizing of structural members to their expected design loads. Material science has provided lighter materials that can withstand higher loads. An understanding of buckling phenomena has allowed for the creation of longer spans. Each of these *improvements* resulted from a continuing desire in the engineering sciences to optimize [32], go fast, push hard, design light, and reduce time to market. This desire has created *needs* within many engineering disciplines.

The ability to characterize the performance of structures in terms of mathematical models suitable for parametric study is of increasing importance. Practical performance constraints, such as limits on vibration response, acoustic output, load limits, and fatigue life considerations, create needs for dynamic characterizations from design conception through post production. Computer-aided engineering software can fulfill many of these needs at the onset by making powerful tools available to the engineering team. In contrast, dynamic testing serves to measure the success and failure of a design as it nears completion through analysis

of empirical observation. Once obtained, these results can be used to refine the analytic model, improve the product quality, reduce the time to market, and even flag unforseen difficulties.

Recently, the problem of parameter identification for structural dynamic systems has received considerable attention owing to the *need* to accurately describe and predict the response to various loading environments. Although the responses of many practical structural dynamic systems can be described and predicted via linear partial-differential, ordinary-differential, or algebraic equations[9, 13, 29, 31, 33, 55], there are also many physical phenomena that can not be modeled by linear means. These phenomena include subharmonic, superharmonic, combination, and ultrasubharmonic resonances; self-excited oscillations; jumps; saturation; nonlinear interaction among modes; bifurcations; and nonexistence of periodic responses to harmonic excitations. Briefly, some of the works that have illustrated a need for nonlinear considerations include [66] for ship motions, [27, 70] for machine-tool chatter, [8, 15] for aerospace structures, and [72] for machines and mechanisms; several others works are detailed throughout this text.

Ignoring the effects of relativity[14], the dynamics of structures are governed by Newton's laws[20, 34]. Often, we make a number of limiting assumptions about a system so that the mathematical description is tractable. For instance, in continuum mechanics, we ignore the molecular nature of matter and assume that it is continuous without gaps or holes[51]. For our purposes, a continuous-system description remains too complex because one needs an *infinite* number of degrees of freedom to *completely* describe the system dynamics. One avenue to achieve a useful dynamic characterization is the consideration of reduced-order, finite bandwidth, dynamic models that include only a finite number of degrees of freedom[77].

1.2 Scope

In this Dissertation, we develop and provide proof of principle for parameter identification techniques for structural systems that can be described in terms of one or two nonlinear

normal modes. We model these systems with second-order ordinary-differential equations based on the principles of mechanics, past experience, and engineering judgment. We perform a number of separate experiments on a two-mass structure using several different types of excitation. For the linear tests, the theoretical system response is known in closed-form. For the nonlinear test, we use the method of multiple scales to determine second-order uniform expansions of the model equations and hence the approximations to responses of the structure. Then, we estimate the linear and nonlinear parameters by regressive fits between the theoretically and experimentally obtained response relations. We report deviations and agreements between model and experiment.

1.3 Organization of the Dissertation

This Dissertation is divided into seven chapters and four appendices. The chapters contend with the essential concepts that are central to this work. The appendices contend with important concepts that are required in the overall development of this work, but would otherwise disrupt the flow or provide undue emphasis within a chapter.

We begin with Chapter 2 and estimate the linear system parameters for the first several structural modes of a two-mass structure via experimental observation of the free-decay system response and the system responses to an impact excitation and a base excitation. The results of a modal survey using an impact excitation are described, with a focus on determining the modal mass. We estimate the resonant frequencies, the linear damping factors, and the mode shapes from free-decay data. Then, we examine the forced response of the system to various levels of near-resonant base excitations. The results from the free-decay data and the near-resonant base excitations strongly suggest the presence of nonlinearities due to damping, stiffness, and inertia. Furthermore, the results suggest that the linear gyroscopic coupling among the modes is weak.

In Chapter 3, we begin our first serious examination of the nonlinear dynamics of the structure. The focus of this chapter is to establish the model order of several observed

linear and nonlinear resonances. If we examine the free decay of a linear system, the model order of the response signal is mathematically related to the number of modes involved in the response, excluding the special cases of repeated poles and unobserved dynamics and ignoring the sample rate, decimation, and numerical conditioning issues. If we examine the force response of a linear system to a sinusoidal excitation, then the model order of a single response signal is 2. If all of the modes are purely either in-phase or out-of-phase, the structure will have a single spatial basis function, which is a linear combination of the modes. If any of the modes has a relative phase delay, other than 0 or 180 degrees, the structure will have two spatial basis functions, each of which is a linear combination of the modes, which is the general linear case. For nonlinear systems, these issues are further complicated by harmonic distortion and modal interactions.

The spatial basis functions are not normal modes, in general. However, if we know the modes present within a frequency band and if we have *enough* spatial information, then we can decompose the spatial basis functions in terms of the normal modes, which are spatial basis functions themselves. We focus on the problem of determining the number of spatial basis functions of a response in addition to examining the problem of determining the model order of a signal. To accomplish this task, we utilize the method of principal component analysis (PCA).

In Chapter 4, we introduce a new closed-form decomposition technique for estimating the model parameters of an evenly sampled signal known to be composed of circular and hyperbolic sine and cosine functions in the presence of Gaussian white noise. The technique is closely related to Prony's method and hereditary algorithms that fit complex exponential functions to evenly sampled data. The circular and hyperbolic sine and cosine functions are obtained by adding constraints that limit the form of the characteristic polynomial coefficients. It avoids the leakage effects associated with the DFT for circular sine and cosine functions. When the signal contains frequency components that are not rational multiples of each other, the proposed decomposition yields amplitude and phase parameters that are more accurate than those obtained with the DFT, which is essential for the estimation procedures

of Chapters 5 and 6.

Characterizing the parameters of a nonlinear model of a system can be undertaken using a number of different methods. One approach involves iterating the parameters of a system of governing equations until data and model are in agreement [35]. This approach has the dual appeals that one works directly with the governing equations and the data. Another approach involves minimizing an objective function, such as a Euclidean norm, to obtain closed-form estimates. Approximate relationships involving the data and the governing equations are formed and solved in some least squares sense, either in the time-domain [56, 82, 86, 89, 90] or in the frequency-domain [87, 88]. This approach has the appeal that a solution is obtained in closed-form, although significant data manipulations are sometimes needed; for instance, simultaneous measures in terms of displacement, velocity, and acceleration are often required when only one form of response is available. A third approach involves estimating the Volterra kernels or higher-order frequency-response functions (FRFs) and subsequently uncovering the model parameters [47]. A problem with this method is that it is computationally expensive to estimate the Volterra kernels numerically and impractical from an experimental standpoint. The techniques described above do not require explicit emphasis of the nonlinearity. If the nonlinearity is not emphasized, a nonlinear estimation procedure will not generally provide good estimates, even if it is mathematically sound.

In Chapter 5, we advocate exploiting nonlinear resonances as an integral part of the estimation process, as proposed by Nayfeh [59]. We continue this work and describe a procedure for the identification of the nonlinear parameters of a single mode of a structure possessing quadratic and cubic geometric and inertia nonlinearities and linear (viscous), quadratic (airflow drag), and cubic damping. We use it to identify the parameters of the first mode of the two-mass structure. We sought and found a nonlinear phenomenon by exciting the structure near twice the natural frequency of its first mode. The generalized coordinate of this mode is modeled by a second-order ordinary-differential equation possessing quadratic and cubic geometric and inertia nonlinearities; linear, quadratic, and cubic damping; and parametric and external excitation terms. The linear natural frequency and damping coefficient have

been estimated using the linear tests described in Chapter 2, which serve as a check on the nonlinear identification procedure presented in this chapter. Here, the structure exhibits a behavior consistent with a combination of a principal parametric resonance and a subharmonic resonance of order one-half. We use the method of multiple scales [57, 58, 63, 65] to determine a second-order uniform expansion of the model equation and hence the response of the structure, also see [18, 19, 26, 41, 42]. We estimate the linear and nonlinear parameters by regressive fits of the theoretically obtained response relations to those obtained experimentally. We report deviations and agreements between model and experiment.

In Chapter 6, we advocate again the exploitation of nonlinear resonances as an integral part of the estimation process. We describe a procedure for the identification of the nonlinear parameters of two modes of a structure possessing quadratic and cubic geometric and inertia nonlinearities and linear and cubic damping. We use it to estimate the linear and nonlinear parameters of the first and second modes of a two-mass structure. We sought and found a nonlinear phenomenon by exciting the structure near the sum of the natural frequencies of the first and second modes. The generalized coordinates of these modes are modeled by two coupled second-order ordinary-differential equations possessing quadratic and cubic geometric and inertia nonlinearities; linear and cubic damping; and parametric and external excitation terms. A number of symmetries are utilized to simplify the governing equations by phrasing the generalized coordinates in terms of the mass-normalized modal coordinate system [60]. The essential concept of this chapter involves exploiting a combination resonance of the additive type to uncover the nature of the linear and nonlinear coupling parameters between the first and second modes. We use the method of multiple scales [57, 58, 60, 63, 65] to determine a second-order uniform expansion of the model equations and hence the response of the structure. We estimate the linear and cubic damping terms for each mode, the direct and parametric excitation terms for each mode, the linear gyroscopic coupling term between modes one and two, and the geometric and inertia quadratic and cubic stiffness terms involving modes one and two. We compare the estimated linear damping term of the first mode with those obtained in Chapters 2 and 5. Additionally, we compare the estimated external and parametric excitation coefficients and the cubic damping term with

those obtained in Chapter 5. These comparisons serve as checks on the procedure outlined in this chapter. We estimate the linear and nonlinear parameters by regressive fits between the theoretically obtained response relations and those obtained experimentally. We report deviations and agreements between model and experiment.

Chapter 2

Linear Parameter Identification

In this chapter, we estimate the linear system parameters for the first several structural modes of a two-mass structure via experimental observation of the free-decay system response and the system response to an impact excitation and a base excitation. The system consists of two *block* masses, a base, and two side beams. The system resembles a two-story building. Each block mass includes two end plates, a main mass, four 10-32 UNF cap screws, and a PCB J352C68 accelerometer. The overall mass of each of the block masses is $0.4714kg$. Additionally the top mass is instrumented with a PCB 352B33 accelerometer, which is not included in the mass measurement. The J352C68 accelerometers are shock-style accelerometers with integral ground isolation, labeled as "Response Accel No. 1" and "Response Accel No. 2" in Figure 2.1. The PCB 352B33 accelerometer is a low-mass accelerometer with an anodized aluminum casing, labeled as "Response Accel No. 3" in Figure 2.1. The overall dimension of each block mass is $105.4mm \times 30.0mm \times 20.0mm$. The main masses, end plates, and cap screws are made of low-carbon steel. The main mass has two shallow grooved channels for positioning of the side beams. The side beams are sandwiched between the main mass and the end plates and secured with two cap screws per end plate. The PCB J352C68 accelerometers are then studded to one of the end plates. The base has the same general design as the block masses, except for two recessed milled holes, which are used to bolt it to the reaction mass. The side beams have a cross-section of $12.70mm \times 0.810mm$

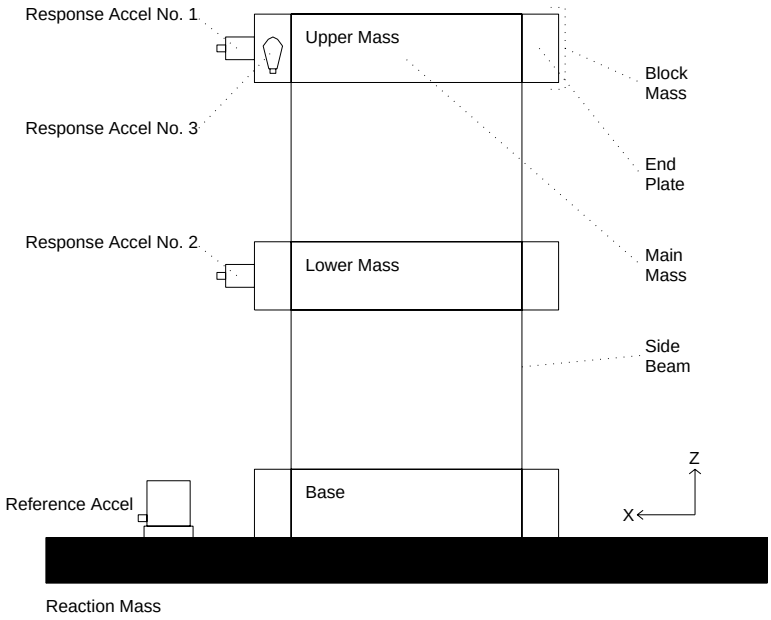

Figure 2.1: A diagram of the two-mass structure

and are manufactured from oil-hardened tool steel. Each of the distances between the upper mass and lower mass and lower mass and base is $70.0mm$. Finally, the two-mass structure is bolted to a large reaction mass, which is fixed to the armature of a $4000N$ electro-mechanical shaker. The final assembly is illustrated in Figures 2.1 and 2.2.

In Section 2.1, we describe the results of a modal survey using an impact excitation, with a focus on determining the modal mass. In Section 2.2, we estimate the resonant frequencies, the linear damping factors, and the mode shapes of the first three modes from free-decay data. In Section 2.3, we examine the forced response of the system to various levels of near-resonant base excitations. A summary of the results is provided in Section 2.4.

2.1 Modal Survey via Impact Tests

In this section, we describe a modal survey of the structure using an impact excitation. Three accelerometers are attached to the structure in order to measure the structural response.

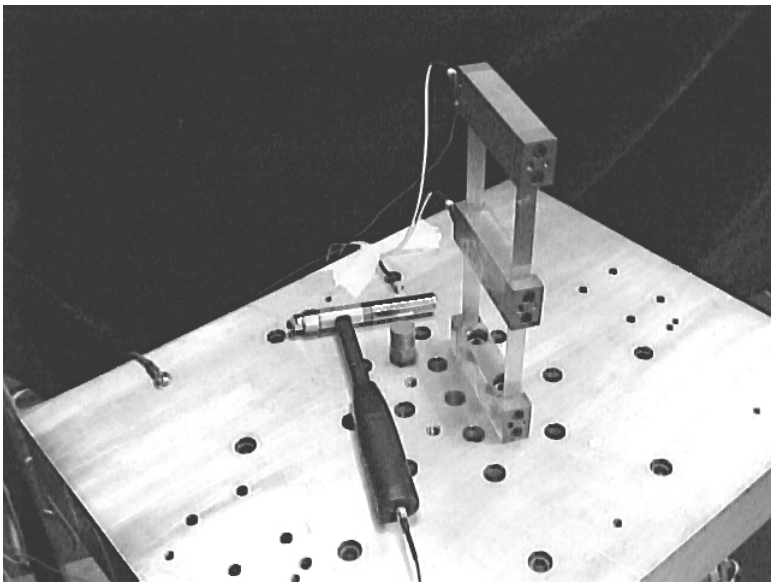

Figure 2.2: A picture of the two-mass structure

Table 2.1: Accelerometer locations - the X,Y, and Z provide the position and the U,V, and W provide the orientation in Cartesian coordinates

Response Name	X	Y	Z	U	V	W
uprx+	52.7 mm	0 mm	215 mm	1	0	0
lorx+	52.7 mm	0 mm	115 mm	1	0	0
upry+	46.3 mm	10 mm	215 mm	0	1	0

The accelerometer locations are documented in Figures 2.1 and 2.2 and Table 2.1. Then, an instrumented hammer is *roved* to the various reference locations documented in Table 2.2. To maintain the response within a linear range, we choose as reasonably as possible light hammer impacts. This type of testing procedure is known as a roved impact test. A four-channel spectrum analyzer is used for data acquisition and for calculating the frequency-response functions (FRFs). To display the mode shapes, we utilize the Betti-Maxwell reciprocity principle and switch the reference and response indices for analysis purposes [4].

Table 2.2: Impact Locations - the X,Y, and Z provide the position and the U,V, and W provide the orientation in Cartesian coordinates

Reference Name	X	Y	Z	U	V	W
uplx+	-52.7 mm	0 mm	215 mm	1	0	0
uply+	-46.3 mm	-10 mm	215 mm	0	1	0
uprx-	52.7 mm	0 mm	215 mm	-1	0	0
upry+	46.3 mm	-10 mm	215 mm	0	1	0
lolx+	-52.7 mm	0 mm	115 mm	1	0	0
loly+	-46.3 mm	-10 mm	115 mm	0	1	0
lorx-	52.7 mm	0 mm	115 mm	-1	0	0
lory+	46.3 mm	-10 mm	115 mm	0	1	0
baly+	-46.3 mm	-10 mm	15 mm	0	1	0
bary+	46.3 mm	-10 mm	15 mm	0	1	0

A *composite* FRF is provided in Figure 2.3. This composite FRF is the power average of all of the FRFs. It clearly shows five distinct resonant peaks near 12, 33, 39, 221, and 282 Hz. In the following section, it is shown that these resonant peaks correspond to the first five structural modes.

2.1.1 Modal Analysis

From the FRFs, the impulse-response functions (IRFs or Markov parameters) are calculated via the inverse discrete Fourier transform. Then, the eigensystem realization algorithm [33] (or the Ho-Kalman algorithm [29]) is used to decompose the IRFs into a minimum state-space realization $[A, B, C, D]$ in terms of accelerance. Details of the Ho-Kalman algorithm and the eigensystem realization algorithm are provided in Appendix A, which also explains the meaning of the notation used in the remainder of this chapter. For our purposes, A represents the poles of the system in the z-plane in diagonal form, B represents the initial modal amplitudes, C represents the mode shapes, and D represents the initial pulse amplitudes.

For receptance and mobility, D does not need to be included. However, for accelerance, it needs to be included because the accelerance IRFs generally contain an initial pulse response.

In Figures 2.4 and 2.5, two characteristic examples of the realized parameters are overlayed with the original FRFs. In Figure 2.4, the fit and data are generally in good agreement. The coherence is generally good, except near 221 Hz, which corresponds to the third-mode resonant frequency. The modal contributions of the third mode at "uprx+" and "uplx+" are small and sensitive to the variations involved with impact testing.

In Figure 2.5, the fit and data are generally in good agreement, except below 20 Hz and near 140 Hz. In the neighborhood of 20 Hz, there is a poorly developed and unestimated mode that is believed to be a rigid-body mode of the shaker assembly; however its effect on the overall response is considered to be small. Here, it is noticeable because of the antiresonant behavior of the test object. In the neighborhood of 140 Hz, the phase and amplitude of the antiresonance do not match the curve fit with a high degree of accuracy. It is apparent from the phase and amplitude that there is a minor mode near 145 Hz. We have no explanation for this apparent mode; however its effect on the overall response is considered to be small. In Figure 2.5, the coherence is generally good, except below 20 Hz, near 140 Hz, and near 280 Hz, which correspond to the antiresonant regions. The overall data quality is considered to be good. The overall agreement between the data and curve fits is good.

The mode shapes C for the first five structural modes are illustrated in Figures 2.6 through 2.10. The first two modes are lateral modes in the X-direction. The first mode has a small translational component in the Y-direction. The third and fifth modes are lateral modes in the Y-direction. The fourth mode is a torsional mode about the Z-direction. In Figure 2.6-2.10, we observe that each of the first five modes is nearly orthogonal to the excitation in the Z-direction.

The auto-modal assurance criterion is provided in Figure 2.11 [1]. The largest off-diagonal component is 0.01128. This demonstrates good self-orthogonality of the modes. However, the modes are not in general self-orthogonal, rather they are orthogonal relative to the system's

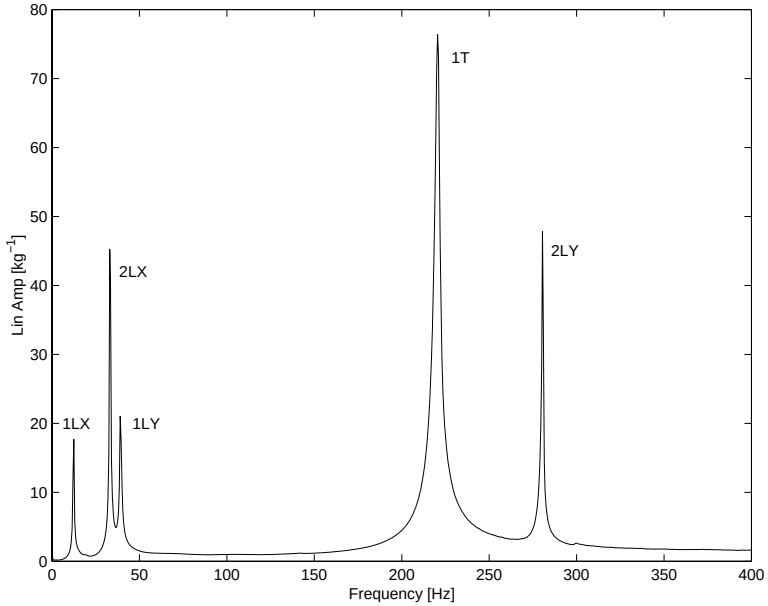

Figure 2.3: A composite frequency-response function, which is the power average of the experimentally obtained FRFs

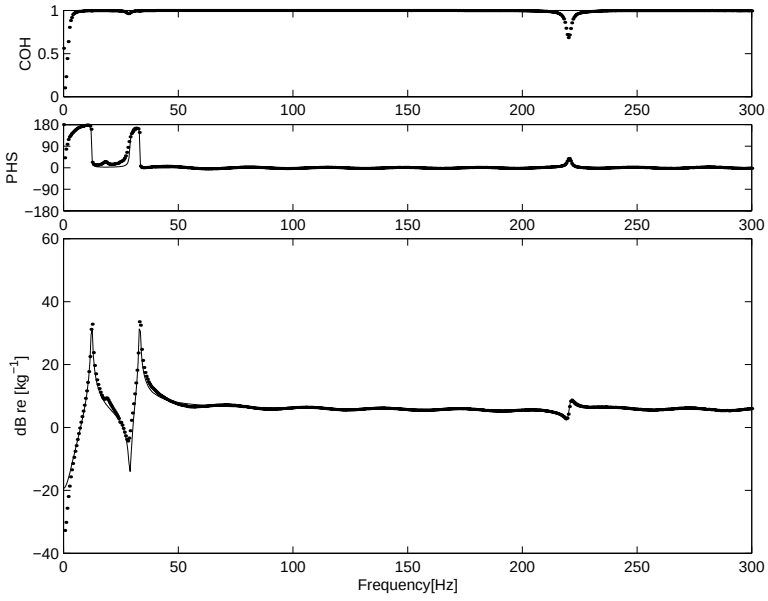

Figure 2.4: A frequency-response function uprx+/uplx+ '.' versus its fit '-': an example in the X-direction

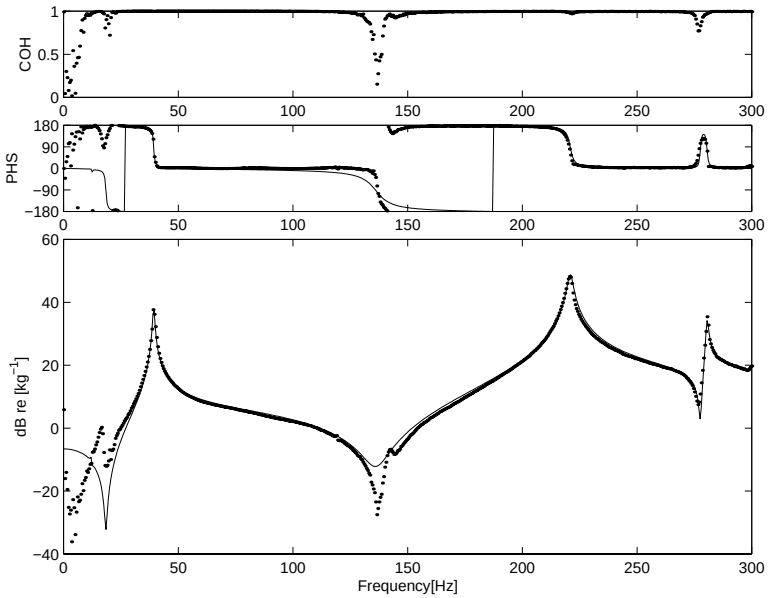

Figure 2.5: A frequency-response function '.' versus its fit '-': an example in the Y-direction

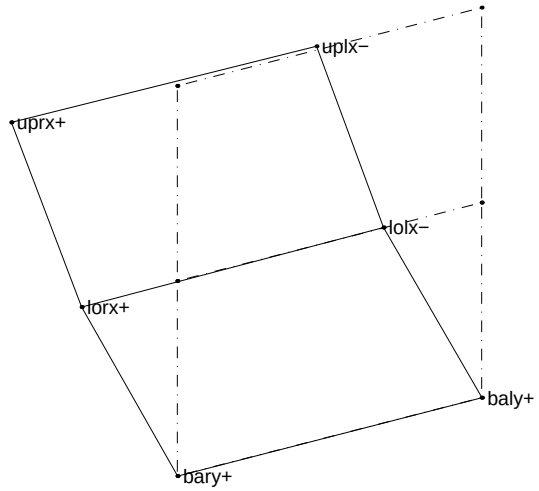

Figure 2.6: First mode near 12 Hz; first lateral mode in the X-direction

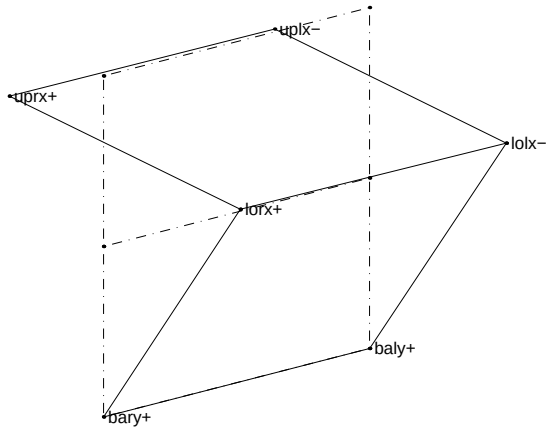

Figure 2.7: Second mode near 33 Hz; second lateral mode in the X-direction

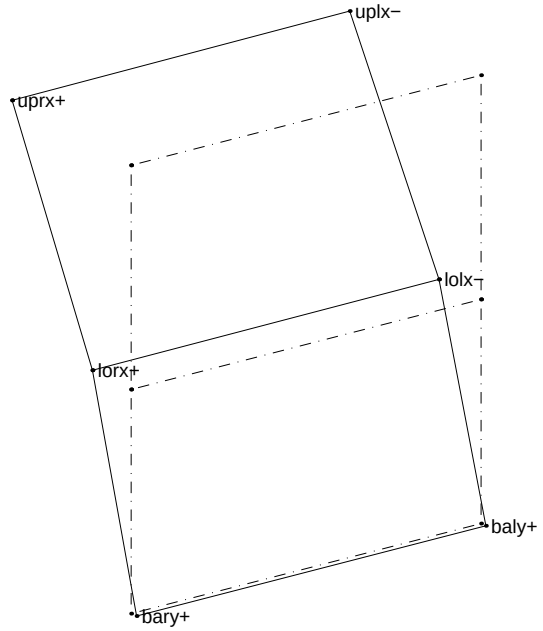

Figure 2.8: Third mode near 39 Hz; first lateral mode in the Y-direction

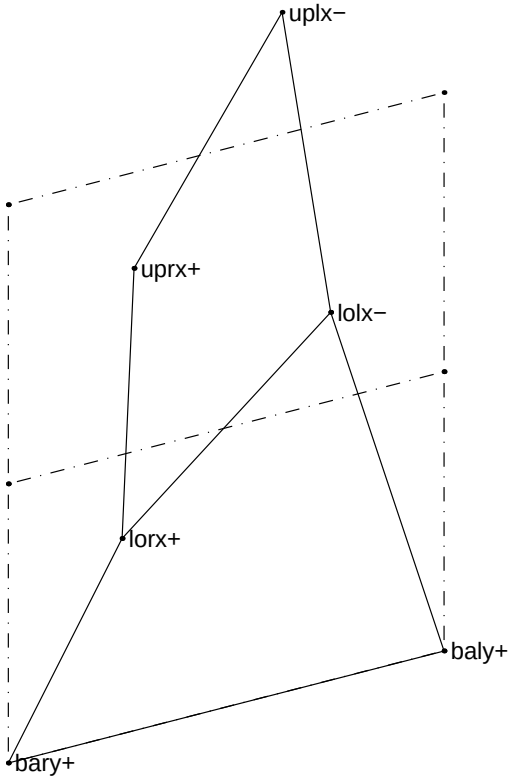

Figure 2.9: Fourth mode near 221 Hz; first torsional mode about the Z-direction

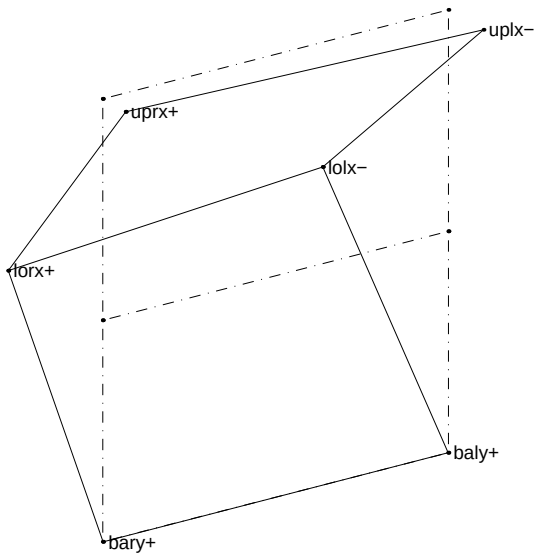

Figure 2.10: Fifth mode near 281 Hz; second lateral mode in the Y-direction

mass. This *suggests* that our choice of the impact locations are reasonably representative of the involved mass.

2.1.2 Modal Mass Calculation

In Chapter 6, we utilize several symmetries in the nonlinear stiffness terms, which are detailed in that chapter. To take advantage of these symmetries, we need to decompose the system response in terms of the mass-normalized normal modes. Unfortunately, our primary testing method, namely a base excitation, contains only measures in terms of time and length (via acceleration); no measures of either force or mass are available. But, the impact test involves units of time, length (via acceleration), and mass (via force). Hence, we need to estimate the modal mass with impact testing.

We focus on the first two structural modes. But, the *closeness* of the frequency of the third mode to that of the second mode requires continued attention. However, the resonant

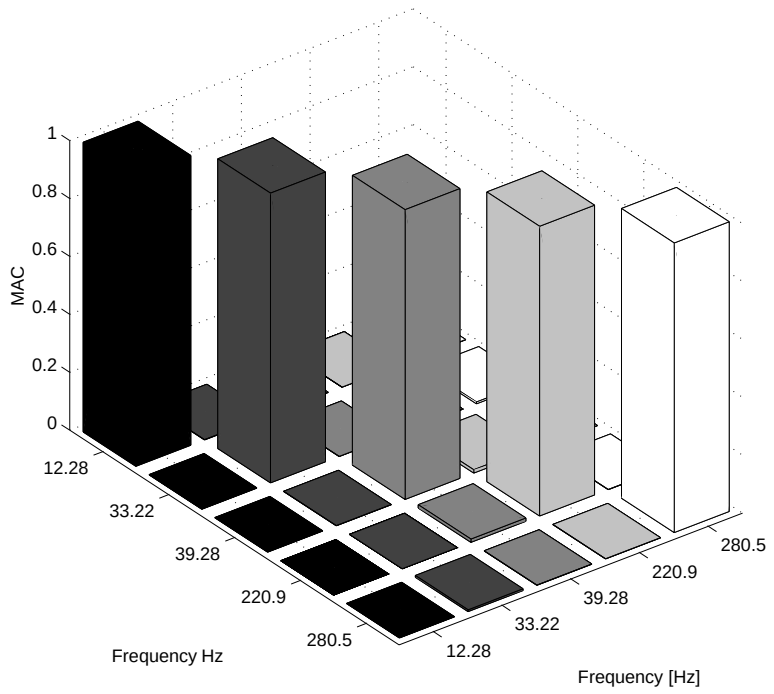

Figure 2.11: Auto- modal assurance criterion of the first five modes

frequencies of modes four and five are more than five times the resonant frequencies of the first three structural modes. Thereby, we ignore the effects of modes four and five because their resonant frequencies are well separated from the frequency band of interest. We will return to this point and provide additional justification in the next chapter on model order.

According to the linear modal model, the residues for receptance are

$$A_{pqr} = \frac{1}{2j\omega_r\sqrt{1-\zeta_r^2}}\tilde{\Phi}_{pr}\tilde{\Phi}_{qr}Q_r \tag{2.1}$$

where p, q, r, ω_r, ζ_r, $\tilde{\Phi}_r$, and Q_r are the response index, the reference index, the mode index, the damped natural frequencies, the linear damping ratios, the mode shapes, and the modal participation factor, respectively [17]. The so-called modal participation factor $Q_r = 1/M_r$ is the reciprocal of the modal mass.

Clearly, the modal mass depends on the choice of the scaling for the mode shapes. As detailed above, we desire to scale the mode shapes with respect to the modal mass [55]. However, at this juncture, the modal mass is not known. Hence, we need to choose an

alternate scaling of the mode shapes, such as

$$\sum_p \tilde{\Phi}_{pr}^2 = 1 \tag{2.2}$$

To avoid confusion about which scaling rule is being used, Φ denotes the mass-normalized mode shapes and $\tilde{\Phi}$ denotes the mode shapes normalized according to Equation (2.2).

The scaling among the state-space matrices is arbitrary, which are defined in Appendix A. Clearly, if $[A, B, C, D]$ is a state-space realization, then $[N^{-1} \times A \times N, N^{-1} \times B, C \times N, D]$ is another applicable state-space realization, when n has full rank.. Hence, we need to select a scaling of the state-space parameters that ensures that the mode shapes C conform with Equation (2.2). Additionally, we need to modify the form of the response from accelerance to receptance so that we can utilize Equation (2.1). The accelerance residues can be formed from the state-space parameters as

$$A_{pqr} = C(p, r)B(r, q) \tag{2.3}$$

Since the $C(p, r)$ are the mode shapes for a diagonal A, we introduce the diagonal scaling matrix N such that

$$A_{pqr} = C(p, r)N(r, r)^{-1}N(r, r)B(r, q) \tag{2.4}$$

and

$$C_{new} = C_{old}(p, r)N(r, r)^{-1} \tag{2.5}$$

$$B_{new} = N(r, r)B_{old}(r, q) \tag{2.6}$$

where $\tilde{\Phi} = C_{new}$ satisfies Equation (2.2). Then, the state-space realization $[A, B, C, D]$ in terms of accelerance is modified to an equivalent form in terms of receptance $[A, B, C]$. From Appendix B, we can rescale A_{pqr}. However, holding C fixed results in scaling B alone.

Subsequently, equating the right-hand sides of Equations (2.1) and (2.3), replacing $C(p, r)$ with Φ_{pr}, and performing some algebraic manipulations, we have

$$M_r = \frac{1}{2j\omega_r\sqrt{1-\zeta_r^2}}\frac{C(q, r)}{B(r, q)} \tag{2.7}$$

Table 2.3: Modal mass estimates

Reference Name	Mode One	Mode Two	Mode Three
uplx-	0.528 kg	0.570 kg	N/A
lolx-	0.518 kg	0.526 kg	N/A
upry+	N/A	N/A	0.523 kg
Average	0.523 kg	0.548 kg	0.523 kg

Since we have three references q, Equation (2.7) provides three independent estimates of the modal mass. However, modes one and two are nearly orthogonal to the reference in the Y-direction, and mode three is nearly orthogonal to the references in the X-direction. Therefore, we drop these estimates from our analysis, because we expect them to be poorly conditioned due to the problem of a small devisor. The averaged results are provided in Table 2.3. In general, the estimated modal mass appears to be consistent with the actual measured mass of the system; that is, we would obtain a similar result with an analytic model.

In the following sections, we significantly increase the response amplitude to emphasize the nonlinearity. We explore the apparent dependence of the damping and the response amplitude on the amplitude of excitation.

2.2 Free-Decay Tests

In this section, we estimate the frequencies, damping factors, and mode shapes of the first three modes using a so-called sliding window and the Eigensystem Realization Algorithm. The two-mass structure is impacted or plucked to provide finite initial conditions. The free-decay response is then acquired. The signal is sampled at a rate of 256 Hz and the data acquisition system limits the spectral content with a 100 Hz low-pass filter. Seven free-decay events with differing initial conditions are obtained.

In Figure 2.12, a typical free-decay time series is illustrated. We segment each of the time

series into several ensembles. The first ensemble begins at the start of the decaying part of the time series. The last ensemble is chosen such that the mean modal amplitudes are at least $2m/s^2$, which is intended to ensure that the parameter estimates are not unreasonably biased by noise [67]. In the current configuration, the noise floor is largely driven by Response Accel No. 3, which has a noise source of approximately $0.15m/s^2$, which is consistent with its rate resolution. Each of Response Accel No. 1 and Response Accel No.2 has a noise level of about $0.05m/s^2$, which is higher than their rated resolutions and is most likely due to environment factors. The ensemble length is selected to be 0.375 seconds with an overlap of 33%.

The frequency and damping estimates of the ensembles for modes one, two, and three are plotted against their mean modal amplitudes in Figures 2.13, 2.14, and 2.15, respectively. The frequency and damping estimates are provided in terms of the real and imaginary parts of the modal poles. The modal poles can be expressed as

$$\{\lambda_r, \lambda_r^*\} = -\zeta_r\omega_r \pm j\omega_r\sqrt{1-\zeta_r^2} \tag{2.8}$$

where

$$\begin{aligned}
\zeta_r &= \text{critical damping ratio} \\
\omega_r &= \text{natural frequency} \\
-\zeta_r\omega_r &= \text{damping factor} \\
\omega_r\sqrt{1-\zeta_r^2} &= \text{damped natural frequency}
\end{aligned}$$

and

$$\begin{aligned}
\omega_r &= \sqrt{\text{real}(\lambda_r)^2 + \text{imag}(\lambda_r)^2} \\
\zeta_r &= -\frac{\text{real}(\lambda_r)}{\sqrt{\text{real}(\lambda_r)^2 + \text{imag}(\lambda_r)^2}}
\end{aligned}$$

There are clear trends in the frequency and damping estimates. In Figure 2.13, the damping of the first mode increases with increasing modal amplitude, which is consistent with a

nonlinear damping mechanism. In Figure 2.13, the first-mode frequency decreases with increasing modal amplitude, which is consistent with a softening stiffness. Here, we note that the decrease in the damped linear natural frequency due to the increase in damping would only account for about a 0.003Hz shift in the damped natural frequency of the first mode, which is significantly less than the frequency shift observed in Figure 2.13. In Figure 2.14 and 2.15, the same qualitative trends of increasing damping and decreasing frequencies are clearly observable for modes two and three.

It is difficult to establish from Figures 2.13-2.15 what the linear damping factors and damped natural frequencies should be. The frequency and damping estimates also have noticeable variances. To estimate the linear (or at least linearized) frequency and damping estimates, we should utilize the redundancy of our estimates and also remove the amplitude dependent trend. Our intention is to estimate the damping factors and damped natural frequencies as the response level approaches zero. In practice, we often estimate the damping and frequency using a very low level of excitation and declare it equal to the linear damping and frequency. Here, we clearly see that the damping and frequency estimates associated with the smallest modal amplitudes are far away from zero-response amplitude to simply declare them as linear. At this juncture, the next best thing is to examine the frequency and damping estimates associated with the smallest response amplitudes and project back onto zero-response amplitude. For simplicity, we form a straight-line regressive fit through the frequency and damping estimates and obtain the intercepts and slopes given in Table 2.4. Consequently, the linear frequency and damping parameters can be represented by the intercepts. The standard deviations about the regressive fits are also provided in Table 2.4. In Chapter 5, we find that the damping mechanism for the first mode is best described by linear and cubic damping terms. Hence, this approach of estimating the linear damping is not quite correct, at least in a rigorous sense.

In Figures 2.13-2.15, the variances of the frequency and damping estimates appear to increase with increasing modal amplitude. In other words, our frequency and damping estimates have a divergent character for large modal amplitudes. Perhaps, for these larger modal

Table 2.4: Straight-line frequency and damping estimates

Mode Number	Frequency Intercept [Hz]	Frequency Slope [Hz-s^2/m]	Frequency STD [Hz]	Damping Intercept [Hz]	Damping Slope [Hz-s^2/m]	Damping STD [Hz]
1	12.419	-0.0199	0.0197	-0.0456	-0.0104	0.0133
2	33.319	-0.0089	0.0187	-0.0472	-0.0037	0.0055
3	39.305	-0.0139	0.0519	-0.0858	-0.0052	0.0240

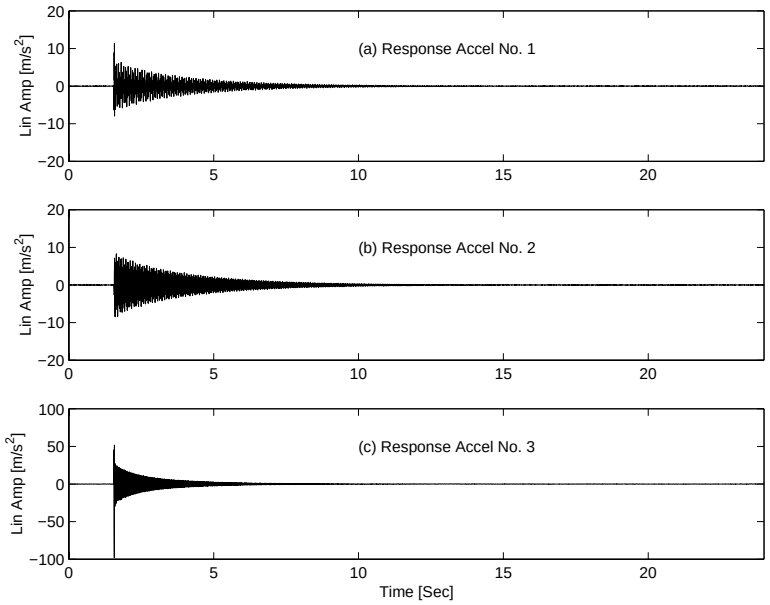

Figure 2.12: Typical free-decay time series

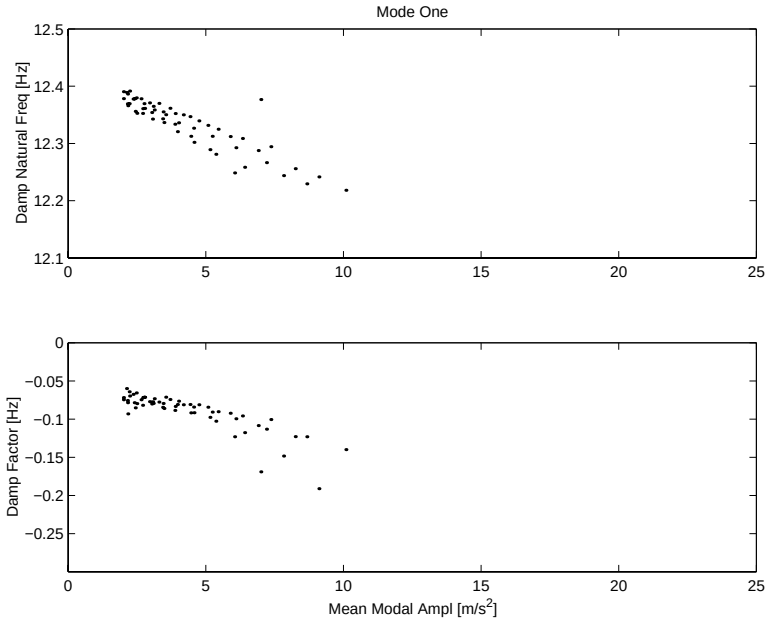

Figure 2.13: Frequency and damping estimates for mode one using ERA

amplitudes, our method of estimating the frequency and damping parameters oversimplies the dynamics of the system!

In Figures 2.16-2.18, the various mode-shape estimates are shown in the complex plane. They are closely clustered and are labeled with their respective response locations, as described in Table 2.1. We note that the mode-shape estimates can not be statistically distinguished as being away from the real line. In fact, there is only one mean imaginary component that is not within a standard deviation of the real line. Furthermore, the mode shapes appear to remain constant with respect to the response amplitude.

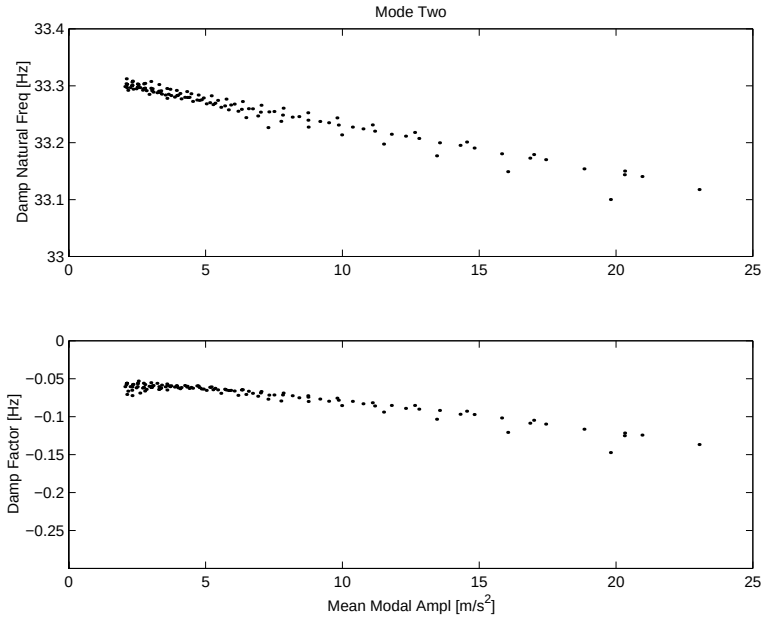

Figure 2.14: Frequency and damping estimates for mode two using ERA

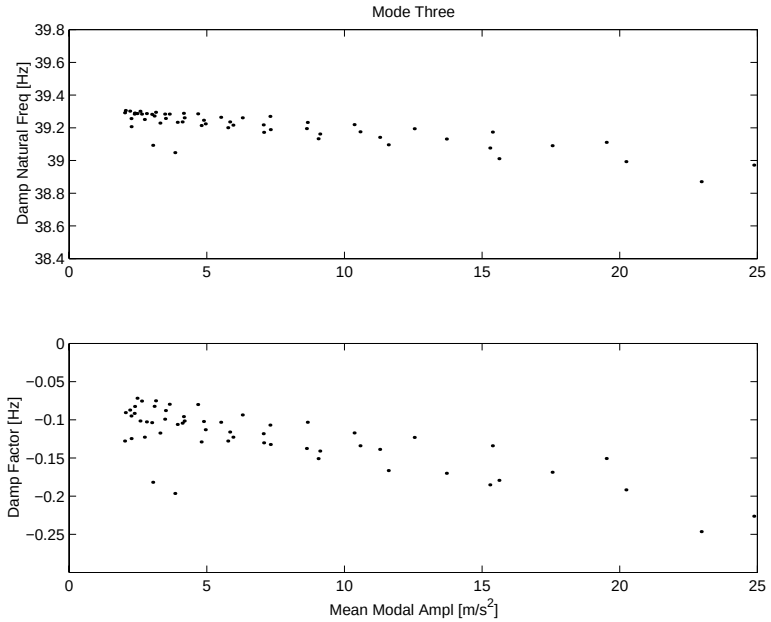

Figure 2.15: Frequency and damping estimates for mode three using ERA

Table 2.5: Mode-shape estimates from the eigensystem analysis

Mode Number	Response Location	Real Mean	Real STD	Imag Mean	Imag STD
1	uprx+	0.8391	0.0065	-0.0008	0.0205
	lorx+	0.5305	0.0066	-0.0031	0.0150
	upry+	-0.1207	0.0681	-0.0002	0.0300
2	uprx+	-0.5329	0.0056	0.0062	0.0156
	lorx+	0.8460	0.0036	-0.0089	0.0219
	upry+	0.0169	0.0205	0.0256	0.0124
3	uprx+	0.0076	0.0080	0.0030	0.0088
	lorx+	-0.0120	0.0107	-0.0007	0.0052
	upry+	0.9999	0.0009	-0.0033	0.0132

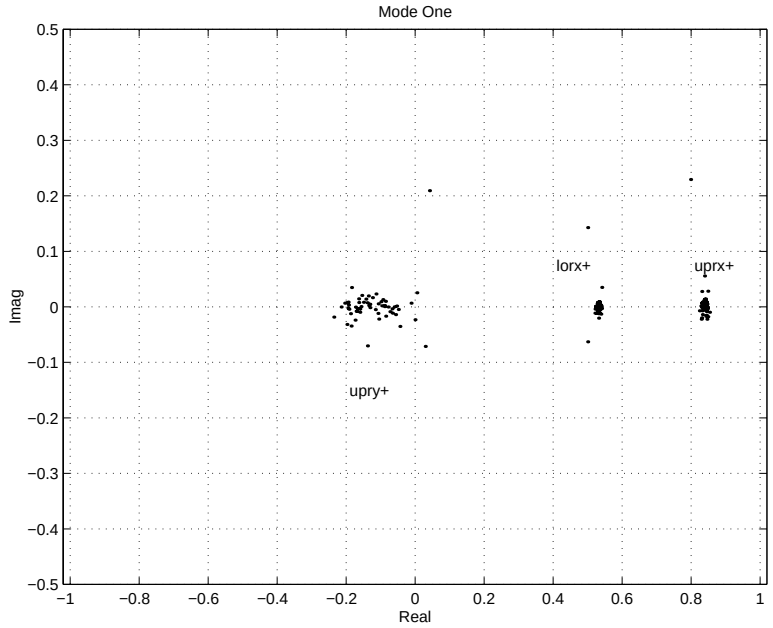

Figure 2.16: Complex mode-shape estimates for mode one using ERA

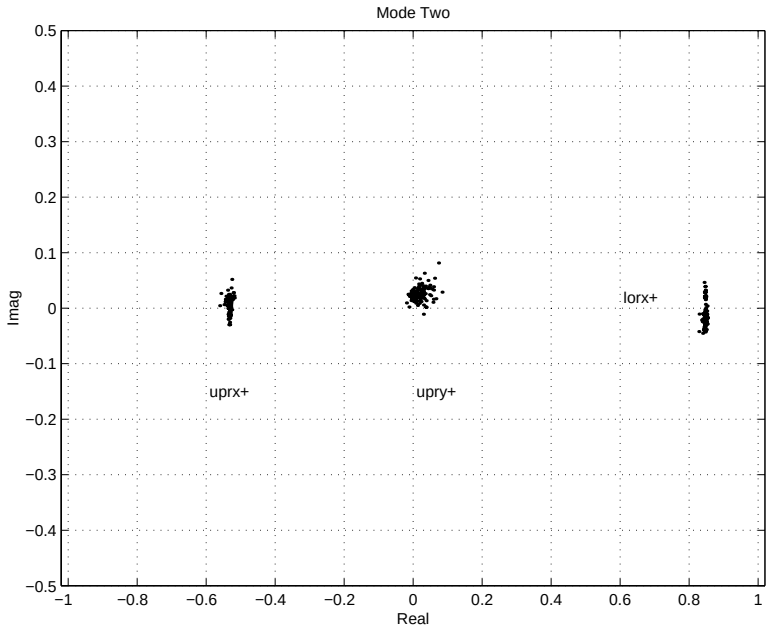

Figure 2.17: Complex mode-shape estimates for mode two using ERA

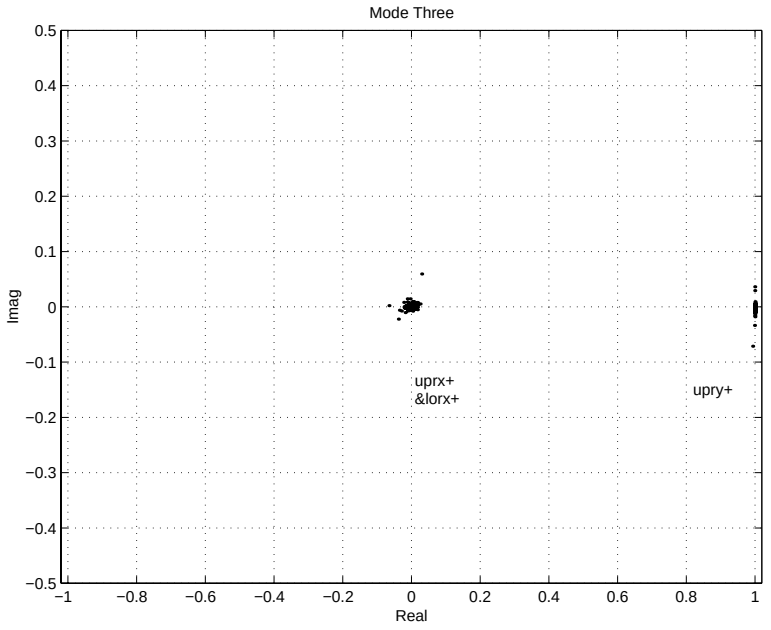

Figure 2.18: Complex mode-shape estimates for mode three using ERA

The real and complex mean values and standard deviations for the mode-shape estimates are provided in Table 2.5. Hereon, we take the mode shapes as the mean values of the real parts of the mode-shape estimates provided in Table 2.5. Essentially, we are justifying a normal mode assumption through the observation that the imaginary parts of the mode-shape estimates are not statistically different from zero [1]. In the following section, we examine the primary-resonance amplitude response as a function of the excitation amplitude.

2.3 Base Excitation Tests

In this section, we detail the response of the two-mass structure to varying levels of swept-sine base excitations. The structure is excited in the vertical direction, which is nearly orthogonal to each of the first three modes. However, asymmetries due to manufacturing defects, initial curvature, and installation of the instrumentation cause a small component of direct excitation, which is estimated using the nonlinear parameter estimation technique of Chapter 5.

We excite the structure in the five so-called events documented in Table 2.6. Events A, B, C, and D are intended to quantify the dependence of the excitation amplitude on the response amplitude. We compare Events E and D in order to check for possible nonlinear jump phenomena or the coexistence of multiple solutions.

In Figures 2.19-2.21, we show the frequency-response curves of the structure to a primary-resonance excitation with varying levels of excitation. The free-decay results suggested that the first three modes exhibit a softening stiffness nonlinearity. In the swept-sine data, the frequency-response curves consistently bend more to the left as the level of the excitation

[1] Had the imaginary part been statistically different from zero, we would have needed to find normal mode shapes that diagonalize the mass and stiffness matrices alone. Then, we would have needed to uncover a *damping* matrix that includes damping coupling terms. The damping coupling terms couple the normal modes, resulting in so-called complex modes. In the nonlinear system examination of Chapter 6, the damping coupling terms are included. The damping coupling terms are not emphasized by impact or free-decay data; but they may be, or may not be, emphasized by nonlinear resonances.

Table 2.6: Events for swept-sine tests via base excitation

Event Letter	Sweep Direction	Excitation Amplitude
A	Up	$0.1g$
B	Up	$0.2g$
C	Up	$0.5g$
D	Up	$1.0g$
E	Down	$1.0g$

increases for each of the first three modes, which is consistent with the free-decay results. Hence, one speaks of a softening stiffness nonlinearity for the first three modes. Had the frequency-response curves bend more to the right with increasing excitation level, we would have concluded a nonlinear hardening effect.

In Figures 2.19-2.21, we overlay the frequency-response curve to a base excitation of $1.0g$ and 10 times the frequency-response curve to a base excitation of $0.1g$. Clearly, the peak response amplitude due to the base excitation of $1.0g$ is significant less than 10 times the peak response amplitude due to the base excitation of $0.1g$. This is consistent with a nonlinear damping effect, see [41].

Table 2.7 compares the observed reduction in the peak response from a linear case. The observed behavior is qualitatively similar to the results obtained from the free-decay data. Additionally, Table 2.7 compares the anticipated level of damping from the free-decay straight-line damping analysis for the cases of $0.1g$ and $1.0g$ base excitation, from the slope and intercept of Table 2.4, with those calculated using the peak modal amplitude. If the damping of a linear system is increased and if the other system parameters are not changed, then the reduction in the peak response amplitude should be nearly proportional to the inverse of the change in damping. The inverse of the ratio of the anticipated damping and the ratio of the observed peak amplitudes are provided in the right-hand column of Table 2.7. Although there are differences between the ratios of the observed peak amplitudes and

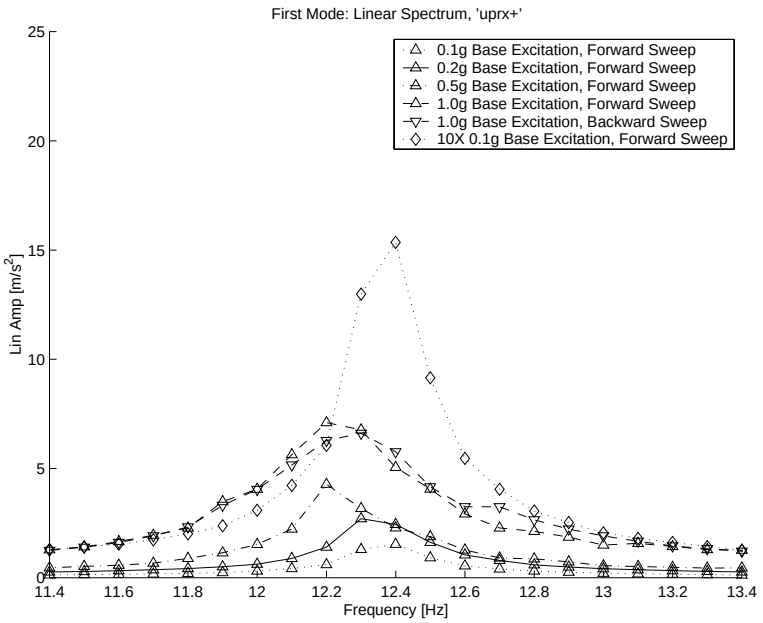

Figure 2.19: Frequency-response curves of the first mode for varying levels of base excitation

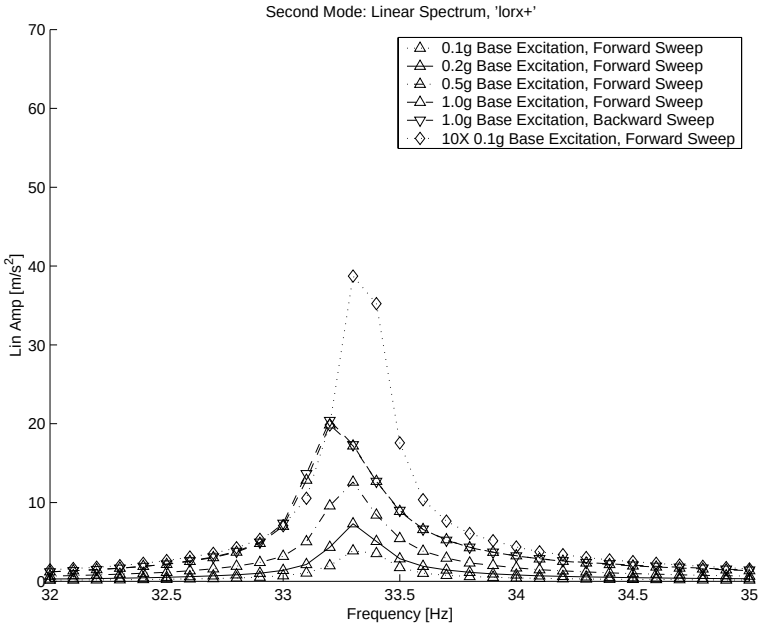

Figure 2.20: Frequency-response curves of the second mode for varying levels of base excitation

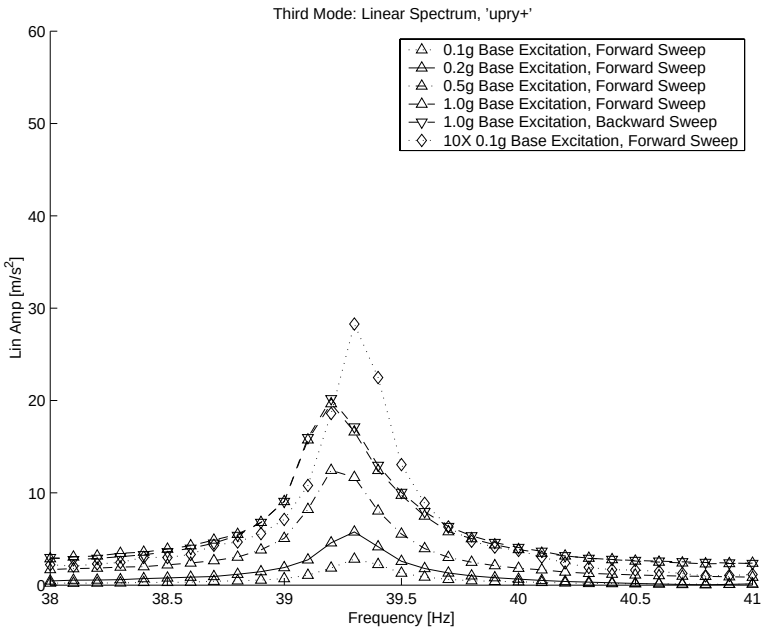

Figure 2.21: Frequency-response curves of the third mode for varying levels of base excitation

the inverse ratios of the anticipated damping, they are the same order of magnitude and have the same general trend. When examining Table 2.7, however, one should keep in mind that the assumptions involved in estimating the anticipated level of damping are oversimplified, that the observed peak response amplitude is not the peak response amplitude, that the form of excitation is different, and the system is not linear.

2.4 Summary

In Section 2.1, we obtain an estimate of the modal mass. In Section 2.2, we obtain estimates of the linear modal damping factors and damped natural frequencies. Additionally, we obtain averaged estimates for the self-normalized mode shapes and establish that a normal mode approximation is appropriate. Next, we estimate the mass-normalized mode shapes and the

Table 2.7: Amplitude and damping ratios

Mode Number	Response Location	10X Peak Primary Resonance Amplitude $0.1g$ Base $[m/s^2]$	Peak Primary Resonance Amplitude $1.0g$ Base $[m/s^2]$	Ratio of the Primary Resonance Amplitudes
1	uprx+	15.35	6.61	0.4306
2	lorx+	38.72	20.40	0.5269
3	upry+	28.28	20.18	0.7136
Mode Number		Anticipated Free-decay ERA Sliding-window Damping Factor $0.1g$ Base [Hz]	Anticipated Free-decay ERA Sliding-window Damping Factor $1.0g$ Base [Hz]	Inverse Ratio of the Free-decay ERA Sliding-window Damping Factors
1		-0.0640	-0.1250	0.5120
2		-0.0659	-0.1343	0.4907
3		-0.0891	-0.1759	0.5065

effective dynamic matrices. It follows from the modal model that

$$\left[\tilde{\Phi}\right]^T [m] \left[\tilde{\Phi}\right] = [\backslash M_r \backslash] \tag{2.9}$$

$$[\Phi]^T [m] [\Phi] = [I] \tag{2.10}$$

$$[\Phi]^T [c] [\Phi] = [\backslash 2\zeta_r \omega_r \backslash] \tag{2.11}$$

$$[\Phi]^T [k] [\Phi] = \left[\backslash \omega_r^2 \backslash\right] \tag{2.12}$$

where m, c, and k are the mass, damping, and stiffness matrices and $\tilde{\Phi}$, Φ, and M_r are the self-normalized mode shapes, mass-normalized mode shapes, and modal mass, respectively.

The first step is to renormalize the mode shapes in terms of the mass and to establish the mass matrix. Comparing Equations (2.9) and (2.10) provides

$$[\Phi] = \left[\tilde{\Phi}\right] [\backslash M_r \backslash]^{-1/2} \tag{2.13}$$

$$[m] = [\Phi]^{-T} [\Phi]^{-1} \tag{2.14}$$

The modal mass is known from Table 2.3 as

$$[\backslash M_r \backslash] = \begin{bmatrix} 0.523 & 0 & 0 \\ 0 & 0.548 & 0 \\ 0 & 0 & 0.523 \end{bmatrix} kg \tag{2.15}$$

and the self-normalized mode shapes are known as the real mean values of Table 2.5

$$[\tilde{\Phi}] = \begin{bmatrix} 0.8391 & -0.5329 & 0.0076 \\ 0.5305 & 0.8460 & -0.0120 \\ -0.1207 & 0.0169 & 0.9999 \end{bmatrix} \tag{2.16}$$

Substituting Equations (2.15) and (2.16) into Equation (2.13), we obtain the mass-normalized mode shapes

$$\begin{aligned} [\Phi] &= \left[\tilde{\Phi}\right] [\backslash M_r \backslash]^{-1/2} \\ &= \begin{bmatrix} 1.1603 & -0.7199 & 0.0105 \\ 0.7336 & 1.1428 & -0.0166 \\ -0.1669 & 0.0228 & 1.3826 \end{bmatrix} kg^{-1/2} \end{aligned} \tag{2.17}$$

Then, substituting Equation (2.17) into Equation (2.14) provides the mass matrix

$$[m] = [\Phi]^{-T}[\Phi]^{-1} \tag{2.18}$$
$$= \begin{bmatrix} 0.5421 & -0.0048 & 0.0543 \\ -0.0048 & 0.5444 & 0.0330 \\ 0.0543 & 0.0330 & 0.5230 \end{bmatrix} kg$$

Next, we take the linear damped natural frequencies and the linear damping factors as the intercept values in Table 2.4. We use Equation (2.8) to convert the damped natural frequencies and damping factors to the natural frequencies ω_r and damping ratios ζ_r, paying a special attention that the unit of ω_r is rad/s and not Hz. Then, we obtain the damping and stiffness matrices by an algebraic manipulation of Equations (2.11) and (2.12) as

$$[c] = [\Phi]^{-T}[\backslash 2\zeta_r\omega_r \backslash][\Phi]^{-1} \tag{2.19}$$
$$= \begin{bmatrix} 0.3171 & -0.0062 & 0.0606 \\ -0.0062 & 0.3205 & 0.0324 \\ 0.0606 & 0.0324 & 0.5638 \end{bmatrix} kg/s$$
$$[k] = [\Phi]^{-T}\left[\backslash \omega_r^2 \backslash\right][\Phi]^{-1} \tag{2.20}$$
$$= \begin{bmatrix} 9533 & -9191 & 3387 \\ -9191 & 18192 & 1899 \\ 3387 & 1899 & 31893 \end{bmatrix} kg/s^2$$

Equations (2.18)-(2.20) represent the linear parameter estimates for the frequency band involving the first three modes of the two-mass structure.

In Section 2.2, we observe a behavior that is consistent with nonlinear damping and softening stiffness nonlinearity for each of the first three structural modes from the free-decay data. In Section 2.3, we observe a behavior that is also consistent with nonlinear damping and softening stiffness nonlinearity for each of the first three structural modes from swept-sine base excitation data.

In the following chapter, we examine the issue of determining the number of modes involved in a response. In Chapter 4, we examine a signal processing technique for uncovering

the harmonic character of the nonlinear response of the structure to a primary resonance. In Chapters 5 and 6, we uncover the nonlinear damping and stiffness parameters by exploiting behaviors that emphasize the nonlinearity.

Chapter 3

Principal Component Analysis

In this chapter, we focus on the problem of determining the number of spatial basis functions of a response, and also examine the problem of determining the model order of a signal. In short, our aim is to determine the number of significant harmonics and the number of spatial basis functions involved in the response of a linear or nonlinear structural dynamic system. To accomplish this task, we utilize the method of principal component analysis (PCA).

As far as I am aware, the first application of PCA was in psychological studies [30], where control variables can be statistically redundant or lack statistical independence. PCA has also been utilized extensively throughout the engineering literature. In chemistry and heat transfer, [24] considered thermal convection, [22, 46] considered temperature fronts in the oxidation process of hydrogen on a nickel disk, and [44] considered the instability in chemically reacting systems. In fluid dynamics, [38, 81, 84] considered wind-loaded structures, [23] considered the control of vortex shedding around a cylinder, [45] considered the Burger's equation, [3] considered the Kuramoto-Sivashinsky equation, [75] considered the computational savings for 2-D turbulence simulations, [7, 12] considered turbulent mixing layers, [74] considered turbulent boundary layers, [69] considered turbulent channel flows, [6] considered turbulent shear flows, [10] considered unsteady flow past a delta wing, and [2] considered the fluctuation of the sound pressure level surrounding a jet engine. In structural dynamics,

[36] considered spring-mass-friction damper systems, [73] considered the Duffing-Holmes oscillator, [11] considered an impact oscillator, [5] considered the Lorenz equations, and [43] considered torsional springs. In modal analysis, each of [29, 33, 48, 49, 50] used some form of PCA as an internal step in the estimation of the modal parameters.

If we examine the free decay of a linear system, the model order of the response signal is mathematically related to the number of modes involved in the response, excluding the special cases of repeated poles and unobserved dynamics and ignoring the sample rate, decimation, and numerical conditioning issues. If we examine the response of a linear system to a sinusoidal excitation, then the model order of a single response signal is 2. If all of the modes are purely either in-phase or out-of-phase, the structure will have a single spatial basis function, which is a linear combination of the modes. If any of the modes has a relative phase delay, other than 0 degrees or 180 degrees, the structure will have two spatial basis functions, each of which is a linear combination of the modes, which is the general linear case. For nonlinear systems, these issues are further complicated by harmonic distortion and modal interactions.

The spatial basis functions are not normal modes, in general. However, if we know the modes present within a frequency band and if we have *enough* spatial information, then we can decompose the spatial basis functions in terms of the normal modes, which are spatial basis functions themselves.

In Section 3.1, we discuss implementation of the method of principal component analysis. In Section 3.2, we estimate the model order of the free decay of a linear oscillator via numerical simulation. Then, we examine the free response of the van der Pol oscillator and observe that the number of system degrees of freedom has, at best, a nontrivial relation to the model order of the signal. In Section 3.3, we examine the forced response of the two-mass system in five resonant conditions, namely primary resonance of each of the first two modes, subharmonic resonance of order one-half for each of the first two modes, and combination resonance of the additive type of the first two modes. In Section 3.4, a summary of the results is provided.

3.1 The Method of Principal Component Analysis

The goal of principal component analysis is to explain as much of the variance in a data set with the minimum number of parameters [39, 78]. The problem reduces to finding the so-called *weighted* principal components, which involve a rotation from the observation variables of a data set. Our phrasing of *weighted* principal components versus principal components is explained shortly. This rotation from the observation variables can be expressed as

$$\tilde{p}_k(t_\ell) = \sum_{i=1}^{n} v_i(t_\ell) q_{ik} \quad \forall \quad k \quad \in \quad \{1, 2, \ldots, m\} \quad \text{and} \quad \ell \quad \in \quad \{1, 2, \ldots, N\} \tag{3.1}$$

where $\tilde{p}_k$, v_i, t_ℓ, q_{ik}, k, i, ℓ, m, n, and N are the kth weighted principal component, the ith observation variable, the ℓth control variable, the rotation coefficients, the principal component index, the observation variable index, the control variable index, the number of principal components, the number of observation variables, and the number of control variables, respectively. For example, the $v_i(t_\ell)$ can be regarded as n measures of the structural acceleration at time t_ℓ.

The rotation coefficients q_{i1} for the first weighted principal component are chosen such that the variance of $\tilde{p}_1$ is as large as possible subject to the constraint

$$\sum_{i=1}^{n} q_{i1}^2 = 1 \tag{3.2}$$

These rotation coefficients can be determined by taking an initial guess for the q_{i1} respecting the constraint of Equation (3.2). Then, linear programming and optimization algorithms (such as the steepest descent algorithm, the conjugate direction method, or Newton's method [85]) can be utilized to determine the q_{i1} such that $-\sum_\ell p_1^2(t_\ell)$ is a minimum. In general, this is not a computationally efficient route and is subject to the potential problems of local and multiple minima. To avoid confusion in the following development, we advance the result that the q_{ik} are actually equivalent to the right singular vectors of the singular value decomposition of the matrix $V(i, \ell) = v_i(t_\ell)$, which also avoids the dilemmas of local and multiple minima that are encountered in objective minimization. The principal components

are orthogonal, but neither in the sense of the QR factorization nor in the sense of the Gram-Schmidt orthonormalization procedure [21, 79].

Now, the rotation coefficients q_{i2} for the second weighted principal component are chosen such that the variance of $\tilde{p}_2$ is as large as possible with the constraints

$$\sum_{i=1}^{n} q_{i2}^2 = 1 \tag{3.3}$$

and

$$\sum_{\ell=1}^{n} \tilde{p}_1(t_\ell)\tilde{p}_2(t_\ell) = 0 \tag{3.4}$$

The meaning of the latter constraint is that the second weighted principal component must be completely uncorrelated with the first weighted principal component. In other words, $\tilde{p}_2$ is chosen to account for the maximum amount of the total variance that is not accounted for by $\tilde{p}_1$. This general procedure is repeated m times.

Then, we let

$$d_k^2 = \sum_{\ell} \tilde{p}_k^2(t_\ell) \tag{3.5}$$

and

$$p_k(t_\ell)d_k = \tilde{p}_k(t_\ell) \tag{3.6}$$

where $p_k(t_\ell)$ and d_k^2 are the kth principal component (no weight) and *a measurement of* the variance of the kth weighted principal component, respectively. We note that the sample variance of $p_k(t_\ell)$ is $1/(N-1)d_k^2$, and not d_k^2 [39]. It follows from Equations (3.5) and (3.6) that

$$\sum_{\ell} p_k^2(t_\ell) = 1 \text{ for all } k \in \{1, 2, \ldots, m\} \tag{3.7}$$

If m is equal to $\min(n, N)$ and if the $v_i(t_\ell)$ are real, then

$$V = [P][\backslash D\backslash][Q]^T \tag{3.8}$$

where $[\backslash \ \backslash]$ implies a diagonal matrix and

$$V(\ell, i) = v_i(t_\ell) \tag{3.9}$$

$$P(\ell, k) = p_k(t_\ell) \tag{3.10}$$

$$D(k, k) = d_k \tag{3.11}$$

$$Q(k, i) = q_{ik} \tag{3.12}$$

Equation (3.8) is clearly the *economy size* singular value decomposition of the matrix V [21, 40].

The values for n and N are the row length and column length of the matrix V. However, the choice of m is not as straightforward. In statistics, one often chooses m such that the $m+1$ principal component is not *statistically significant* [39]. In engineering, one often selects m such that d_{m+1} is negligible; that is, $d_{m+1} \ll d_1$. If we choose m based on significance or negligibility, we have

$$V = [P|P_0] \begin{bmatrix} [\backslash D \backslash] & \emptyset \\ \emptyset & [\backslash D_0 \backslash] \end{bmatrix} \begin{bmatrix} Q^T \\ \hline Q_0^T \end{bmatrix} \tag{3.13}$$

when $m \leq \min(n, N)$. The variance accounted for by the first m principal components is $\sum_{k=1}^{m} d_k^2$. If the unaccounted variance $\sum_{k=m+1}^{min(n,N)} d_k^2$ is small, then

$$V \approx [P][\backslash D \backslash][Q]^T \tag{3.14}$$

where P, D, and Q are also known as the $N \times m$ left singular vectors, the m singular values, and the $n \times m$ right singular vectors, respectively.

3.1.1 Numerical Simulation

To demonstrate some of the issues involved with applying PCA to the problem of determining model order, we explore two numerical examples using delay coordinates. First, we simulate the impulse-response function of a linear single-mode system. Then, we simulate the free response of the van der Pol oscillator.

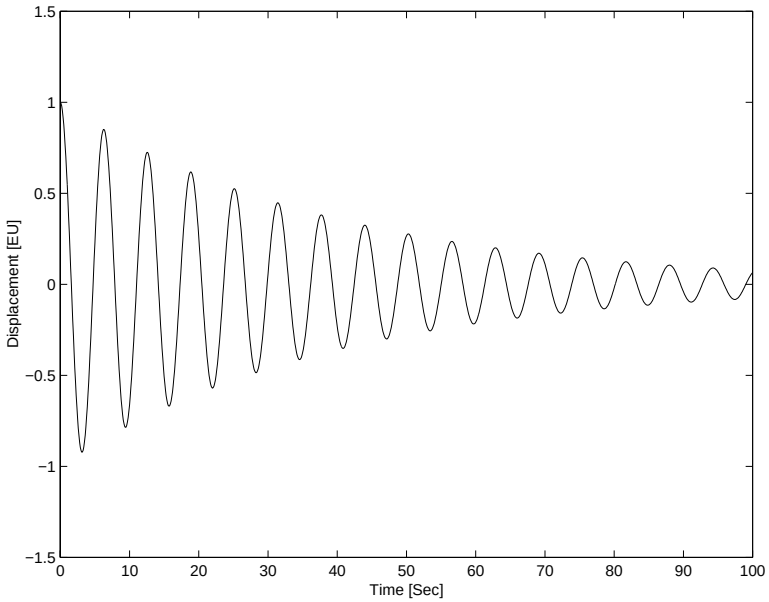

Figure 3.1: Time history of a linear impulse-response function

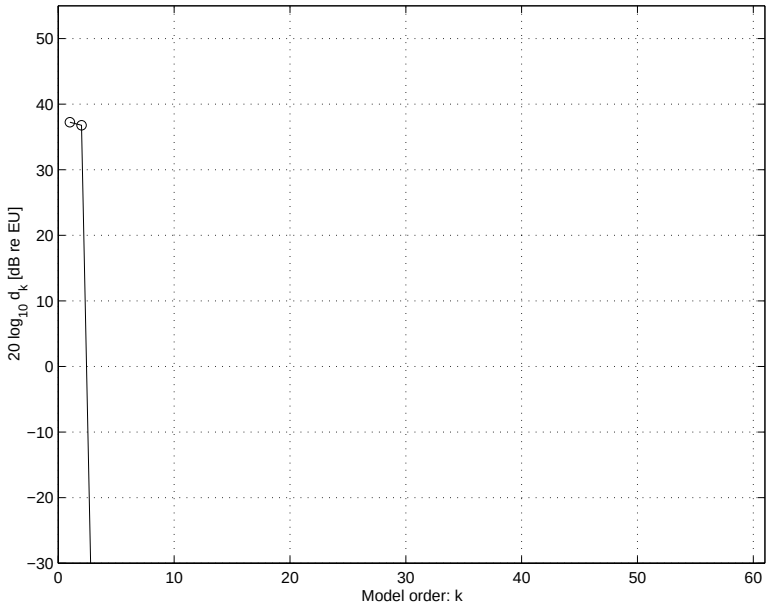

Figure 3.2: Singular values associated with a linear impulse-response function

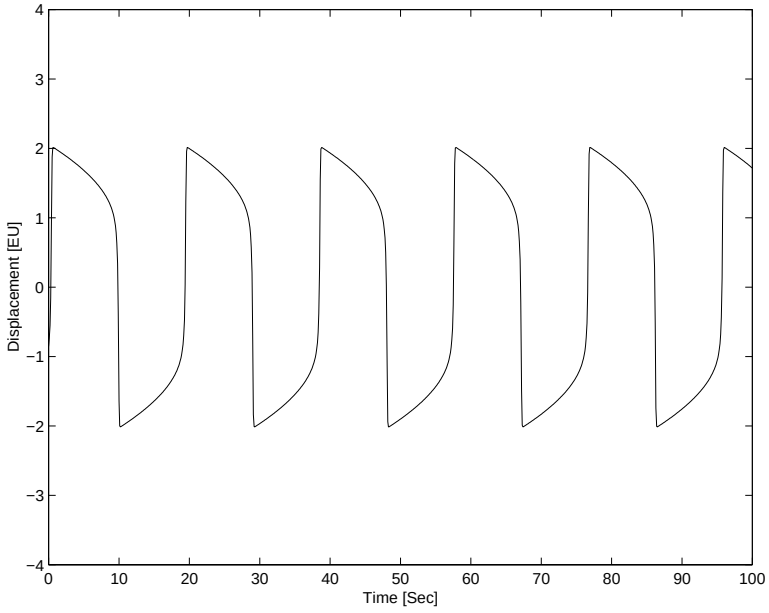

Figure 3.3: Time history of the free response of the van der Pol oscillator

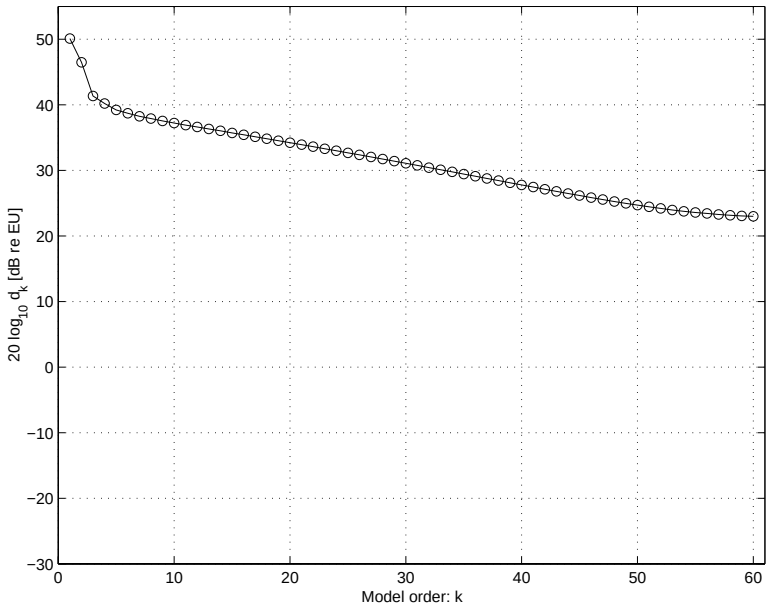

Figure 3.4: Singular values associated with the free response of the van der Pol oscillator

Linear Impulse-Response Function

We simulate the response of the system

$$\ddot{v} + c\dot{v} + v = \delta_0 \tag{3.15}$$

where $c = 0.05$ and δ_0 is a unit pulse applied at time $t = 0$. We sample the response for 100 seconds at a rate of 10 samples per second. The results of this simulation are shown in Figure 3.1. Then, we form sixty delay coordinates and assemble them in a 60×940 Hankel matrix, from which the principal components are calculated. The associated singular values are shown in Figure 3.2.

The van der Pol Oscillator

We simulate the free response for the van der Pol oscillator

$$\ddot{v} + v = \epsilon(1 - v^2)\dot{v} \tag{3.16}$$

given the initial conditions $u = 0$ and $\dot{u} = 1$ at time $t = -10$ (not shown), where $\epsilon = 10$. We sample the response for 100 seconds at a rate of 10 samples per second, starting at time $t = 0$. The results of this simulation are shown in Figure 3.3. As before, we form sixty delay coordinates and assemble them in a 60×940 Hankel matrix, from which the principal components are calculated. The associated singular values are shown in Figure 3.4.

Comments on the Results of PCA

In Figure 3.1, we show the impulse-response function of a second-order linear system. In Figure 3.2, we observe that the Hankel matrix of the signal has only two significant singular values; that is, $\{d_3, d_4, \dots\}$ are very small in comparison to d_1. For *observable* linear systems, without repeated modes, the model order of the system in first-order form is the same as the model order of the impulse-response function.

In Figure 3.3, we show the free response of the van der Pol oscillator, which is a second-order nonlinear system. In Figure 3.4, we observe that there are many significant singular values of the Hankel matrix of the corresponding signal. Consequently, it is difficult to even establish an appropriate model order for the signal, since there is no clear *cut-off*. Moreover, the model order of the system is clearly not the same as the model order of the signal.

In order to estimate the number of spatial basis functions p involved in the response of a system, one needs to look over at least $p+1$ spatial locations, in general. Since we have only one system response coordinate, we are not able to clearly establish the number of spatial basis functions involved in the response of the van der Pol oscillator. In the following section, we suggest a procedure for uncovering the number of spatial basis functions involved in five different resonant cases for the two-mass structure. Perhaps, the relation between the signal and the number of degrees of freedom, or spatial basis functions, could be estimated via an examination of the embedding dimension [62]. However, such an examination is beyond the scope of the work presented here.

3.2 Examination of the Two-Mass Structure

In this section, we estimate the spatial and temporal model order of the response of the two-mass structure undergoing five different resonant conditions, individually. The majority of the spectral content of the response is less than 50 Hz. Some minor frequency distortion is observed and is apparently limited to less than 100 Hz. The nominal resonant frequency of the fourth mode is 221 Hz. Therefore, we expect the response of the structure to be dominated by the first three structural modes with the nominal resonant frequencies 12.5, 33, and 39 Hz.

We expect the spatial model order to be at most three. In other words, we expect that either one, two, or three modes will participate in the response. These three modes or linear combinations of them will provide the spatial basis functions. In Section 3.1, we were unable to uncover the spatial model order of the van der Pol oscillator because we did not

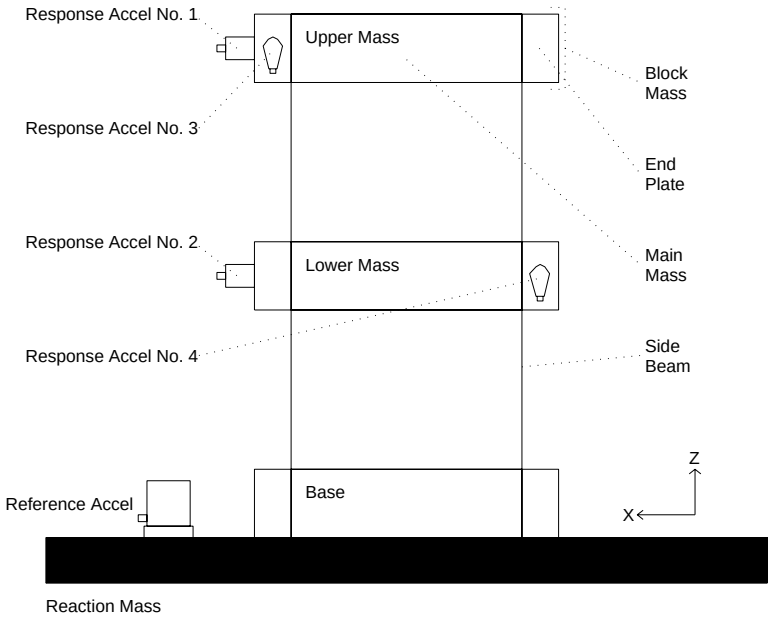

Figure 3.5: Diagram of the two-mass structure

have enough spatial informations. If we expect as many as three modes to participate in a response, we need four spatial observers to validate that there are indeed either one, two, or three and not four or more spatial basis functions.

In addition to the response location considered in Chapter 2, an additional PCB 352B33 accelerometer has been temporarily installed. The locations and orientations of the four response accelerometers are documented in Table 3.1 and illustrated in Figure 3.5. However, we also need to observe the system input, but the maximum number of readily available simultaneous channels is four. In order to observe five quantities with four channels, we choose to break our measurements into two so-called formats, documented in Table 3.1. The X,Y, and Z provide the position and the U,V, and W provide the orientation in Cartesian coordinates. Data is acquired using Format A, and subsequently using Format B. We need to acquire all four response channels simultaneously in order to establish the number of spatial basis functions. Fortunately, we do not need to compare the system input to all four response measurements simultaneously.

Table 3.1: Accelerometer locations

Format	Response Name	X	Y	Z	U	V	W
A	uprx+	52.7 mm	0 mm	215 mm	1	0	0
	lorx+	52.7 mm	0 mm	115 mm	1	0	0
	upry+	46.3 mm	10 mm	215 mm	0	1	0
	loly+	-46.3 mm	10 mm	115 mm	0	1	0
B	uprx+	52.7 mm	0 mm	215 mm	1	0	0
	lorx+	52.7 mm	0 mm	115 mm	1	0	0
	upry+	46.3 mm	10 mm	215 mm	0	1	0
	Base	46.3 mm	50 mm	0 mm	0	0	1

Table 3.2: Modal orientation with respect to the response accelerometers

Response Name	Mode 1	Mode 2	Mode 3	Mode 4	Mode 5
uprx+	+	−	0	0	0
lorx+	+	+	0	0	0
upry+	−	0	+	+	+
loly+	−	0	+	−	−

If more than three modes participate in the response, the most likely culprit would be either mode four or mode five. Table 3.2 provides the orientation of the modes with respect to the response accelerometers. Modes one and two have very little influence on the response of the "loly+" accelerometer. The orientation of mode three is in-phase to the response of the forth accelerometer, whereas modes four and five are out-of-phase. Our choice of the orientation and location of the fourth accelerometer is merely intended to delineate the potential of an unanticipated response involving either mode four or mode five from that of modes one, two, and three.

In the following sections, we examine the response of the two-mass structure to the events documented in Table 3.3. In Section 3.2.1, we examine two primary resonances via Events A and B. In Section 3.2.2, we examine two subharmonic resonances of order one-half via

Table 3.3: Events for the two-mass structure via base excitation

Event Letter	Event Description	*Actual* Excitation Frequency [Hz]	*Nominal* Response Frequency (-ies) [Hz]
A	Primary Resonance of Mode One	12.5	12.5
B	Primary Resonance of Mode Two	33	33
C	Principal Parametric Resonance of Mode One	25	12.5
D	Principal Parametric Resonance of Mode Two	66	33
E	Combination Resonance of Modes One and Two	45.5	12.5, 33, and 45.5

Events C and D. In Section 3.2.3, we examine a combination resonance of the additive type via Event E.

3.2.1 Primary Resonance

In this section, we examine the response of the two-mass system to an excitation near the resonant frequency of the first mode, and then near the resonant frequency of the second mode. The excitation is sinusoidal and in the form of a vertical base excitation.

Exciting the structure at 12.425 Hz results in a moderate amplitude response. In Figure 3.6, we observe that the number of spatial and temporal basis functions is apparently one and two based on principal component analysis, respectively. We make this conclusion by examining the relative magnitudes of the singular values. If $d_{m+1} \ll d_1$, the model order is at most m. For the spatial case, we use the decomposition

$$y(:,p)^T y(:,p) = [P][\backslash D^2 \backslash][P]^T \tag{3.17}$$

where y and p denote the acceleration response and the response index, respectively. For the temporal case, we use the decomposition

$$H_{rs}(:,:)^T H_{rs}(:,:) = [P][\backslash D^2 \backslash][P]^T \tag{3.18}$$

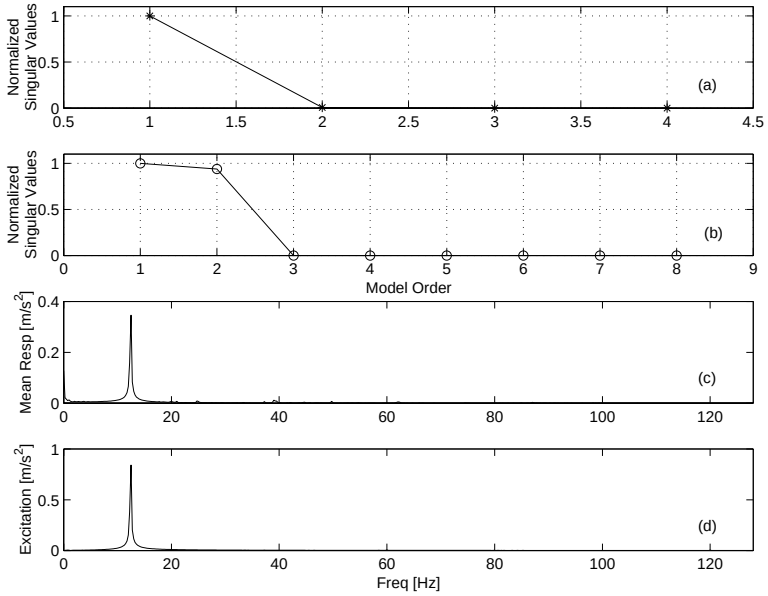

Figure 3.6: Primary resonance excitation of mode one: (a) spatial singular values, (b) temporal singular values, (c) mean response linear spectrum, and (d) reference linear spectrum

where H_{rs} is the block Hankel matrix. For a mathematical description of the block Hankel matrix, see Equations (A.3), (A.5), and (A.6) in Appendix A. The number of temporal basis functions suggests that the response contains a single harmonic. The number of spatial basis functions suggest that either only one mode is participating or all of the participating modes are purely either in-phase or out-of-phase. In Figure 3.7, we show the relative contributions of the first three modes calculated according to

$$v(:,r) = y(:,p)\Phi(p,r)^{-T} \tag{3.19}$$

where v, r, and Φ are the modal responses, the mode index, and the mass-normalized mode shapes from Chapter 2, respectively. Clearly, the vast majority of the response is due to mode one. Hence, we find that exciting the two-mass structure near 12.425 Hz results in a primary resonance of the first mode.

Similarly, exciting the structure at 33.325 Hz results in a moderate amplitude response. In Figure 3.8, we observe that the number of spatial and temporal basis functions is apparently one and two based on PCA, respectively. The number of temporal basis functions suggests

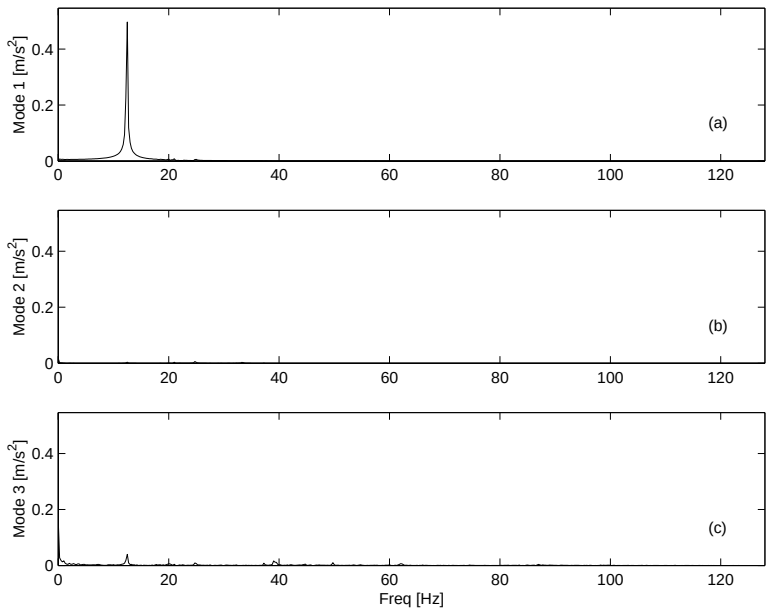

Figure 3.7: Primary resonance excitation of mode one: (a) mode one response, (b) mode two response, and (c) mode three response

that the response contains a single harmonic. The number of spatial basis functions suggests that either only one mode is participating or all of the participating modes are purely either in-phase or out-of-phase. In Figure 3.9, we show the relative contributions of the first three modes. Clearly, the vast majority of the response is due to mode two. Hence, we find that exciting the two-mass structure at 33.325 Hz results in primary resonance of the second mode.

3.2.2 Subharmonic Resonance of Order One-Half

Exciting the structure at 24.5 Hz results in a large amplitude response near 12.25 Hz. This response can not be explained in linear terms. The structure is exhibiting a nonlinear resonance. In Figure 3.10, we observe that the number of spatial and temporal basis functions is apparently one and two based on PCA, respectively. The number of temporal basis functions suggests that the response is dominated by a single tone. The number of spatial basis functions suggests that either only one mode is participating or all of the participating

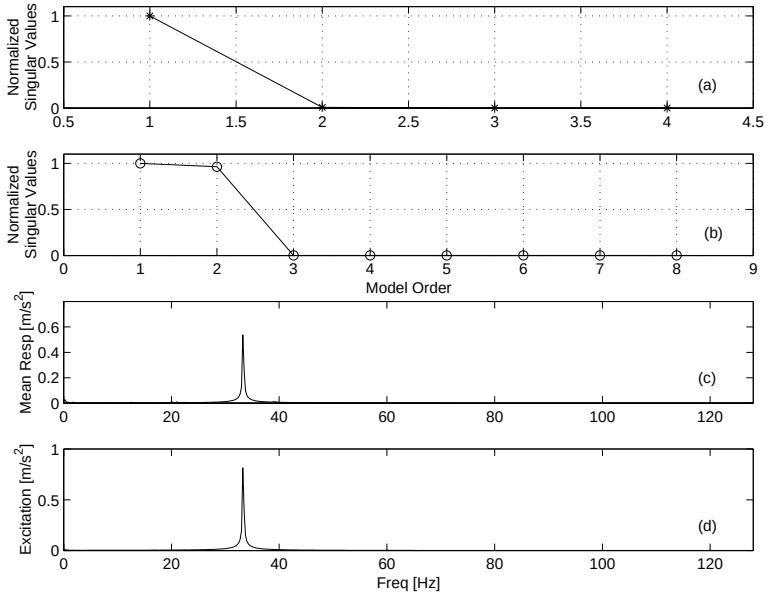

Figure 3.8: Primary resonance excitation of mode two: (a) spatial singular values, (b) temporal singular values, (c) mean response linear spectrum, and (d) reference linear spectrum

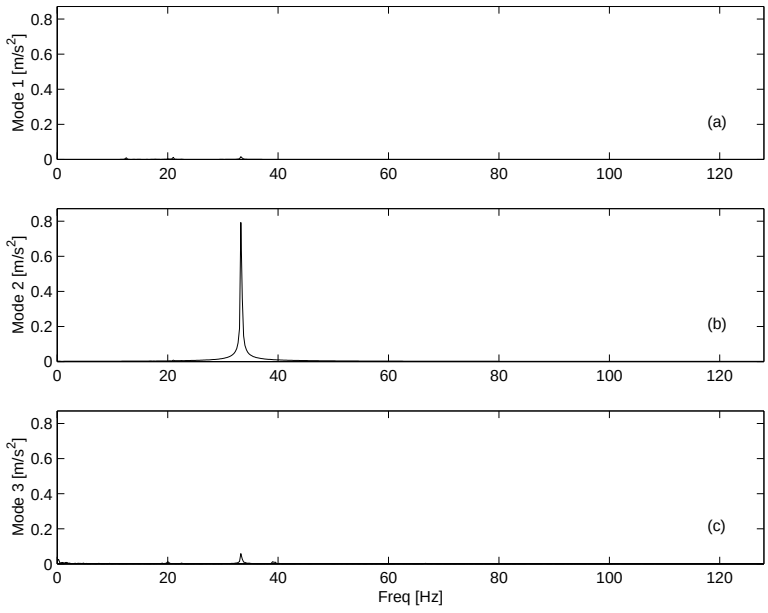

Figure 3.9: Primary resonance excitation of mode two: (a) mode one response, (b) mode two response, and (c) mode three response

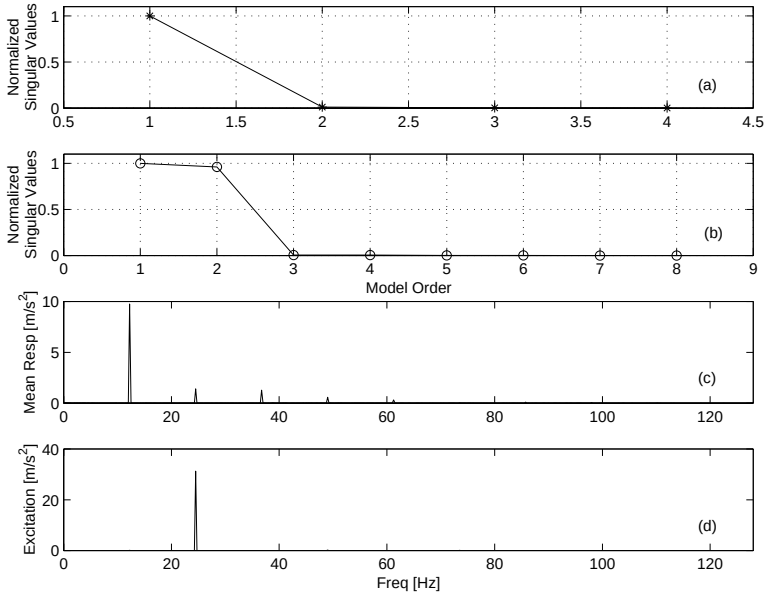

Figure 3.10: Subharmonic resonance excitation of order one-half of mode one: (a) spatial singular values, (b) temporal singular values, (c) mean response linear spectrum, and (d) reference linear spectrum

modes are purely either in-phase or out-of-phase. In Figure 3.11, we display the relative contributions of the first three modes. Clearly, the vast majority of the response is due to mode one. Hence, we conclude that the structure is undergoing a subharmonic resonance of order one-half since the response frequency is half that of the excitation frequency.

There is a very small response component at 24.5 Hz, which implies that a small direct component gives rise to the subharmonic resonance of order one-half. However, we suspect from experience that there is also a multiplicative component of the excitation, which produces a parametric contribution, also known as a principal parametric resonance of the first mode. By multiplicative, we mean that the form of excitation involves an effective net torque on the system proportional to the product of the system coordinates and the excitation. In Chapter 5, we detail these issues. Furthermore, [25, 59, 65] delineate parametric and direct excitations and principal parametric resonance and subharmonic resonance of order one-half.

Similarly, exciting the structure at 66.5 Hz, results in a large amplitude response near

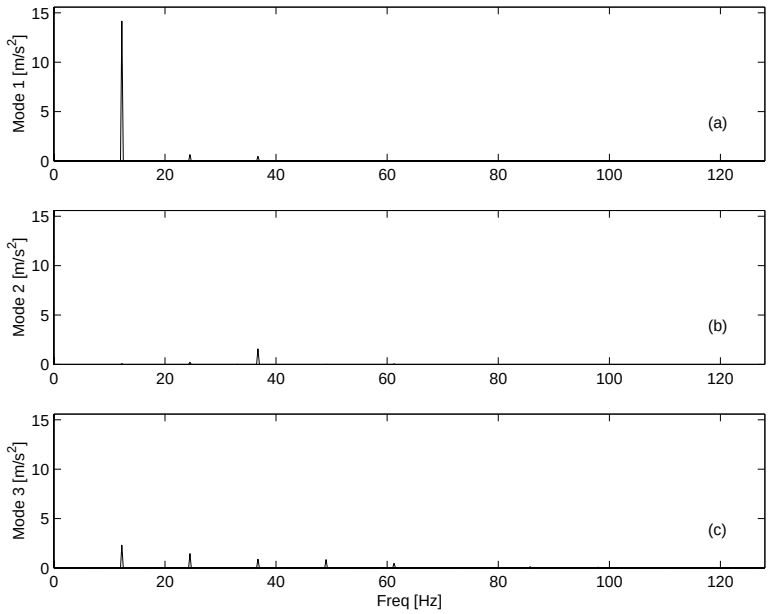

Figure 3.11: Subharmonic resonance excitation of order one-half of mode one: (a) mode one response, (b) mode two response, and (c) mode three response

33.25 Hz. This response can not be explained in linear terms. The structure is exhibiting a nonlinear resonance. In Figure 3.12, we show that the number of spatial and temporal basis functions is apparently one and two based on principal component analysis, respectively. The number of temporal basis functions suggests that the response is dominated by a single tone. The number of spatial basis functions suggests that either only one mode is participating or all of the participating modes are purely either in-phase or out-of-phase. In Figure 3.13, we observe the relative contributions of the first three modes. Clearly, the vast majority of the response is due to mode two. There is a very small response component at 66.5 Hz. We find that exciting the two-mass structure at 66.5 Hz results in a subharmonic resonance of order one-half of the second mode.

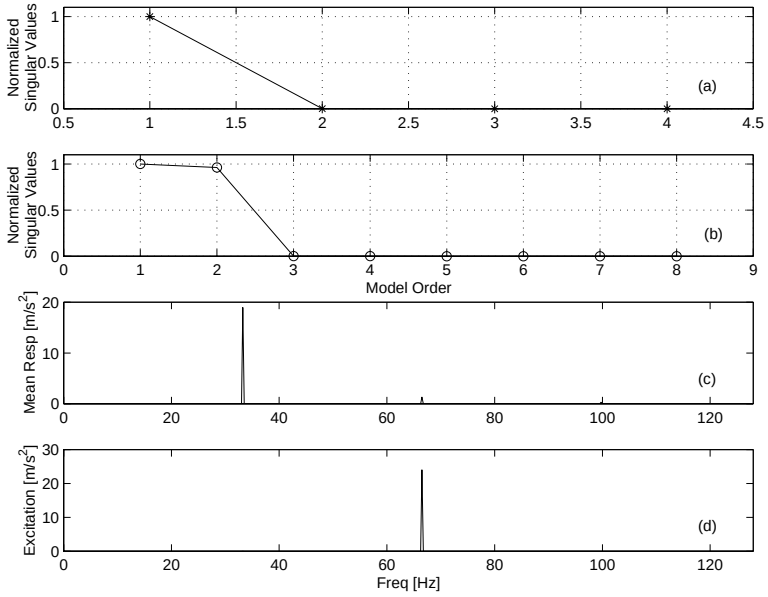

Figure 3.12: Subharmonic resonance excitation of order one-half of mode two: (a) spatial singular values, (b) temporal singular values, (c) mean response linear spectrum, and (d) reference linear spectrum

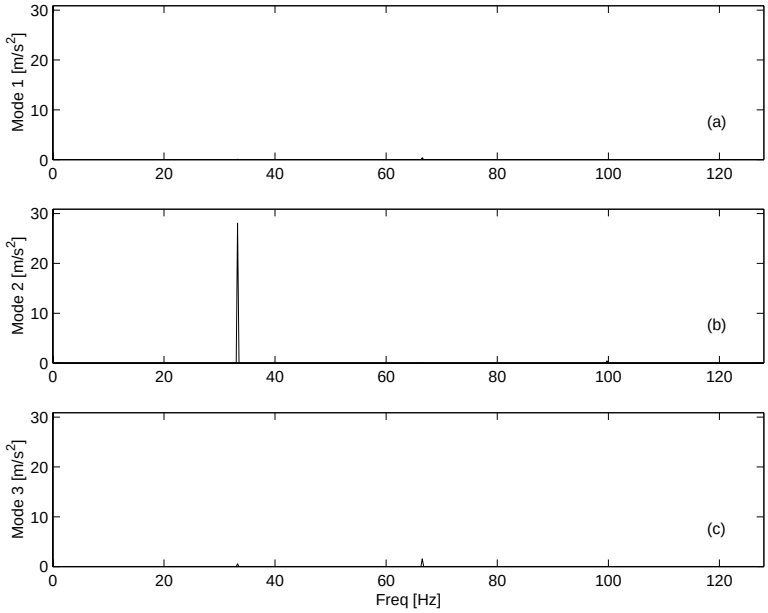

Figure 3.13: Subharmonic resonance excitation of order one-half involving mode two: (a) mode one response, (b) mode two response, and (c) mode three response

3.2.3 Combination Resonance of the Additive Type

Exciting the structure at 45.6 Hz results in a significant system response near 12.5, 33, and 45.6 Hz. This response can not be explained in linear terms. The structure is exhibiting a nonlinear resonance. It follows from Figure 3.14 that the number of spatial and temporal basis functions is apparently three and six based on PCA, respectively. The number of temporal basis functions suggests that the response is dominated by three tones. The number of spatial basis functions suggests that there are three modes that significantly participate in the response. It follows from Figure 3.15 that the tone near 12.5 Hz is dominated by the first mode, and the tone near 33 Hz is dominated by the second mode. We observe that modes one and two exhibit a significant response at 45.6 Hz, however the majority of the 45.6 Hz tone is due to the third mode. The response of the third mode is a nonresonant direct response; that is, the response predicted by linear theory. We also observe that there is no significant component near 39 Hz, corresponding to the third mode resonant frequency. Hence, we find that two effects coexist in the response. The first effect is the nonresonant direct excitation of the third mode. The second effect is a combination resonance of the first and second modes.

Had the third mode not been present, we would have expected six temporal basis functions to account for the first and second mode contributions near 12.5, 33, and 45.6 Hz. However, we would have expected only two spatial basis functions.

3.3 Summary

In this chapter, we detail the basic implementation of the method of principal component analysis. We find that exciting the two-mass structure near its first mode resonant frequency results in a primary resonance of the first mode. We find that exciting the two-mass structure near its second mode resonant frequency results in a primary resonance of the second mode. We find that exciting the two-mass structure near twice its first mode resonant frequency results in a subharmonic resonance of order one-half of the first mode. We find that

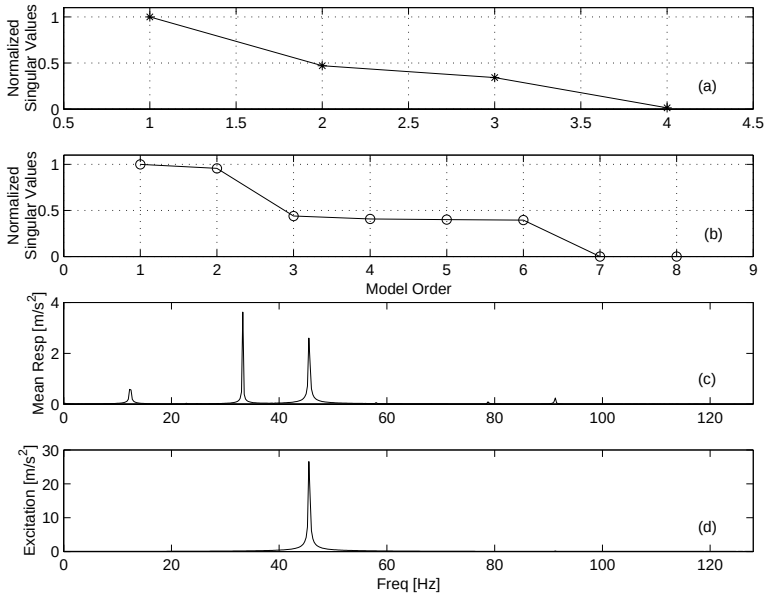

Figure 3.14: Combination resonance excitation of the additive type involving modes one and two: (a) spatial singular values, (b) temporal singular values, (c) mean response linear spectrum, and (d) reference linear spectrum

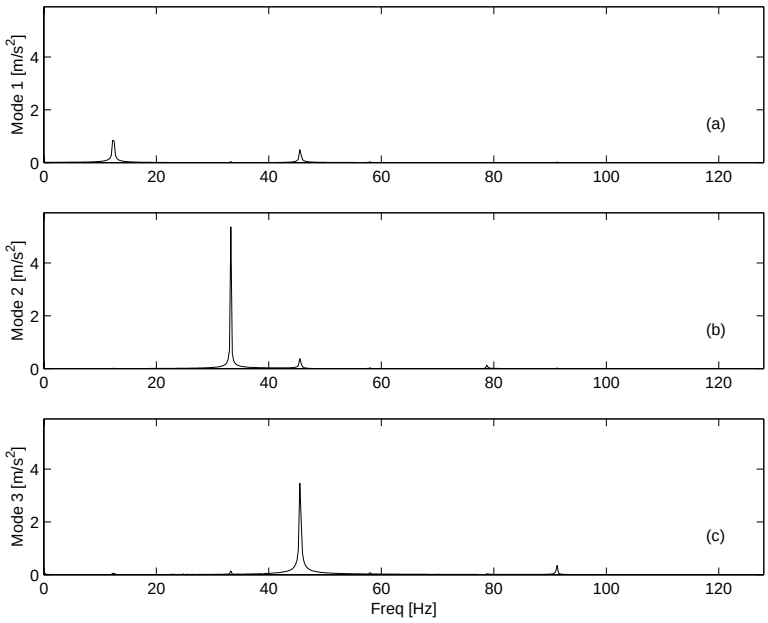

Figure 3.15: Combination resonance excitation of the additive type involving modes one and two: (a) mode one response, (b) mode two response, and (c) mode three response

exciting the two-mass structure near twice its second mode resonant frequency results in a subharmonic resonance of order one-half of the second mode. We find that exciting the two-mass structure near the sum of the first and second mode resonant frequencies results in a combination resonance of the additive type involving the first and second modes.

In the following chapter, we examine a technique to uncover the Fourier coefficients of a time-limited signal known to be composed of sine and cosine functions.

Chapter 4

The Circular-Hyperbolic Decomposition

We introduce a new closed-form decomposition technique for estimating the model parameters of an evenly sampled signal known to be composed of circular and hyperbolic sine and cosine functions in the presence of Gaussian white noise. The technique is closely related to Prony's method and hereditary algorithms that fit complex exponential functions to evenly sampled data. The circular and hyperbolic sine and cosine functions are obtained by adding constraints that limit the form of the characteristic polynomial coefficients. It avoids the leakage effects associated with the Discrete Fourier Transform (DFT) for circular sine and cosine functions. When the signal contains frequency components that are not rational multiples of each other, the proposed decomposition yields amplitude and phase parameters that are more accurate than those obtained with the DFT in moderate levels of noise. First, we review Prony's method and one hereditary algorithm (the complex exponential algorithm). Then, we detail three implementation procedures of the new technique. The first is a two-stage least-squares approach. The second utilizes a novel concept of noise reduction, which is attributed to Pisarenko [68]. The last provides additional means of noise reduction through a covariance formulation that avoids zero-lag terms. Experimental and numerical examples of the application of the circular-hyperbolic decomposition (CHD) are given.

4.1 Introduction

In many applications, there is a need to fit a discrete time-limited signal to one or more complex exponentials, such as the Markov parameters, the impulse-response function, and the ring down of a linear structural dynamic system. The Prony family of algorithms has been shown to be very useful in achieving such an objective [76]. A real signal composed of complex exponentials can be expressed as

$$v(t_\ell) = \sum_{i=1}^{m} A_i \exp(\lambda_i t_\ell) \tag{4.1}$$

and in the presence of Gaussian white noise as

$$y(t_\ell) = v(t_\ell) + \epsilon(t_\ell) \tag{4.2}$$

where m, λ_i, A_i, $v(t_\ell)$, $y(t_\ell)$, $\epsilon(t_\ell)$, and t_ℓ are the number of complex exponentials, poles (frequencies and decay rates), residues (amplitudes and phases), signal, signal with noise, noise, and evenly sampled control variable (often taken as time or distance along a path) with the associated index ℓ, respectively.

Since $v(t_\ell)$ is real, the complex pole λ_i must have a complex conjugate pole $\lambda_k = \lambda_i^*$ and its corresponding complex conjugate residue $A_k = A_i^*$. On the other hand, the poles of hyperbolic functions are real and occur in reciprocal pairs (e.g., $\lambda_2 = 1/\lambda_1$). In practice, we often make the restriction that m is an even number. Yet, there can be unpaired real poles in which case m could be odd. Here, we restrict m to be an even number $2n$ for notational purpose. We note that, although not all data can be expressed in terms of either Equation (4.1) or Equation (4.2), these equations encompass a very large class of signals [68, 76, 17, 71, 52, 37]. Details of Prony's method and the complex exponential algorithm for uncovering the parameters in Equation (4.1) are reviewed in Sections 4.2.1 and 4.2.2.

Besides the need to fit data with complex exponentials, there is a need to fit data with circular and hyperbolic sine and cosine functions, which are referred to as *circular-hyperbolic* functions. Signals that can be described in terms of these functions include stationary motions of rotating machines; deformation of cables, beams, and shells; and trajectories

of celestial bodies. Prony's hereditary algorithms can be applied to these signals because circular-hyperbolic functions represent a special case of complex exponentials. However, unless the signal is noiseless, one must contend with non-zero decay rates for circular sine and cosine functions and unpaired exponentials for hyperbolic sine and cosine functions, which can cause a dilemma in the interpretation of parameter estimates. Thus, we consider the special case of circular-hyperbolic functions. The circular-hyperbolic functions include the circular and hyperbolic sine and cosine functions and the products of circular and hyperbolic sine and cosine functions expressed as

$$\begin{aligned} v(t_\ell) =& \sum_{i=1}^{n_\omega} p_i \cos(\omega_i t_\ell) + q_i \sin(\omega_i t_\ell) \\ &+ \sum_{i=1}^{n_\kappa} a_i \cosh(\kappa_i t_\ell) + b_i \sinh(\kappa_i t_\ell) + (-1)^{\ell-1} \sum_{i=1}^{n_\eta} c_i \cosh(\eta_i t_\ell) + d_i \sinh(\eta_i t_\ell) \\ &+ \sum_{i=1}^{n_\lambda} \{e_i \cos[\mathrm{Im}(\lambda_i) t_\ell] \cosh[\mathrm{Re}(\lambda_i) t_\ell] + f_i \sin[\mathrm{Im}(\lambda_i) t_\ell] \cosh[\mathrm{Re}(\lambda_i) t_\ell] \\ &+ g_i \cos[\mathrm{Im}(\lambda_i) t_\ell] \sinh[\mathrm{Re}(\lambda_i) t_\ell] + h_i \sin[\mathrm{Im}(\lambda_i) t_\ell] \sinh[\mathrm{Re}(\lambda_i) t_\ell]\} \end{aligned} \tag{4.3}$$

$$y(t_\ell) = v(t_\ell) + \epsilon(t_\ell) \tag{4.4}$$

where the n_ω, n_κ, n_η, and n_λ are the number of the frequencies ω_i, κ_i, η_i, and λ_i, respectively; and the p_i, q_i, a_i, b_i, c_i, d_i, e_i, f_i, g_i, and h_i are the amplitudes. The parameters ω_i, κ_i, η_i, p_i, q_i, a_i, b_i, c_i, d_i, e_i, f_i, g_i, and h_i are real-valued for real signals. The λ_i are complex-valued quantities. The transition from Equation (4.1) to Equation (4.3) provides $n(= n_\omega + n_\kappa + n_\eta + 2n_\lambda)$ constraints that can be integrated into the estimation procedure. On the right-hand side of Equation (4.3), the terms one and two represent circular functions, the terms three and four represent hyperbolic functions, the terms five and six represent hyperbolic functions multiplied by a circular component at the Nyquist frequency, and the terms seven through ten represent the product of hyperbolic functions and circular functions. Details of the proposed technique to uncover the parameters in Equation (4.3) are given in Sections 4.3.1-4.3.3. Experimental and numerical examples of the proposed decomposition are given in Sections 4.4.1 and 4.4.2, respectively. Conclusions are presented in Section 4.5.

4.2 Background

In Sections 4.2.1 and 4.2.2, we review Prony's method and the complex exponential algorithm. Prony's method is a traditional technique that transforms $4n$ data points, known to be composed of exactly $2n$ complex exponentials, into the pole and residue parameters of Equation (4.1). The complex exponential algorithm is a generalization of Prony's method to data that is overdetermined and noisy.

4.2.1 Prony's Method

Prony's method transforms $N = 4n$ evenly sampled discrete data points, at this juncture taken to contain no noise, into the pole and residue parameters of $2n$ distinct complex exponentials as described in Equation (4.1) [76, 71]. When a signal contains more than $2n$ complex exponentials, the data are said to be **underdetermined**, and Prony's method will often provide an exact map between the data and results. However, the results from an underdetermined data set may not match the data exactly in some instances. For example, $v(1:4) = [1, -0.9, 0.8, -0.7]^T$ does not conform with Equation (4.1) for any choice of the λ_i and A_i when $m \leq 2$. Unfortunately, there is no reliable physical interpretation or good resolution for such results. On the other hand, most signal evaluations involve quantities of data that exceed by far the number of parameters desired. For these evaluations, the data are referred to as **overdetermined**, which will be readdressed through the complex exponential algorithm in Section 4.2.2. For now, we assume that $4n$ data points are composed of exactly

$2n$ distinct complex exponentials. In the absence of noise, the following expressions hold:

$$\begin{aligned} v(\ell) &= \sum_{i=1}^{2n} A_i \exp(\lambda_i[\ell-1]\Delta t) \\ &= \sum_{i=1}^{2n} A_i [z_i]^{\ell-1} \\ &= [A_1, A_2, \ldots, A_{2n}] \begin{bmatrix} z_1 & & & 0 \\ & z_2 & & \\ & & \ddots & \\ 0 & & & z_{2n} \end{bmatrix}^{\ell-1} \begin{Bmatrix} 1 \\ 1 \\ \vdots \\ 1 \end{Bmatrix} \end{aligned} \tag{4.5}$$

where $t_\ell = [\ell - 1]\Delta t$ is time in seconds. The parameters z_i and λ_i represent the ith pole in the z-domain and frequency domain, respectively. These parameters are related by

$$\lambda_i = \frac{1}{\Delta t} \ln(z_i) \tag{4.6}$$

where λ_i has units of radians per second. The problem reduces to finding the z_i and A_i such that Equation (4.5) holds for all $\ell \in \{1, 2, \ldots, 4n\}$.

The z-domain characteristic polynomial is given by

$$\prod_{i=1}^{2n} [z - z_i] = \sum_{k=0}^{2n} \alpha_k [z]^k \tag{4.7}$$

where $\alpha_{2n} = 1$ and its roots z_i are the poles, which need to be uncovered. We note that the characteristic polynomial has the special property

$$\sum_{k=0}^{2n} \alpha_k [z]^k = 0 \tag{4.8}$$

for all $z \in \{z_1, z_2, \ldots, z_{2n}\}$.

Next, we introduce the Hankel matrix $V(i,k) \equiv v(i+k-1)$, which can be expressed in

verbose form as

$$V(1:2n, 1:2n+1) = \begin{bmatrix} v(1) & v(2) & \dots & v(2n+1) \\ v(2) & v(3) & \dots & v(2n+2) \\ \vdots & \vdots & \ddots & \vdots \\ v(2n) & v(2n+1) & \dots & v(4n) \end{bmatrix} \tag{4.9}$$

As a consequence of Equation (4.5), every row in the Hankel matrix can be written as

$$V(\ell, 1:2n+1) = [A_1, A_2, \dots, A_{2n}] \times \begin{bmatrix} z_1 & & & 0 \\ & z_2 & & \\ & & \ddots & \\ 0 & & & z_{2n} \end{bmatrix}^{\ell-1} \begin{bmatrix} 1 & z_1 & \dots & z_1^{2n} \\ 1 & z_2 & \dots & z_2^{2n} \\ \vdots & \vdots & \ddots & \vdots \\ 1 & z_{2n} & \dots & z_{2n}^{2n} \end{bmatrix} \tag{4.10}$$

However, it follows from Equation (4.8) that

$$\begin{bmatrix} 1 & z_1 & \dots & z_1^{2n} \\ 1 & z_2 & \dots & z_2^{2n} \\ \vdots & \vdots & \ddots & \vdots \\ 1 & z_{2n} & \dots & z_{2n}^{2n} \end{bmatrix} \begin{Bmatrix} \alpha_0 \\ \alpha_1 \\ \vdots \\ \alpha_{2n} \end{Bmatrix} = \begin{Bmatrix} 0 \\ 0 \\ \vdots \\ 0 \end{Bmatrix} \tag{4.11}$$

Therefore, $V(\ell, 1:2n+1)[\alpha_0, \alpha_1, \dots, \alpha_{2n}]^T = 0$, and $V(1:2n, 1:2n+1)[\alpha_0, \alpha_1, \dots, \alpha_{2n}]^T$ results in the null vector $[0, 0, \dots, 0]^T$. Hence, the entries in each row of the Hankel matrix are related by the coefficients of the characteristic polynomial. Since $\alpha_{2n} = 1$, the characteristic polynomial coefficients can be determined directly from the Hankel matrix. Partitioning the right-hand column and inverting the remainder, we obtain

$$[\alpha_0, \alpha_1, \dots, \alpha_{2n-1}]^T = -V(1:2n, 1:2n)^{-1} V(1:2n, 2n+1) \tag{4.12}$$

where $[\ ]^{-1}$ denotes the matrix inverse operator. The poles z_i can then be calculated by solving Equation (4.8).

We emphasize that the above procedure is valid when the signal contains exactly $2n$ complex exponentials. If the signal contains less than $2n$ complex exponentials, the calculation of the inverse of the matrix will be ill-conditioned. If the signal contains more than $2n$ complex exponentials, the calculation will not respect the *true* spectral information and may not match the data exactly.

Having calculated the characteristic delays z_i, we determine the residues A_i from

$$\begin{Bmatrix} A_1 \\ A_2 \\ \vdots \\ A_{2n} \end{Bmatrix} = \begin{bmatrix} 1 & 1 & \dots & 1 \\ z_1 & z_2 & \dots & z_{2n} \\ \vdots & \vdots & \ddots & \vdots \\ z_1^{2n-1} & z_2^{2n-1} & \dots & z_{2n}^{2n-1} \end{bmatrix}^{-1} \begin{Bmatrix} v(1) \\ v(2) \\ \vdots \\ v(2n) \end{Bmatrix} \tag{4.13}$$

We note that this computation requires only the first $2n$ data points. When dealing with overdetermined data sets in the following section, all of the data are utilized in establishing the residues. Here, the first $2n$ data points produce results that are equivalent to those obtained with any other combination of $2n$ data points in $v(\ell)$. In the next section, we provide two generalizations of Prony's method, namely, the treatment of overdetermined data and noise.

4.2.2 Complex Exponential Algorithm

In this section, we review the complex exponential algorithm [76], *which is known as the least-squares Prony's method, the autoregressive technique, or the maximum entropy method.* The complex exponential algorithm is an **estimation procedure** as opposed to a **transformation**. Prony's method is a transformation because $4n$ data points are represented by $4n$ parameters. The complex exponential algorithm represents $N \geq 4n$ data points with $4n$ parameters, as in Equation (4.1) or as in Equation (4.2), in the presence of noise. We assume that N evenly sampled data points are known to contain exactly $2n$ distinct complex exponentials in the presence of Gaussian white noise, as in Equation (4.2). We intend to uncover the parameters of Equation (4.1) and quantify the noise contribution.

The basic concept of the complex exponential algorithm is to utilize data redundancy not considered by Prony's method to provide an averaged or, at least, a more consistent result. A closed-form solution is established by breaking the problem into two linearized stages. The first stage uncovers the characteristic delays and the second one uncovers the associated residues. Again, we examine the structure of the Hankel matrix

$$Y(1:N-2n,1:2n+1) = \begin{bmatrix} y(1) & y(2) & \dots & y(2n+1) \\ y(2) & y(3) & \dots & y(2n+2) \\ \vdots & \vdots & \ddots & \vdots \\ y(N-2n) & y(N-2n+1) & \dots & y(N) \end{bmatrix} \tag{4.14}$$

where $y(\ell) = v(\ell) + \epsilon(\ell)$. In this case, the column length of Y is $N - 2n$ and is chosen so that the index ℓ does not exceed N. Each row of the Hankel matrix $Y(\ell, 1 : 2n + 1)$ can still be related by the coefficients of the characteristic polynomial, in Equation (4.7), with an associated error $e(\ell)$ given by

$$e(\ell) = Y(\ell, 1:2n+1) \begin{Bmatrix} \alpha_0 \\ \alpha_1 \\ \vdots \\ \alpha_{2n} \end{Bmatrix} \tag{4.15}$$

This error must be equal to $\sum_{k=0}^{2n} \alpha_k \epsilon(\ell + k)$ according to the definition of $y(\ell)$ in Equation (4.2). The first stage of the least-squares solution is obtained by summing the squares of the errors and minimizing the primary objective function

$$SSE_1(\alpha_0, \dots, \alpha_{2n-1}; \alpha_{2n}) = \sum_{\ell=1}^{N-2n+1} e(\ell)^2 \tag{4.16}$$

The solution is expressed as

$$[\alpha_0, \alpha_1, \dots, \alpha_{2n-1}]^T = -Y(1:N-2n, 1:2n)^+ Y(1:N-2n, 2n+1) \tag{4.17}$$

where $\alpha_{2n} = 1$ and the matrix pseudo-inverse operator $[\ ]^+ \equiv [[\ ]^T[\ ]]^{-1}[\ ]^T$ for real quantities and $[\ ]^+ \equiv [[\ ]^H[\ ]]^{-1}[\ ]^H$ for complex ones. The poles z_i are determined from Equation (4.8).

In the second stage, the residues A_i are determined by defining a secondary objective function as

$$SSE_2(A_1, \ldots, A_{2n}) = \sum_{\ell=1}^{N} \epsilon(\ell)^2 \tag{4.18}$$

The minimum of this function is realized when

$$\begin{Bmatrix} A_1 \\ A_2 \\ \vdots \\ A_{2n} \end{Bmatrix} = \begin{bmatrix} 1 & 1 & \ldots & 1 \\ z_1 & z_2 & \ldots & z_{2n} \\ \vdots & \vdots & \ddots & \vdots \\ z_1^{N-1} & z_2^{N-1} & \ldots & z_{2n}^{N-1} \end{bmatrix}^{+} \begin{Bmatrix} y(1) \\ y(2) \\ \vdots \\ y(N) \end{Bmatrix} \tag{4.19}$$

We note also that this computation involves all N data points in contrast to Equation (4.13). Prony's method and the complex exponential algorithm provide the same result if either the data matches Equation (4.1) or $N = 4n$.

4.3 Circular-Hyperbolic Decomposition

In this section, we detail three implementations of the new circular-hyperbolic decomposition technique (CHD). In the first implementation, we utilize a two-stage least-squares approach that parallels the complex exponential algorithm. In the second one, we modify the technique by incorporating a novel concept of noise reduction attributed to Pisarenko [68]. In the third implementation, we provide additional means of noise reduction through a covariance formulation that avoids zero-lag terms. These implementations are discussed in Sections 4.3.1, 4.3.2, and 4.3.3, respectively.

The basic concept of the CHD involves constraining the form of the characteristic polynomial coefficients α_k defined in Equation (4.7). However, constraining these coefficients is not a new concept [68, 52]. In Pisarenko's Harmonic Decomposition (PHD) [68], we find the

α_k as the eigenvector associated with the smallest eigenvalue μ_0 of

$$\begin{bmatrix} B(0) & B(1) & \dots & B(2n) \\ B(1) & B(0) & \dots & B(2n-1) \\ \vdots & \vdots & \ddots & \vdots \\ B(2n) & B(2n-1) & \dots & B(0) \end{bmatrix} \begin{Bmatrix} \alpha_0 \\ \alpha_1 \\ \vdots \\ \alpha_{2n} \end{Bmatrix} = \mu_0 \begin{Bmatrix} \alpha_0 \\ \alpha_1 \\ \vdots \\ \alpha_{2n} \end{Bmatrix}$$

Here, the $B(k)$ is a known covariance function of a real stationary signal of order $2n$. For instance, we often take the covariance function to be the autocorrelation function. Observe that the first row reads exactly the same as the last row in reverse, the second row reads exactly the same as the second to last row in reverse, and so forth. Thus, the PHD implicitly enforces the symmetry requirement

$$\alpha_{n+i} = \alpha_{n-i} \text{ for } i \in \{1, 2, \dots, n\} \tag{4.20}$$

It can be shown that a stationary signal whose autocorrelation function satisfies Equation (4.20) must be composed of circular sine and cosine functions. Pisarenko [68] and Marple [52] provide additional insights into this point.

We should stress that, and as a cautionary note, we do not detail the implementation of the PHD. We utilize some concept from the PHD in Section 4.3.2, but the implementation of Section 4.3.2 should not be confused with the PHD. A detailed description of the PHD is given in [68].

The α_k can certainly be estimated from a covariance function, as is the case with the PHD. The process of estimating a covariance function has its own associated difficulties and errors, particularly for a signal with a short duration. The phase information of a signal can not generally be recovered from a covariance function. It is also obvious that covariance functions are also ill-defined for hyperbolic functions in the stationary sense. Hence, it may not be desirable to estimate a covariance function and subsequently estimate the signal parameters. Rather, we are motivated to estimate the signal parameters directly from the signal itself.

As detailed in Section 4.2.1, the α_k also relate the columns of the Hankel matrix of a

sampled signal. But, the Hankel matrix does not enjoy the symmetries observed in the covariance matrix B above. This section details different methods of enforcing the symmetries in the α_k. We note that the method that we use to enforce this symmetry is similar to the one used in the Prony Spectral Line (PSL) estimation technique [52]. However, we do not provide details of the PSL.

Another important issue to address, here, is that an estimation algorithm can neither recognize that a signal is stationary nor generally enforce the requirements of stationarity. Upon close examination, Equation (4.20) can also be satisfied by a large class of nonstationary functions, namely, hyperbolic sine and cosine functions and the products of hyperbolic sine and cosine functions and circular sine and cosine functions. Enforcing the symmetry conditions in Equation (4.20) is broader than just a means to uncover circular sine and cosine functions. It provides means for decomposing a time-limited signal in terms of circular and hyperbolic sine and cosine functions.

4.3.1 The Least Squares Procedure

In this section, we describe how to constrain the complex exponential algorithm to decompose a signal in terms of circular-hyperbolic functions in the presence of noise, as expressed in Equation (4.4). We begin by examining the structure of the characteristic polynomial for circular and hyperbolic functions; that is, $p\cos(\omega t_\ell) + q\sin(\omega t_\ell)$, $a\cosh(\kappa t_\ell) + b\sinh(\kappa t_\ell)$, or $(-1)^{\ell-1}[c\cosh(\eta t_\ell) + d\sinh(\eta t_\ell)]$). We observe that each of these functions has two poles $\{z_1, z_2\}$ with the property

$$z_1 z_2 = 1 \tag{4.21}$$

Hence, the characteristic polynomial, for either a circular or a hyperbolic function, always takes the form

$$z^2 + (z_1 + z_2)z + 1 = z^2 + r_1 z + 1 \tag{4.22}$$

where r_1 is real. Similarly, we examine the structure of the characteristic polynomial for the terms involving the product of circular and hyperbolic functions in Equation (4.3). We

observe that each of these terms has four poles $\{z_1, z_2, z_3, z_4\} = \{z, 1/z, z^*, 1/z^*\}$ with the property

$$z_1 z_2 = z_3 z_4 = 1 \tag{4.23}$$

Therefore, the characteristic polynomial for the product of a circular function and a hyperbolic function always takes the form

$$[z^2 + (z_1 + z_2)z + 1][z^2 + (z_3 + z_4)z + 1] = \prod_{i=1}^{2}(z^2 + r_i z + 1) \tag{4.24}$$

where the r_i are real. Subsequently, the characteristic polynomial for n circular-hyperbolic functions, where the product of a circular function and a hyperbolic function counts as 2, can be expressed as

$$\begin{aligned}\prod_{i=1}^{n}[z^2 + r_i z + 1] &= z^{2n} + \sum_{i=1}^{n} r_i z^{2n-1} + \sum_{i=1}^{n}\sum_{k=1}^{n} r_i r_k z^{2n-2} + \cdots + \sum_{i=1}^{n} r_i z + 1 \\ &= z^{2n} + \alpha_{2n-1} z^{2n-1} + \alpha_{2n-2} z^{2n-2} + \cdots + \alpha_1 z + 1\end{aligned} \tag{4.25}$$

Examining the structure of Equation (4.25), we note that the polynomial coefficients exhibit the symmetries

$$\alpha_{n-i} = \alpha_{n+i} \text{ for } i \in \{1, 2, \ldots, n\} \tag{4.26}$$

which provide n constraints. This symmetry requirement is exactly the same as in Equation (4.20).

Next, we choose the matrix

$$\tilde{Y}(1 : N - 2n, 1 : n + 1) = \tag{4.27}$$
$$\left[\begin{array}{c|ccc} y(n+1) & y(n) + y(n+2) & \ldots & y(1) + y(2n+1) \\ y(n+2) & y(n+1) + y(n+3) & \ldots & y(2) + y(2n+2) \\ \vdots & \vdots & \ddots & \vdots \\ y(N-n) & y(N-n-1) + y(N-n+1) & \ldots & y(N-2n) + y(N) \end{array}\right]$$

Due to the symmetries in Equation (4.26), the objective function, expressed in Equation (4.16), has a constrained minimum when

$$[\alpha_n, \alpha_{n+1}, \ldots, \alpha_{2n-1}]^T = -\tilde{Y}(1 : N - 2n, 1 : n)^+ \tilde{Y}(1 : N - 2n, n + 1) \tag{4.28}$$

where $\alpha_{2n} = 1$. Here, we note that the minimum number of data points required is reduced; Equation (4.28) can be executed when $N \geq 3n$, whereas Equation (4.17) requires that $N \geq 4n$. The polynomial coefficients $\{\alpha_0, \alpha_1, \ldots, \alpha_{n-1}\}$ are given by Equation (4.26), and the poles are calculated by solving Equation (4.8) as before. Then, the residues can be calculated according to Equation (4.19). If the results can be presented in exponential form, the decomposition is complete.

If we were to use either the PHD or the PSL, we would not know how to contend with z-domain pole estimates away from the unit circle because they are not expected. This can be a practical concern when implementing either the PHD or the PSL. One approach to resolve this dilemma, for spectral line estimation, is to ignore the modulus of the pole estimates and to recalculate them via $\exp(j \operatorname{Arg}(z))$, where $\operatorname{Arg}(z)$ denotes the argument of z (the polar angle on the z-domain). Although, this approach may be appropriate for practical purposes, it is not correct in a rigorous sense. It ignores the basic fact that the solution set that satisfies the symmetry requirement in Equation (4.20) is broader than just the circular sine and cosine functions.

We also observe that Equation (4.3) actually extends to the entire z-domain. One might now wonder if there is really any difference between Equations (4.1) and (4.3). The difference is one of emphasis. The symmetry requirement encourages the pole estimates to occur on either the unit circle or the real line, where it takes only one degree of freedom $n = n_\omega$, n_κ, or n_η per frequency. Elsewhere, it takes two degrees of freedom $n = 2n_\lambda$ per frequency. This also suggests a potential for difficulties in large-order problems or problems where the model order is highly overspecified with so-called computational degrees of freedom. The full benefits over the complex exponential algorithm may not be realized in such instances.

When the results are desired in the form of Equation (4.3), some additional algebra is required. First, we collect the poles on the unit circle and pair complex conjugate poles and residues. The circular frequencies ω_i and amplitudes p_i and q_i associated with the pole pair

$\{z, z^*\}$ and corresponding residues $\{A, A^*\}$ are

$$\omega = |\text{Arg}(z)|/\Delta t \tag{4.29}$$

$$p = 2\ \text{Real}(A) \tag{4.30}$$

$$q = -2\ \text{Imag}(A) \tag{4.31}$$

Next, we collect the positive poles and pair reciprocal poles and corresponding residues. The first hyperbolic frequencies κ_i and amplitudes a_i and b_i associated with the pole pair $\{z, 1/z\}$ $(z > 1)$ and corresponding residues $\{A_z, A_{1/z}\}$ are

$$\kappa = \ln(z)/\Delta t \tag{4.32}$$

$$a = (A_z + A_{1/z}) \tag{4.33}$$

$$b = (A_z - A_{1/z}) \tag{4.34}$$

Then, we collect the negative poles and pair reciprocal poles and corresponding residues. The second hyperbolic frequencies η_i and amplitudes c_i and d_i associated with the pole pair $\{z, 1/z\}$ $(|z| > 1)$ and corresponding residues $\{A_z, A_{1/z}\}$ are

$$\eta = \ln(|z|)/\Delta t \tag{4.35}$$

$$c = (A_z + A_{1/z}) \tag{4.36}$$

$$d = (A_z - A_{1/z}) \tag{4.37}$$

Finally, the remaining poles must correspond to the λ_i in Equation (4.3). The frequencies λ_i and amplitude e_i, f_i, g_i, and h_i associated with the poles $\{z, 1/z, z^*, 1/z^*\}$ $(|z| > 1$ and $\text{Im}(z) > 0)$ and corresponding residues $\{A_z, A_{1/z}, A_{z^*}, A_{1/z^*}\}$ are

$$\lambda = \ln(z)/\Delta t \tag{4.38}$$

$$e = 2\ \text{Re}(A_z + A_{1/z}) \tag{4.39}$$

$$f = -2\ \text{Im}(A_z - A_{1/z}) \tag{4.40}$$

$$g = 2\ \text{Re}(A_z - A_{1/z}) \tag{4.41}$$

$$h = -2\ \text{Im}(A_z + A_{1/z}) \tag{4.42}$$

Equations (4.29) through (4.42) provide the estimates of the parameters for the deterministic part of the signal in the form of Equation (4.3). The noise part can be obtained by generating Equation (4.3) from the parameter estimates and subtracting the result from the original data. Equations (4.19), (4.26), and (4.28) represent the basic formulation of the CHD.

4.3.2 Noise Reduction via the Pisarenko Procedure

In this section, we utilize a noise reduction technique due to Pisarenko to establish an unbiased estimate of the characteristic polynomial from the covariance matrix. Pisarenko [68] showed that this is possible if the effect of noise on the covariance matrix is known. However, the method presented here is not the PHD and should not be confused as such.

The expected value of the covariance of y can be expressed as

$$E[y(i)y(k)] = \left\{ \begin{array}{c} v(i)v(i) + \mu_0 \quad \text{for} \quad i = k \\ v(i)v(k) \quad \text{for} \quad i \neq k \end{array} \right\} \tag{4.43}$$

where $E[\ ]$ denotes the expected value. The expected value of the random part is zero whenever $i \neq k$. When $i = k$, the expected value of the random part approaches the noise variance

$$\mu_0 = \lim_{N \to \infty} \frac{1}{N} \sum_{i=1}^{N} \epsilon(i)^2 \tag{4.44}$$

which is a zero-lag term. Defining $\tilde{y}_i$ as the ith column of $\tilde{Y}$, we form a special time-dependent or transient covariance matrix as

$$C(1:n+1, 1:n+1) = \begin{bmatrix} \tilde{y}_1^T \tilde{y}_1 & \tilde{y}_1^T \tilde{y}_2 & \cdots & \tilde{y}_1^T \tilde{y}_{n+1} \\ \tilde{y}_2^T \tilde{y}_1 & \tilde{y}_2^T \tilde{y}_2 & \cdots & \tilde{y}_2^T \tilde{y}_{n+1} \\ \vdots & \vdots & \ddots & \vdots \\ \tilde{y}_{n+1}^T \tilde{y}_1 & \tilde{y}_{n+1}^T \tilde{y}_2 & \cdots & \tilde{y}_{n+1}^T \tilde{y}_{n+1} \end{bmatrix} \tag{4.45}$$

which is an unconventional expression due to our definition of $\tilde{Y}$ and subsequently $\tilde{y}_i$. The

expected value of C can be expressed as

$$E[C(1:n+1,1:n+1)] = \begin{bmatrix} \tilde{v}_1^T\tilde{v}_1 + \mu & \tilde{v}_1^T\tilde{v}_2 & \dots & \tilde{v}_1^T\tilde{v}_{n+1} \\ \tilde{v}_2^T\tilde{v}_1 & \tilde{v}_2^T\tilde{v}_2 + 2\mu & \dots & \tilde{v}_2^T\tilde{v}_{n+1} \\ \vdots & \vdots & \ddots & \vdots \\ \tilde{v}_{n+1}^T\tilde{v}_1 & \tilde{v}_{n+1}^T\tilde{v}_2 & \dots & \tilde{v}_{n+1}^T\tilde{v}_{n+1} + 2\mu \end{bmatrix} \tag{4.46}$$

where $\tilde{v}_i$ is the noise free part of $\tilde{y}_i$ and μ is μ_0 times the column length of $\tilde{Y}$. The eigenvalue decomposition

$$\begin{bmatrix} 1 & 0 & \dots & 0 \\ 0 & \frac{1}{2} & \dots & 0 \\ \vdots & \vdots & \ddots & \vdots \\ 0 & 0 & \dots & \frac{1}{2} \end{bmatrix} C(1:n+1,1:n+1) = \Psi\Lambda\Psi^{-1} \tag{4.47}$$

provides the eigenvalues as the components of the diagonal matrix Λ and the eigenvectors as the columns of Ψ. It follows from the structure of Equation (4.46) that the eigenvector $\Psi(:,1)$ associated with the minimum eigenvalue $\Lambda(1)$ is an unbiased estimate of the characteristic polynomial coefficients $\{\alpha_n, \alpha_{n+1}, \dots, \alpha_{2n}\}^T$ for which μ is a minimum. Additionally, the eigenvalue decomposition may provide improved numerical stability in comparison to Equation (4.28). Furthermore, the value of $\Lambda(1)$ divided by the column length of $\tilde{Y}$ provides an estimate of the noise variance μ_0. We note that α_{2n} need not be set equal to unity. As before, the coefficients $\{\alpha_0, \alpha_1, \dots, \alpha_{n-1}\}$ are determined according to Equation (4.26). Then, the poles and residues are calculated using Equations (4.8) and (4.13), respectively.

4.3.3 Noise Reduction via the Covariance Procedure

In the preceding section, we observed that only the zero-lag terms of the expected value of the covariance matrix C are affected by Gaussian white noise. Assuming that all of our other model assumptions are satisfied, the least-squares formulation of the complex exponential algorithm biases results because the errors $e(\ell)$ in Equation (4.15) are not statistically independent. The statistical independence is an important and an often violated assumption

involved with the least-squares regression [39]. We begin with the observation that Equation (4.28) can also be expressed in terms of the covariance matrix as

$$\begin{Bmatrix} \alpha_n \\ \alpha_{n+1} \\ \vdots \\ \alpha_{2n-1} \end{Bmatrix} = -C(1:n,1:n)^{-1}C(1:n,n+1) \tag{4.48}$$

We observe from Equation (4.46) that while $E[C(i,i)]$ contains a noise contribution, $E[C(i,k)]$ does not whenever $i \neq k$.

By letting

$$\tilde{C}(1:n,1:n+1) = \tilde{Y}(1:N-2n,1:n)^T\tilde{Y}(2n+1:N,1:n+1) \tag{4.49}$$

we can obtain an unbiased estimate of the characteristic polynomial coefficients via

$$\begin{Bmatrix} \alpha_n \\ \alpha_{n+1} \\ \vdots \\ \alpha_{2n-1} \end{Bmatrix} = -\tilde{C}(1:n,1:n)^{-1}\tilde{C}(1:n,n+1) \tag{4.50}$$

because the α_k also relate the noise-free portions of the covariance matrix, as shown for the Hankel matrix in Section 4.2.1. The key feature of this approach involves avoiding the zero-lag terms of the covariance matrix. The remaining coefficients $\{\alpha_0, \alpha_1, \ldots, \alpha_{n-1}\}$ are obtained according to Equation (4.26). The poles and residues are determined according to Equations (4.8) and (4.13), respectively.

We note that, in general, the data do not conform with our other model assumption, and the assumption of statistical independence may or may not be significant in comparison with other potential violations of the model assumptions.

4.4 Applications

In this section, we provide experimental and numerical examples of the application of the CHD. In Section 4.4.1, we consider an experiment involving the motion of a shaker system with harmonic distortion. The data obtained from this experiment appear to be at least weakly stationary. For stationary data, only the sine and cosine terms are significant. In Section 4.4.2, we uncover the model parameters from numerically generated data of a cable deformed under the effect of gravity.

4.4.1 An Experimental Example: Harmonic Distortion of a Shaker System

In this section, we implement the CHD described in Sections 4.3.1, 4.3.2, and 4.3.3 to uncover the harmonic distortion of a shaker system. A signal generator provides a sinusoidal command voltage to the shaker amplifier. An accelerometer is studded to a reaction mass attached to the shaker's armature. An acquisition system samples the analog signal from the accelerometer and associated hardware into a record of 160 seconds at the rate of 64 samples per second. The record is carved into 37 ensembles with 75 percent overlap. The duration of each ensemble or sampled window is 16 seconds, as shown in Figure 4.1. The frequency of the sinusoidal command voltage is approximately equal to 10 Hz. However, the excitation frequency is not known *a priori* and periodicity within the sampled window is not ensured.

The first issue is to establish a model order m for the signal. Perhaps, the most common method is to examine the singular values of the singular value decomposition of the covariance matrix $Y^TY = QDQ^T$ or Hankel matrix $Y = PD^{1/2}Q^T$ normalized with the column length of Y. When $D(m+1)$ is small, the model order is m. We demonstrated in Equation (4.35) that Gaussian white noise results in positive contributions to the zero-lag covariance terms $C(i,i)$. In low noise situations, the singular values drop sharply to approximately μ once the appropriate model order has been exceeded, and they maintain the same order of magnitude for subsequent values. Since the smallest singular value does not approach zero even for

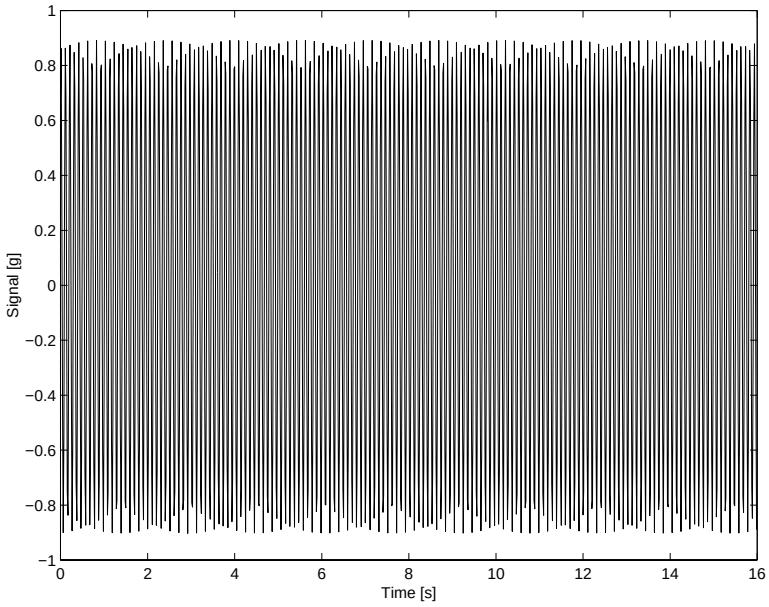

Figure 4.1: An experimental example of an acceleration time series $y(t_\ell)$.

large m, the singular values of Y^TY are termed biased singular values. Sinusoids with mean-squared values of the same order as μ are indistinguishable from noise. Conversely, the smaller singular values of $Y(:, 1:m)^TY(:, m+1:2m)$ do tend towards zero because zero-lag terms are avoided; they are termed unbiased singular values. In moderate noise situations, the unbiased singular values may provide a valuable tool for choosing m when $N \gg 1$.

In Figure 4.2, we show the biased and unbiased singular values for the signal given in Figure 4.1. In this situation, the difference between the biased and unbiased singular values is small, yet noticeable, for the smaller values of m. The biased singular values drop-off sharply from 5dB to -28dB as m exceeds 2 and from -52dB to -65dB as m exceeds 7. Since $D(1)$ and $D(2)$ are much greater than $D(3)$, one is tempted to use $m = 2$. But the singular values above $m = 2$ continue to decrease with increasing m, implying that the next few terms are small deterministic signal components. However, the biased singular values $D(m)$ for $m > 8$ are roughly the order of magnitude of $D(8)$, implying that they may be attributed to noise. We also notice that the value of the unbiased versus biased singular values diverge at $m = 8$, also implying a model order of $m = 8$. We choose the model orders

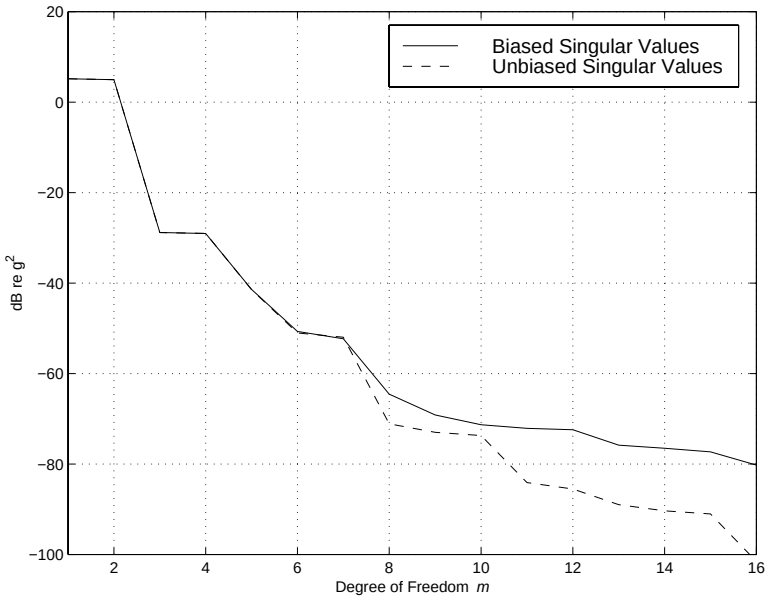

Figure 4.2: An experimental example of singular values: — biased singular values; - - - unbiased singular values.

$m = 2$ and $m = 8$ for the signal. The first choice demonstrates the performance of the CHD in the presence of biased noise due to an under-valued model order. The second choice demonstrates the performance of the CHD with a well-selected model order. The differences between the original signal $y(t_\ell)$ and its estimates $v(t_\ell)$ using the procedure implemented in Section 4.3.1 with model orders $m = 2$ and $m = 8$ are shown in Figures 4.3a and 4.3b, respectively. A comparison of the two figures shows that the error is reduced significantly by increasing the model order from $m = 2$ to $m = 8$. We should also note that the error is large near the start and the end of the record. This can be attributed to the error in the frequency estimates. This is akin to the problem of leakage or wrap around error associated with the DFT [28, 54].

Estimates of the frequency, amplitude, and associated errors with model order $m = 2$ for the three implementations are shown in Table 4.1. The results obtained by implementing the scheme in Section 4.3.2 are quantitatively and qualitatively better than those obtained with the schemes in Sections 4.3.1 and 4.3.3. However, this is not always the case. The model order is smaller than the order of the signal. Hence, the noise is deterministic and biased.

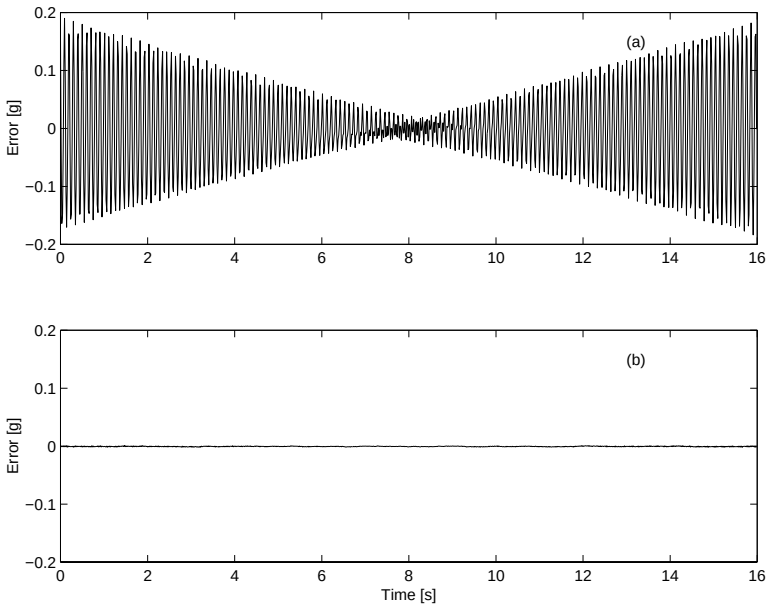

Figure 4.3: An experimental example of the error $\epsilon(t_\ell)$ using the technique of Section 4.3.1: (a) $m = 2$ and (b) $m = 8$.

The form of noise violates the basic assumptions used in the development of the algorithms. Surprisingly, the correlation γ^2 between measured and estimated values is near unity for the first two cases and reasonable for the third one, which implies that the performance of the estimation algorithms is fair.

Table 4.1: An experimental example – mean parameter estimates of 37 ensembles for $n = 1$: () denotes the standard deviation of the preceding parameter estimate.

Method	ω_1 [Hz]	$\lvert p_1 + jq_1 \rvert$ [g]	γ^2	dB (S/N)
§4.3.1	9.80155(0.00038)	0.8887(0.0013)	0.9811	17.2
§4.3.2	9.79857(0.00037)	0.8959(0.0005)	0.9971	25.3
§4.3.3	9.80699(0.00063)	0.8587(0.0048)	0.9161	10.4

Next, we assume that $m = 8$ and implement the CHD for each of the 37 ensembles. The three implementations provide about $30 - 45$dB better results than the results obtained with $m = 2$. This time the decomposition can explain approximately the first 55dB of the signal and the results are more consistent among the various estimation schemes. The signal is composed of the primary frequency, its first and second harmonics, and an extremely small near-zero frequency component. A summary of the mean results is provided in Table 4.2. The components of the first and second harmonics are -34dB and -57dB below the primary tone, respectively. In other words, the total harmonic distortion is about 2.0 %. In Figure 4.4, we show the power spectral density (PSD) of the signal using a boxcar window, the PSD using the CHD (§4.3.1 & $m = 8$), and the PSD of the noise. We note that the implementation procedure of Section 4.3.3 consistently represents the zero, or near zero, frequency component with a small hyperbolic term, rather than a circular one. This emphasizes our assertion in Section 4.3 that the algorithm itself does not enforce an assumption of stationarity.

For comparison, the peak parameters of the DFT are provided in Table 4.3, which demonstrate the sensitivity of the amplitude and phase estimates to the frequency. Here, the effects of leakage associated with the DFT are much more significant than the errors observed for either of the cases documented in Figure 4.3. Each of the three implementations of the CHD describes the signal well.

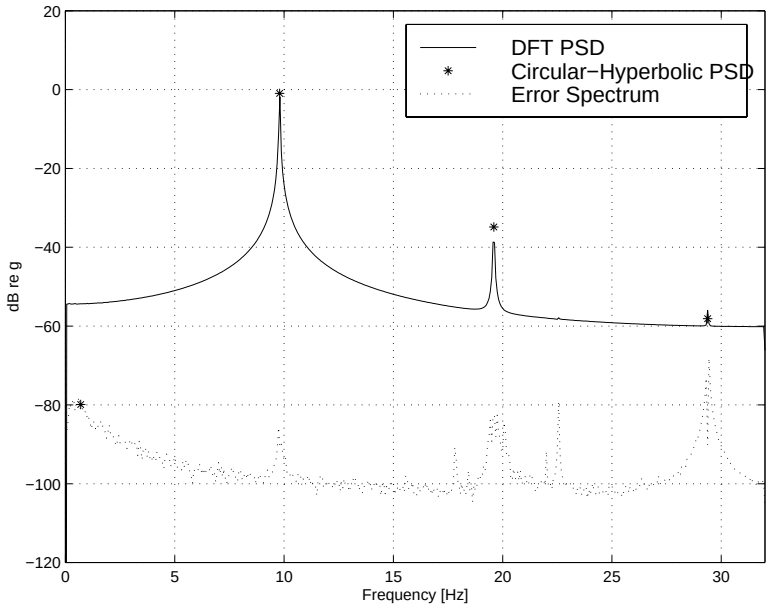

Figure 4.4: An experimental example of the power spectrum: — DFT PSD; * CHD PSD; and - - - error DFT PSD.

Table 4.2: An experimental example – mean parameter estimates of 37 ensembles for $n = 4$: () denotes the standard deviation of the preceding parameter estimate, * denotes the hyperbolic term, and ** near-zero and ill-defined.

Method	ω_i or κ_i* [Hz]	$\lvert p_i + jq_i \rvert$ or $\lvert a_i + jb_i \rvert$* [g]	γ^2	dB (S/N)
§4.3.1	0.699393(0.367055)	0.000101(0.000064)	0.99999	55.2
	9.796872(0.000002)	0.896984(0.000145)		
	19.593836(0.000091)	0.018090(0.000113)		
	29.376525(0.001472)	0.001241(0.000038)		
§4.3.2	0.529780(0.284751)	0.000100(0.000056)	0.99999	55.8
	9.796872(0.000002)	0.896984(0.000144)		
	19.593825(0.000092)	0.018090(0.000113)		
	29.392829(0.000997)	0.001359(0.000025)		
§4.3.3	0.257881(0.142207) *	*,**	0.99999	55.5
	9.796872(0.000015)	0.896985(0.000144)		
	19.593734(0.000096)	0.018090(0.000113)		
	29.399722(0.002036)	0.001317(0.000028)		

Table 4.3: An experimental example – peak amplitudes of the DFT and parameter estimates for a single ensemble for $n = 4$: * denotes the hyperbolic term.

Method	ω_i or κ_i* [Hz]	p_i or a_i* [g]	q_i or b_i* [g]	γ^2	dB (S/N)
§4.3.1	0.424557	0.000011	0.000137	0.99999	53.6
	9.796870	0.604806	-0.661885		
	19.593810	-0.016996	0.006848		
	29.379217	0.000482	0.001168		
§4.3.2	0.332196	0.000094	0.000083	0.99999	53.9
	9.796870	0.604804	-0.661889		
	19.593802	-0.016993	0.006854		
	29.393740	-0.000444	0.001277		
§4.3.3	0.091571 *	0.002675 *	-0.002678 *	0.99999	55.7
	9.796876	0.605007	-0.661712		
	19.593848	-0.017013	0.006810		
	29.402133	-0.000895	0.000942		
DFT	9.8125	0.805861	0.036122		
	19.625	-0.003412	0.010855		
	29.375	0.001227	-0.000963		

Table 4.4: A numerical example – mean parameter estimates and standard deviations for $n = 1$: () denotes the standard deviation of the preceding parameter estimate.

Method	κ_1 $[L^{-1}]$	a_1 $[L]$	b_1 $[L]$	γ^2	dB (S/N)
Actual	0.3	0.6	-0.4	0.999991	50.5
§4.3.1	0.2957(0.0134)	0.5965(0.0107)	-0.3923(0.0233)	0.999882	39.3
§4.3.2	0.2971(0.0132)	0.5962(0.0106)	-0.3946(0.0230)	0.999889	39.6
§4.3.3	0.2993(0.0133)	0.5994(0.0106)	-0.3984(0.0228)	0.999893	39.7

4.4.2 A Numerical Example: Cable Deformation due to Gravity

In this section, we show how a signal composed of a hyperbolic function, with a small Gaussian white noise component, can be analyzed with the techniques discussed in Sections 4.3.1, 4.3.2, and 4.3.3. The frequency and amplitudes are given in Table 4.4. The signal, to be examined here, is generated numerically and corresponds to a cable supported at its ends by two pins and loaded by its own weight. The shape of this cable is hyperbolic. To conduct the proposed analysis, we normalize the signal to a unit length L and sample it given a sampling interval of 0.025 L.

With the obvious assumption that $m = 2$, we conduct 25 trials of the CHD and obtain the mean parameter estimates and standard deviations in Table 4.4. The deterministic part of the signal is the same for all trials, whereas a different set of random numbers is utilized each time to simulate Gaussian white noise.

The performance of the implementations described in Sections 4.3.1, 4.3.2, and 4.3.3 demonstrates a similar performance. In this example, the implementation described in Section 4.3.3 provides marginally better results than the implementations described in Sections 4.3.1 and 4.3.2. A typical example of the results for the implementation described in Section 4.3.3 are graphically documented in Figures 4.5a and 4.5b, representing one trial. The signal-to-noise ratio (S/N) and the correlation γ^2 were calculated on a power averaged basis of all of the trails. Each of the implementations of the procedures in Sections 4.3.1, 4.3.2, and 4.3.3 is able to describe the first 39dB of the signal. The CHD describes the signal well

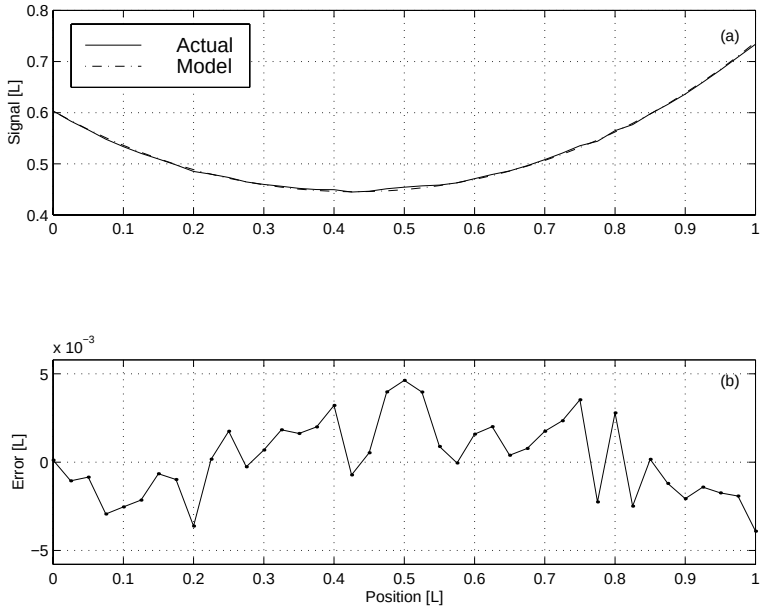

Figure 4.5: A numerical example of the signal $y(t_\ell)$ and the error $\epsilon(t_\ell)$: (a) signal — actual, - - - model; and (b) error Section 4.3.3 with $n = 1$.

and provides exceptional values for the correlation γ^2 between the measured values and the various estimates.

4.5 Summary

In this chapter, we establish constraints on the complex exponential algorithm to limit the estimation procedure to the special case of circular-hyperbolic functions. In sum, the algorithm and constraints are called the circular-hyperbolic decomposition (CHD). Three implementation procedures for this new algorithm are developed. The first is closely related to the least-squares approach of the complex exponential algorithm. The second and third utilize an eigenvalue approach and a covariance approach to avoid zero-lag components, respectively. Experimental and numerical examples of these implementations are provided. They demonstrate that the CHD is able to closely match data that can be represented as a linear combination of sines, cosines, hyperbolic sines, hyperbolic cosines, and their products.

The CHD provides improved amplitude and phase estimates compared to the Discrete Fourier Transform when the frequencies of the circular functions are not integer multiples of each other in moderate noise environments. The present decomposition is applicable to a wide class of problems involving evenly sampled signals composed of circular and hyperbolic sine and cosine functions in the presence of Gaussian white noise.

Chapter 5

Nonlinear Identification of a Single Mode

Characterizing the parameters of a nonlinear model of a system can be undertaken using a number of different methods. One approach involves iterating the parameters of a system of governing equations until data and model are in agreement [35]. This approach has the appeal that one works directly with the governing equations and the data. Another approach involves minimizing an objective function, such as a Euclidean norm, to obtain closed-form estimates. Approximate relationships involving the data and the governing equations are formed and solved in some least-squares sense, either in the time-domain [56, 82, 86, 89, 90] or in the frequency-domain [87, 88]. This approach has the appeal that a solution is obtained in closed-form, although significant data manipulations are sometimes needed; for instance, simultaneous measures in terms of displacement, velocity, and acceleration are often required when only one form of response is available. A third approach involves estimating the Volterra kernels or higher-order frequency-response functions (FRFs) and subsequently uncovering the model parameters [47]. A problem with this method is that it is computationally expensive to estimate the Volterra kernels numerically and impractical from an experimental standpoint. A difficulty with each of these techniques is that the identification procedure does not require data that emphasizes the nonlinearity of the system.

If we had tried to identify the linear parameters of the first mode in Chapter 2 from the part of the FRF around the peak corresponding to the fifth mode, we would be justified from a mathematical standpoint, but not from a practical one. If the nonlinearity is not emphasized, a nonlinear estimation procedure may still not provide good estimates, even if it is mathematically sound.

In this chapter, we advocate exploiting nonlinear resonances as an integral part of the estimation process, as proposed by Nayfeh [59]. Hajj et al. [25], Hajj et al. [26], and Nayfeh et al. [64] demonstrated a proof of principle by estimating the parameters of a nonlinear model of a portal frame. First, they sought and found a nonlinear phenomenon known as principal parametric resonance [57, 58, 63]. Then, they obtained the input power spectra F and output power spectra a. They also uncovered the so-called nonlinear *phase difference* γ via use of higher-order spectral statistics. Finally, they used F, a, and γ, in conjunction with estimation algorithms, to obtain the nonlinear parameters for the frame. In a tandem effort, Fahey and Nayfeh [16] estimated the nonlinear parameters for the same frame using F and a alone, which are within 10% of those given in [64].

In this chapter, we continue this work and describe a procedure for the identification of the nonlinear parameters of a single mode of a structure possessing quadratic and cubic geometric and inertia nonlinearities and linear (viscous), quadratic (airflow drag), and cubic damping. We use it to identify the parameters of the first mode of the two-mass structure, described in Chapter 2. We sought and found a nonlinear phenomenon by exciting the structure near twice the natural frequency of its first mode. The generalized coordinate of this mode is modeled by a second-order ordinary-differential equation possessing quadratic and cubic geometric and inertia nonlinearities, linear, quadratic, and cubic damping, and parametric and external excitation terms. The linear natural frequency and damping coefficient have been estimated using the linear tests described in Chapter 2, which serve as a check on the nonlinear identification procedure. Here, the structure exhibits a behavior consistent with a combination of a principal parametric resonance and a subharmonic resonance of order one-half. We use the method of multiple scales [57, 58] to determine a second-order uniform

expansion of the model equation and hence the response of the structure. We estimate the linear and nonlinear parameters by regressive fits of the theoretically obtained response relations to those obtained experimentally. We report deviations and agreements between model and experiment.

5.1 Introduction

Energy dissipation is often described in terms of a linear damping coefficient. However, damping mechanisms in many systems can not be described by such a simple rule. Linear damping often provides an appropriate engineering description of energy dissipation when aggregate measures are desired. The mathematics of other damping mechanisms can be quite involved and are commonly avoided in practice. Here, we address nonlinear quadratic and cubic damping. For the two-mass structure, we initially suspected a behavior consistent with both viscous damping and airflow drag, from past experience with another structure [16, 64]. It turns out that the energy dissipation of the first mode is more consistent with a combination of linear viscous and nonlinear cubic damping. Thus, we initially incorporate linear, quadratic, and cubic damping terms in the model. We also show that they can be readily separated by the identification technique. In Section 5.5, we outline a qualitative procedure for distinguishing among the various descriptions of energy dissipation. Additional terms for material and other damping mechanisms could also have been included. However, for the present structure, we think that they are either not physically significant or adequately described by linear viscous and nonlinear cubic terms.

The curvature of the structure suggests that the analytical model should include quadratic and cubic geometric terms. Moreover, the concentrated masses lead to quadratic and cubic inertia nonlinearities. These terms can be found by formulating the equations of motion for this system. We show that the resulting model satisfactorily describes moderate-amplitude motions.

The first mode of the structure is a sway mode that is nearly orthogonal to the direction

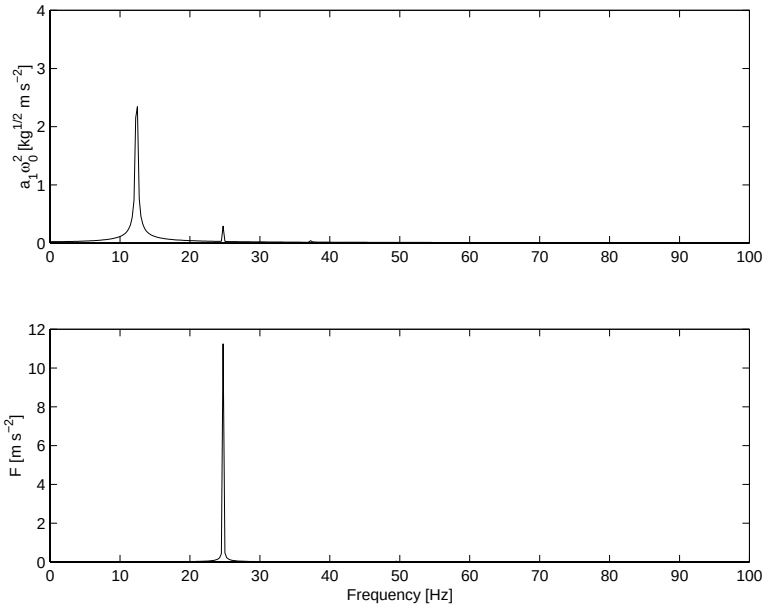

Figure 5.1: Linear spectral density: (top) first-mode acceleration response and (bottom) base acceleration

of the motion of the shaker, as illustrated in Figure 2.6. Hence, the frame is primarily excited by a parametric (multiplicative) component and a small external (additive) component due to asymmetries. This is confirmed by Figure 5.1, which shows that the response of the structure exhibits a small peak at the excitation frequency but the majority of the response is at one-half the excitation frequency. Consequently, the structure is being forced via a principal parametric resonance and a subharmonic resonance of order one-half caused by the quadratic nonlinearity. Hence, we include multiplicative and additive excitation components in the analytical model.

If v denotes the generalized coordinate in terms of the modal displacement of the first mode, then we assume that it is governed by the following mass-normalized second-order nonlinear ordinary-differential equation:

$$\begin{aligned}\ddot{v} + \omega_o^2 v = &-2\mu_1\dot{v} - \mu_2 |\dot{v}| \dot{v} - \mu_3\dot{v}^3 - \alpha_2 v^2 - \alpha_3 v^3 - 2\delta_2 v\ddot{v} - \delta_2\dot{v}^2 \\ &-\delta_3\dot{v}^2 v - \delta_3 v^2\ddot{v} + \eta_1 F\cos(\Omega t) + \eta_2 F v\cos(\Omega t)\end{aligned} \tag{5.1}$$

where ω_0 is the linear natural frequency, $2\mu_1$ is the linear damping coefficient, μ_2 is the

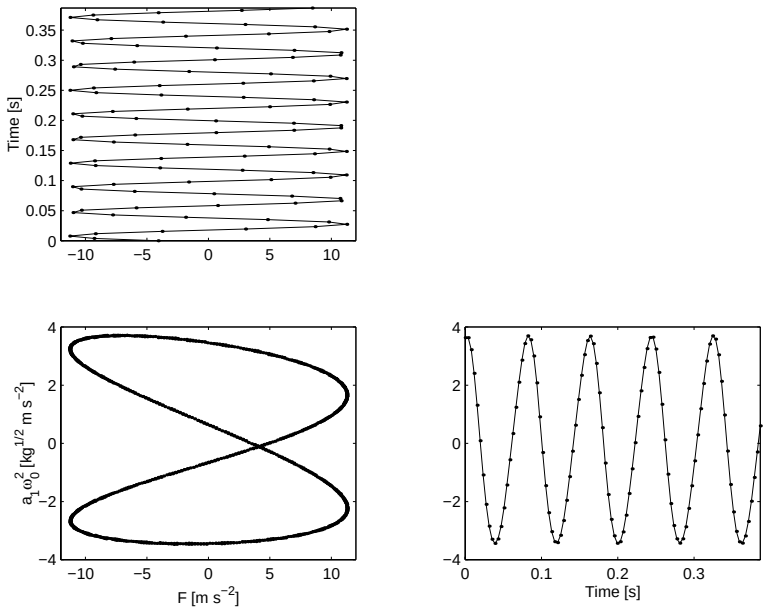

Figure 5.2: X-Y plot of base acceleration versus first-mode acceleration response

quadratic damping coefficient, μ_3 is the cubic damping coefficient, α_2 and α_3 are the coefficients of the quadratic and cubic geometric stiffness nonlinearities, δ_2 and δ_3 are the coefficients of the quadratic and cubic inertia nonlinearities, $F\cos(\Omega t)$ is the excitation, $\eta_1 F\cos(\Omega t)$ is the external (additive) component of the excitation, and $\eta_2 vF\cos(\Omega t)$ is the parametric (multiplicative) component of the excitation. Here $\omega_0, \mu_1, \mu_2, \mu_3, \alpha_2, \alpha_3, \delta_2, \delta_3, \eta_1$, and η_2 are assumed to be constants.

We use the method of multiple scales [57, 58, 63, 65] to generate a second-order approximate solution of Equation (5.1) when $\Omega \approx 2\omega_0$. We use this approximate solution to construct the frequency-response equation that provides the response amplitude a as a function of the excitation parameters F, Ω, η_1, and η_2 and the model parameters ω_0, μ_1, μ_2, μ_3, $\alpha_2, \alpha_3, \delta_2$, and δ_3. We excite the frame and experimentally generate response relations. Then, we estimate the parameters of the model from regressive fits of theoretical response relations to those obtained experimentally.

5.2 Approximate Solution

To determine an approximate solution of Equation (5.1) for weak nonlinearity, we introduce a small nondimensional parameter ϵ as a bookkeeping device and rewrite it as

$$\begin{aligned}\ddot{v}+\omega_o^2 v = &-2\epsilon^2\mu_1\dot{v}-\epsilon^2\mu_2\left|\dot{v}\right|\dot{v}-\epsilon^2\mu_3\dot{v}^3-\epsilon\alpha_2 v^2-\epsilon^2\alpha_3 v^3-2\epsilon\delta_2 v\ddot{v}-\epsilon\delta_2\dot{v}^2\\ &-\epsilon^2\delta_3\dot{v}^2 v-\epsilon^2\delta_3\ddot{v}v^2+\epsilon\eta_1 F\cos\left(\Omega t\right)+\epsilon^2\eta_2 F v\cos\left(\Omega t\right)\end{aligned} \tag{5.2}$$

Using the method of multiple scales [57, 58, 63, 65], we seek a second-order uniform expansion of the solution of Equation (5.2) in the form

$$v = v_0(T_0,T_1,T_2)+\epsilon v_1(T_0,T_1,T_2)+\epsilon^2 v_2(T_0,T_1,T_2)+... \tag{5.3}$$

where $T_0 = t$ is a fast time scale and $T_1 = \epsilon t$ and $T_2 = \epsilon^2 t$ are slow time scales. In terms of T_0, T_1, and T_2, the time derivatives become

$$\begin{aligned} d/dt &= D_0+\epsilon D_1+\epsilon^2 D_2+...\\ d^2/dt^2 &= D_0^2+2\epsilon D_0D_1+\epsilon^2 D_1^2+2\epsilon^2 D_0D_2+...\end{aligned} \tag{5.4}$$

where $D_n = \partial/\partial T_n$. To describe quantitatively the nearness of Ω to $2\omega_0$, we introduce a detuning parameter σ defined by

$$\Omega = 2\omega_0+\epsilon^2\sigma \tag{5.5}$$

Substituting Equations (5.3) and (5.4) into Equation (5.2) and equating coefficients of like powers of ϵ, we obtain

$$D_0^2 v_0+\omega_0^2 v_0 = 0 \tag{5.6}$$

$$D_0^2 v_1+\omega_0^2 v_1 = -2D_0D_1v_0-\alpha_2 v_0^2-2\delta_2 v_0 D_0^2 v_0-\delta_2(D_0v_0)^2+\eta_1 F\cos\left(\Omega T_0\right) \tag{5.7}$$

$$\begin{aligned}D_0^2 v_2+\omega_0^2 v_2 = &-2D_0D_1v_1-2D_0D_2v_0-D_1^2v_0-2\mu_1D_0v_0-\mu_2D_0v_0\left|D_0v_0\right|\\ &-\mu_3(D_0v_0)^3-2\alpha_2v_0v_1-\alpha_3v_0^3-2\delta_2v_0D_0^2v_1-4\delta_2v_0D_0D_1v_0-2\delta_2v_1D_0^2v_0\\ &-2\delta_2D_0v_0D_0v_1-\delta_3\left(D_0v_0\right)^2v_0-\delta_3v_0^2D_0^2v_0+\eta_2Fv_0\cos\left(\Omega T_0\right)\end{aligned} \tag{5.8}$$

The general solution of Equation (5.6) can be expressed as

$$v_0 = A(T_1, T_2)e^{i\omega_0 T_0} + \bar{A}(T_1, T_2)e^{-i\omega_0 T_0} \tag{5.9}$$

where the function $A(T_1, T_2)$ is unknown at this level of approximation; it will be determined by eliminating the secular terms from v_1 and v_2. Substituting Equation (5.9) into Equation (5.7) yields

$$\begin{aligned} D_0^2 v_1 + \omega_0^2 v_1 = &-2i\omega_0 D_1 A e^{i\omega_0 T_0} + 2i\omega_0 D_1 \bar{A} e^{-i\omega_0 T_0} - (\alpha_2 - 3\delta_2\omega_0^2)A^2 e^{2i\omega_0 T_0} \\ &-2(\alpha_2 - \delta_2\omega_0^2)A\bar{A} - (\alpha_2 - 3\delta_2\omega_0^2)\bar{A}^2 e^{-2i\omega_0 T_0} + \frac{1}{2}\eta_1 F e^{i\Omega T_0} + \frac{1}{2}\eta_1 F e^{-i\Omega T_0} \end{aligned} \tag{5.10}$$

Eliminating the terms that produce secular terms in v_1, we have

$$D_1 A = 0, \quad \text{or} \quad A = A(T_2) \tag{5.11}$$

Then, the solution of Equation (5.10) can be written as

$$\begin{aligned} v_1 = &-2\frac{\alpha_2 - \delta_2\omega_0^2}{\omega_0^2}A\bar{A} + \frac{\alpha_2 - 3\delta_2\omega_0^2}{3\omega_0^2}A^2 e^{2i\omega_0 T_0} + \frac{\alpha_2 - 3\delta_2\omega_0^2}{3\omega_0^2}\bar{A}^2 e^{-2i\omega_0 T_0} \\ &-\frac{\eta_1}{6\omega_0^2}F e^{i\Omega T_0} - \frac{\eta_1}{6\omega_0^2}F e^{-i\Omega T_0} \end{aligned} \tag{5.12}$$

where use has been made of the fact that $\Omega \approx 2\omega_0$.

Substituting Equations (5.9) and (5.12) into Equation (5.8) yields

$$\begin{aligned} &D_0^2 v_2 + \omega_0^2 v_2 = -2i\omega_0 \left(A' + \mu_1 A\right) e^{i\omega_0 T_0} \\ &+ \left(\frac{10\alpha_2^2}{3\omega_0^2} - 4\alpha_2\delta_2 - 2\delta_2^2\omega_0^2 - 3\alpha_3 + 2\delta_3\omega_0^2\right) A^2 \bar{A} e^{i\omega_0 T_0} \\ &+ \left[\frac{(\alpha_2 - \delta_2\omega_0^2)\eta_1}{3\omega_0^2} + \frac{1}{2}\eta_2\right] F A e^{i(\Omega+\omega_0)T_0} \\ &- \left(\frac{2\alpha_2^2}{3\omega_0^2} - \frac{20}{3}\alpha_2\delta_2 + 14\delta_2^2\omega_0^2 + \alpha_3 - 2\delta_3\omega_0^2\right) A^3 e^{3i\omega_0 T_0} \\ &+ \left[\frac{(\alpha_2 - 3\delta_2\omega_0^2)\eta_1}{3\omega_0^2} + \frac{1}{2}\eta_2\right] F \bar{A} e^{i(\Omega-\omega_0)T_0} + cc \\ &-\mu_2\left(i\omega_0 A e^{i\omega_0 T_0} - i\omega_0 \bar{A} e^{i\omega_0 T_0}\right)\left|i\omega_0 A e^{i\omega_0 T_0} - i\omega_0 \bar{A} e^{i\omega_0 T_0}\right| \\ &-\mu_3\left(i\omega_0 A e^{i\omega_0 T_0} - i\omega_0 \bar{A} e^{-i\omega_0 T_0}\right)^3 \end{aligned} \tag{5.13}$$

where cc stands for the complex conjugate of the preceding terms. Using Equation (5.5) and eliminating the terms that produce secular terms from Equation (5.13), we obtain

$$2i\omega_0\left(A' + \mu_1 A\right) + 8\alpha_e A^2\bar{A} - 2\eta_e F\bar{A}e^{i\sigma T_2} + \mu_2\hat{g} + 3i\omega_0^3\mu_3 A^2\bar{A} = 0 \tag{5.14}$$

where

$$\hat{g} = \frac{\omega_0}{2\pi}\int_0^{2\pi/\omega_0} i\omega_0\left(Ae^{i\omega_0 T_0} - \bar{A}e^{-i\omega_0 T_0}\right)\left|i\omega_0\left(Ae^{i\omega_0 T_0} - \bar{A}e^{-i\omega_0 T_0}\right)\right| e^{-i\omega_0 T_0} dT_0 \tag{5.15}$$

$$\eta_e = \frac{1}{4}\eta_2 + \frac{\alpha_2 - 3\delta_2\omega_0^2}{6\omega_0^2}\eta_1 \tag{5.16}$$

$$8\alpha_e = 3\alpha_3 - 2\delta_3\omega_0^2 - \frac{10\alpha_2^2}{3\omega_0^2} - 4\alpha_2\delta_2 + 2\delta_2^2\omega_0^2 \tag{5.17}$$

It follows from Equations (5.14) and (5.16) that α_e is an effective nonlinear coefficient and that $\eta_e F$ is an effective principal parametric excitation amplitude. The additive excitation $\eta_1 F\cos\Omega t$ contributes $F\left(\alpha_2 - 3\delta_2\omega_0^2\right)\eta_1/6\omega_0^2$ to the effective principal parametric coefficient η_e.

Next, we express A in the polar form

$$A = \frac{1}{2}ae^{i\beta} \tag{5.18}$$

separate real and imaginary parts in Equation (5.14), and obtain

$$\omega_0 a' = -\omega_0\mu_1 a - \frac{4\omega_0^2\mu_2}{3\pi}a^2 - \frac{3\omega_0^3\mu_3}{8}a^3 + \eta_e F a\sin\gamma \tag{5.19}$$

$$\frac{1}{2}\omega_0 a\gamma' = \frac{1}{2}\omega_0 a\sigma - \alpha_e a^3 + \eta_e F a\cos\gamma \tag{5.20}$$

where

$$\gamma = \sigma T_2 - 2\beta \tag{5.21}$$

Combining Equations (5.3), (5.9), (5.12), (5.18), and (5.21), we obtain

$$\begin{aligned} v = {} & a\cos\left(\frac{1}{2}\Omega t - \frac{1}{2}\gamma\right) \\ & -\epsilon\left[\frac{\alpha_2 - \delta_2\omega_0^2}{2\omega_0^2}a^2 + \frac{\alpha_2 - 3\delta_2\omega_0^2}{6\omega_0^2}a^2\cos\left(\Omega t - \gamma\right) - \frac{\eta_1}{3\omega_0^2}F\cos\Omega t\right] + \cdots \end{aligned} \tag{5.22}$$

where a and γ are given by Equations (5.19) and (5.20). It is clear from Equation (5.22) that spectral components at DC, $\frac{1}{2}\Omega$, and Ω are expected in the response of the frame to an excitation with frequency Ω.

As shown in Figure 5.1, higher-order harmonics, although small, are present in both the reference and response signals. The level of approximation considered does not capture the entire harmonic character. The potential of structure-shaker interactions and power quality issues are also ignored. This approach is justified by observing that the most significant effects, by several orders of magnitude, are explained by the reference harmonic at Ω, the DC component, and the response harmonic at $\frac{1}{2}\Omega$, as predicted.

5.3 Periodic Motions

Periodic motions of v correspond to constant a and γ; that is, the fixed points or equilibrium solutions of Equations (5.19) and (5.20). Letting $a' = 0$ and $\gamma' = 0$ in Equations (5.19) and (5.20), we obtain either $a = 0$ or

$$\omega_0\mu_1 + \frac{4\omega_0^2}{3\pi}\mu_2 a + \frac{3\omega_0^3}{8}\mu_3 a^2 = \eta_e F \sin\gamma \tag{5.23}$$

$$\alpha_e a^2 - \frac{1}{2}\omega_0\sigma = \eta_e F \cos\gamma \tag{5.24}$$

We square Equations (5.23) and (5.24), add the results, and obtain the frequency-response equation

$$\eta_e^2 F^2 = \left(\omega_0\mu_1 + \frac{4\omega_0^2}{3\pi}\mu_2 a + \frac{3\omega_0^3}{8}\mu_3 a^2\right)^2 + \left(\alpha_e a^2 - \frac{1}{2}\omega_0\sigma\right)^2$$

which can be manipulated to give

$$\alpha_e a^2 = \frac{1}{2}\omega_0\sigma \pm \sqrt{\eta_e^2 F^2 - \left(\omega_0\mu_1 + \frac{4\omega_0^2}{3\pi}\mu_2 a + \frac{3\omega_0^3}{8}\mu_3 a^2\right)^2} \tag{5.25}$$

For a given $\alpha_e, \eta_e F, \omega_0, \mu_1, \mu_2$, and μ_3 one can produce frequency-response curves; that is, one can plot a vs. σ. These curves are bent to the right when $\alpha_e > 0$, and one speaks of

a hardening nonlinearity. When $\alpha_e < 0$, the frequency-response curves are bent to the left, and one speaks of a softening nonlinearity.

There are a number of observations that can be made about the nature of a principal parametric resonance or a subharmonic resonance of order one-half. A necessary condition for the response amplitude a is that it must be real-valued and positive. Accordingly, the quantity under the radical in Equation (5.25) must be greater than or equal to zero. Hence, neither a principal parametric resonance nor a subharmonic resonance of order one-half can be activated when $F < F_{min}$, where

$$F_{min} = \left| \frac{\mu_1 \omega_0}{\eta_e} \right| \tag{5.26}$$

The linear damping and effective forcing are the parameters that control the stability boundary for small disturbances, where neither a principal parametric nor a subharmonic resonance of order one-half can be activated. Clearly, lightly damped structures are more vulnerable to such resonances than heavily damped structures. Equation (5.26) demonstrates that these resonances can be activated with a sufficient equivalent principal parametric force $\eta_e F$. It follows from Equation (5.16) that the contribution of the subharmonic resonance of order one-half to η_e depends on the quadratic nonlinearities, but the contribution of the principal parametric resonance is independent of these nonlinearities.

As F exceeds F_{min}, the trivial solution $a = 0$ undergoes either a pitchfork or a transcritical bifurcation, depending on whether μ_2 is zero or not. In the $\sigma - F$ plane, the locations of these bifurcations are given by

$$\frac{1}{2}\omega_0 \sigma = \pm \sqrt{\eta_e^2 F^2 - \mu_1^2 \omega_0^2} \tag{5.27}$$

We observe that for a given excitation level F, in the presence of nonlinear damping, there is an upper bound for the response amplitude a. The nonlinear damping causes the branches of stable and unstable solutions to collide and destroy one another in a saddle-node (S-N) bifurcation, see [65]. In this situation, the quantity under the radical sign in Equation (5.25) must equal zero. Accordingly, the maximum response amplitude for a given excitation

amplitude is given as a solution of

$$|\eta_e|F = \omega_0\mu_1 + \frac{4\omega_0^2}{3\pi}\mu_2 a + \frac{3\omega_0^3}{8}\mu_3 a^2 \tag{5.28}$$

If μ_1, μ_2, and μ_3 are all positive, only one positive solution for a_{max} will be obtained. In the case of negative damping, additional consideration may be required.

Equation (5.28) can be specialized for several particular cases of interest. Case I, linear damping (i.e., $\mu_2 = \mu_3 = 0$):

$$|\eta_e|F = \omega_0\mu_1 \tag{5.29}$$

which has no dependence on a. Thus, if the drag and cubic damping were neglected, then the model would predict an unbounded upper limit for the response amplitude. Case II, linear and quadratic damping (i.e., $\mu_3 = 0$):

$$a_{max} = \frac{3\pi}{4\mu_2\omega_0^2}\left(|\eta_e|\,F - \mu_1\omega_0\right) \tag{5.30}$$

Clearly, a_{max} varies inversely with the drag coefficient μ_2. Case III, linear and cubic damping (i.e., $\mu_2 = 0$):

$$a_{max}^2 = \frac{8}{3\mu_3\omega_0^3}\left(|\eta_e|\,F - \mu_1\omega_0\right) \tag{5.31}$$

Clearly, the square of a_{max} varies inversely with the cubic damping coefficient. We can utilize these qualitative differences to uncover the form of damping, which will be pursued in our consideration of the present structure.

5.4 Experiment

We illustrate the geometry of the structure in Figures 2.1 and 2.2. The experimental apparatus is described in Chapter 2. Briefly, the excitation is measured by an accelerometer studded to the base. The response of the structure is measured using three accelerometers. The locations for these accelerometers are chosen with the intent of distinguishing among

the first three modes. The other modes of the structure are ignored with the justifications that their frequencies are well separated from the first mode and that they were not observed in the response during preliminary testing, as detailed in Chapter 3.

The structure is fixed to a vertical $4000N$ $(900lbf.)$ shaker table, as shown in Figure 2.2. The structure is excited via base excitation. A signal generator is used to drive the shaker amplifier. The data are acquired using a four-channel dynamic signal analyzer in the time-capture mode, which also provides amplification and signal conditioning for the accelerometers.

The structure is excited near twice the natural frequency of its first mode. The experiment includes two testing sequences, which are run on separate days. Several checks for reproducibility of the data show reasonable consistency among the sequences. The checks include comparing previously determined responses for a given excitation frequency and amplitude. In the first testing sequence, both the excitation amplitude and frequency are varied slowly in order to trace-out the approximate boundary for the S-N bifurcation, called the S-N diagram. In the second testing sequence, the frequency is swept while the excitation amplitude is held nearly constant to obtain a frequency-response curve. All calculations include observed variations in the excitation amplitude. Before any measurement is taken, we wait for a significant period of time to ensure steady state so that neither amplitude nor frequency modulations of either the excitation or the response exist, within experimental precision.

Figure 5.2 graphically demonstrates the relationship between the excitation and the response. This figure is crudely akin to the sine-dwell approach once used for modal analysis, where shakers are carefully tuned until the forcing and the response acceleration are 90 degrees out of phase, indicating resonance. For sine-dwell testing, plotting the excitation amplitude versus the response demonstrates linear amplitude and phase relations. In Figure 5.2, we observe a figure-eight profile, which demonstrates a stationary two-to-one periodic *phased-locked* relation between the excitation and the response.

In Figures 5.1 and 5.2, we report response results in terms of the modal acceleration $\ddot{v}$,

but our data is in terms of physical accelerations $\ddot{x}$. For parameter estimation purposes, we express the response of the structure in terms of the modal displacements because this is how our model is phased. We can easily project the physical accelerations of the system onto either the modal displacements or the modal accelerations. We began by uncovering the Fourier components of the acceleration of the structure via the Circular-Hyperbolic Decomposition of Chapter 4. If need be, we calculate equivalent Fourier components in terms of the structure's displacement by twice dividing each component by its pure imaginary circular frequency. Then, we transform the structure's displacements into mass-normalized modal displacements via

$$V = \tilde{\Phi}^{-1} X \tag{5.32}$$

where $\tilde{\Phi}$, V, and X denote the mass-normalized mode shapes of Equation (2.16), the mass-normalized Fourier components of the modal displacements, and the Fourier components of the structure's displacements, respectively. We note that X and V are arranged column-wise and have units of m and $kg^{1/2}m$, respectively. We also note that any zero-frequency component can not be uncovered by such a procedure. Additionally, our accelerometers have a frequency range that excludes zero- and near-zero-frequency components; that is, we are unable to recover the DC component. Although, we find in the next section that our inability to uncover the DC component results in a corresponding inability to decouple the quadratic geometric and inertia nonlinearities. In a similar way, we transform the structure's accelerations into mass-normalized modal accelerations via

$$\ddot{V} = \tilde{\Phi}^{-1} \ddot{X} \tag{5.33}$$

where the overdot represents differentiation with respect to time.

5.5 Parameter Estimation

In Chapter 2, we examined the linear system parameters of the two-mass structure via experimental observation of its free-decay response and its response to an impact excitation.

These linear frequency and damping estimate serve as a check for the nonlinear parameter-estimation procedure outlined in this section.

There are three steps in the present procedure. First, we use the S-N diagram to uncover the form of damping and the damping parameters themselves. Then, we examine the harmonic response at the excitation frequency to uncover a lumped estimate of the quadratic geometric and inertia nonlinearities and the external excitation coefficient. Finally, we uncover the effective nonlinear coefficient and the effective principal parametric coefficient, which are lumped estimates of the quadratic and cubic geometric and inertia nonlinearities, and the external and parametric excitation coefficients, respectively.

To begin, the dynamic characteristics of the first mode of the structure are assumed to be governed by Equation (5.1). We examine the response of the structure to an excitation at nearly twice the natural frequency of the first mode. A large-amplitude response was observed near the natural frequency of the system. Assuming linear, quadratic, and cubic damping, we find that Equations (5.28) describes the location of the S-N bifurcation. Equations (5.29)-(5.31) represent the special cases of linear, linear and quadratic, and linear and cubic damping, respectively. If we assume that the energy dissipation can be described in terms of linear damping and quadratic drag, we can rewrite Equation (5.30) as

$$\{\omega_0\}\,\frac{\mu_1}{|\eta_e|} + \left\{\frac{4\omega_0^2}{3\pi}a\right\}\frac{\mu_2}{|\eta_e|} = \{F\} \tag{5.34}$$

We exploit this S-N condition to estimate the damping coefficients. Unfortunately, S-N bifurcations are not directly observable from the experiment. Therefore, we find 8 stable fixed points that are very close to the S-N bifurcation and assume that they are close enough for parameter-estimation purposes. The excitation and response amplitudes were calculated as the mean amplitude of 10 ensembles, which were also used to calculate the two standard-deviation bounds in Figure 5.3. Equation (5.34) is utilized to obtain the damping-parameter

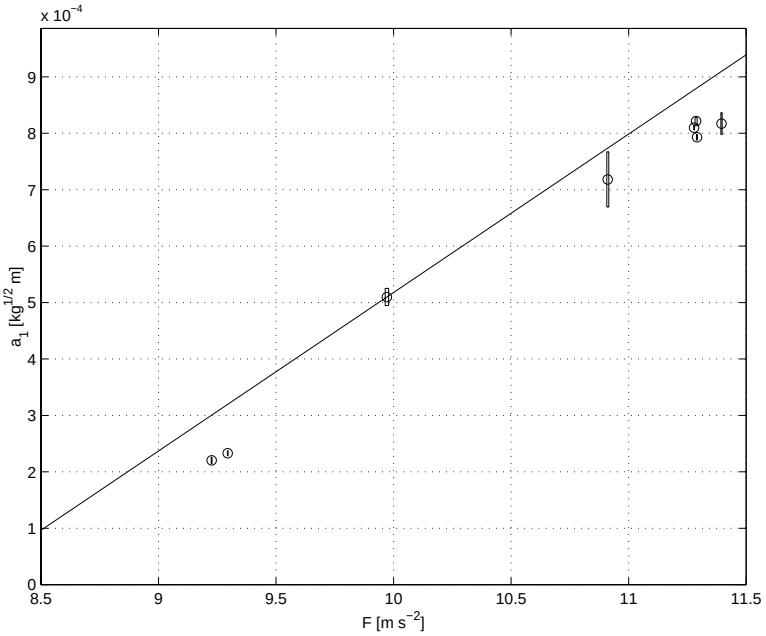

Figure 5.3: Saddle-node diagram, first-mode amplitude versus excitation amplitude: (o) estimated first-mode and excitation amplitudes, ([]) two-standard deviation bound, and (-) a S-N fit assuming linear and quadratic damping

estimates by minimizing a Euclidean norm according to

$$\left\{ \begin{array}{c} \frac{\mu_1}{|\eta_e|} \\ \frac{\mu_2}{|\eta_e|} \end{array} \right\} = \left[\begin{array}{cc} \omega_0 & \frac{4\omega_0^2}{3\pi} a_1 \\ \omega_0 & \frac{4\omega_0^2}{3\pi} a_2 \\ \vdots & \vdots \\ \omega_0 & \frac{4\omega_0^2}{3\pi} a_8 \end{array} \right]^+ \left\{ \begin{array}{c} F_1 \\ F_2 \\ \vdots \\ F_8 \end{array} \right\} \tag{5.35}$$

However, the observed fixed points must all be on the right-hand side of the S-N bifurcation line. Thus, we decrease the estimate of the linear damping until this condition is satisfied, which we illustrate in Figure 5.3. We note that the fixed points appear to diverge from the estimated S-N bifurcation line, which suggests that the assumed form of damping may not be appropriate.

We repeat the same general procedure assuming linear and cubic damping alone. We

rewrite Equation (5.31) as

$$\{\omega_0\}\frac{\mu_1}{|\eta_e|}+\left\{\frac{3\omega_0^3}{8}a^2\right\}\frac{\mu_3}{|\eta_e|}=\{F\} \tag{5.36}$$

Equation (5.36) is utilized to obtain parameter estimates by minimizing a Euclidean norm according to

$$\left\{\begin{array}{c}\frac{\mu_1}{|\eta_e|}\\ \frac{\mu_3}{|\eta_e|}\end{array}\right\}=\left[\begin{array}{cc}\omega_0 & \frac{3\omega_0^3}{8}a_1^2\\ \omega_0 & \frac{3\omega_0^3}{8}a_2^2\\ \vdots & \vdots\\ \omega_0 & \frac{3\omega_0^3}{8}a_8^2\end{array}\right]^+\left\{\begin{array}{c}F_1\\ F_2\\ \vdots\\ F_8\end{array}\right\} \tag{5.37}$$

As before, we decrease the estimate of the linear damping so that all of the observed fixed points are on the right-hand side of the S-N bifurcation line, which we illustrate in Figure 5.4. Now, the fixed points appear to be in better agreement with the estimated S-N bifurcation line.

This exercise demonstrates how we can determine the form of energy dissipation by examining the qualitative appearance of the S-N bifurcation diagram. Physically the S-N bifurcation represents the location where the energy added to the system by the excitation is less than the dissipated energy. Had the damping been linear, then the S-N bifurcation line would have been independent of a, which is not the case. Had the energy dissipation be linear and quadratic, the S-N bifurcation line would be affine when plotting a versus F. In Figure 5.3, the observed fixed points are clearly not affine. When energy dissipation can be described in terms of linear and cubic damping, the S-N bifurcation line should be affine when plotting a^2 versus F. This description provides the best explanation of the data among these three choices. We could certainly include a quadratic term, but it does not appear to be physically justified. We neglect the quadratic damping term and obtain the parameter estimates documented in Table 5.1.

Examining Equation (5.22), we find that it is possible to estimate $(\alpha_2-3\delta_2\omega_0^2)/6\omega_0^2$ and $\eta_1/3\omega_0^2$ by comparing $V(\Omega)$, $V(\Omega/2)$, and $\bar{F}$, which are the one-sided Fourier coefficients of the response at the excitation frequency, the response at half of the excitation frequency,

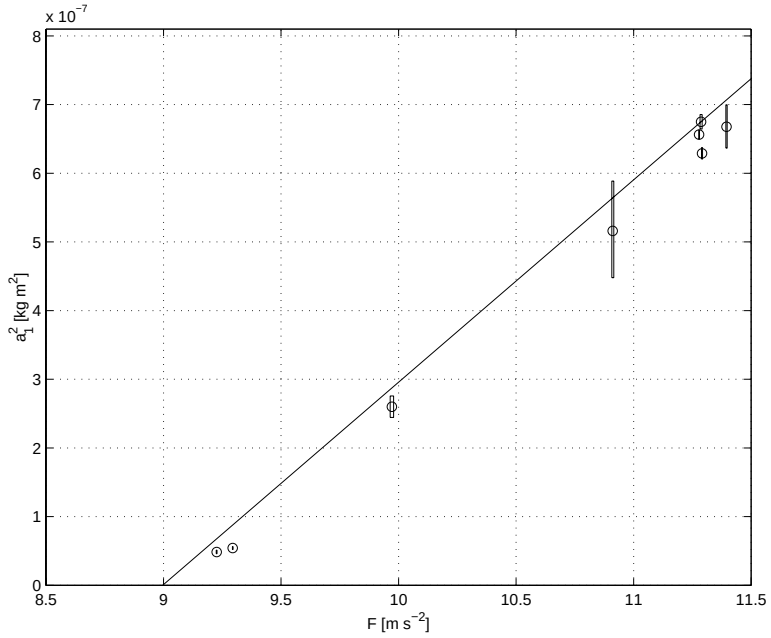

Figure 5.4: Saddle-node diagram that shows the square amplitude of the first mode versus the excitation amplitude: (o) estimated first-mode and excitation amplitudes, ([]) an estimate of a two-standard-deviation bound, and (-) a S-N fit assuming linear and cubic damping

Table 5.1: Linear and cubic damping coefficients.

$\mu_1/\lvert\eta_e\rvert$ $[m\ s^{-1}]$	$\mu_3/\lvert\eta_e\rvert$ $[kg^{-1}m^{-1}s]$
0.1155	19.18

and the response at the excitation frequency, respectively. Care must be taken to use the one-side Fourier coefficients (e.g., $|V(\Omega/2)| = a$ and $|\bar{F}| = F$), otherwise $(\alpha_2 - 3\delta_2\omega_0^2)/6\omega_0^2$ will be off by a factor of 2. Equation (5.22) is used to obtain the parameter estimates by minimizing a Euclidean norm according to

$$\left\{ \begin{array}{c} \frac{\alpha_2 - 3\delta_2\omega_0^2}{6\omega_0^2} \\ \frac{\eta_1}{3\omega_0^2} \end{array} \right\} = \left[\begin{array}{cc} \mathrm{Re}[V_1^2(\Omega/2)] & \mathrm{Re}[\bar{F}_1] \\ \mathrm{Re}[V_2^2(\Omega/2)] & \mathrm{Re}[\bar{F}_2] \\ \vdots & \vdots \\ \mathrm{Re}[V_{10}^2(\Omega/2)] & \mathrm{Re}[\bar{F}_{10}] \\ \mathrm{Im}[V_1^2(\Omega/2)] & \mathrm{Im}[\bar{F}_1] \\ \mathrm{Im}[V_2^2(\Omega/2)] & \mathrm{Im}[\bar{F}_2] \\ \vdots & \vdots \\ \mathrm{Im}[V_{10}^2(\Omega/2)] & \mathrm{Im}[\bar{F}_{10}] \end{array} \right]^+ \left\{ \begin{array}{c} \mathrm{Re}[V_1(\Omega)] \\ \mathrm{Re}[V_2(\Omega)] \\ \vdots \\ \mathrm{Re}[V_{10}(\Omega)] \\ \mathrm{Im}[V_1(\Omega)] \\ \mathrm{Im}[V_2(\Omega)] \\ \vdots \\ \mathrm{Im}[V_{10}(\Omega)] \end{array} \right\} \tag{5.38}$$

where Re[ ] and Im[ ] denote the real and imaginary parts of the quantity inside of the braces, which constrain the coefficients on the left-hand side to be real-valued. We consider the sum of the data obtained in searching for the S-N bifurcation line and the data obtained in tracing out the frequency-response curve. Each of these measurement series involves 10 ensembles. We apply Equation (5.38) repeatedly for each ensemble to obtain the results shown in Figures 5.5 and 5.6. Then, we calculate the mean values and associated standard deviations, which are provided in Table 5.2. Here, $(\alpha_2 - 3\delta_2\omega_0^2)/6\omega_0^2$ can not be statistically distinguished from zero. The estimates of $(\alpha_2 - 3\delta_2\omega_0^2)/6\omega_0^2$ also appear to have a divergent trend for smaller modal amplitudes a. Furthermore, if we had been able to uncover the DC component, we could have decoupled the quadratic geometric and inertia nonlinearities. This can be a concern particularly in situations involving cancelation effects; that is, α_2 and δ_2 could be significant and yet $(\alpha_2 - 3\delta_2\omega_0^2)/6\omega_0^2$ could be insignificant (e.g., $1 - 1 = 0$).

To estimate the effective nonlinearity α_e and excitation η_e coefficients, we rewrite Equation (5.25) as

$$\left\{a^2\right\}\alpha_e - \left\{ \sqrt{F^2 - \left(\omega_o \frac{\mu_1}{|\eta_e|} + \frac{3\omega_0^3}{8}\mu_3 a^2 \right)^2} \right\} |\eta_e| = \left\{ \frac{1}{2}\omega_o \sigma \right\} \tag{5.39}$$

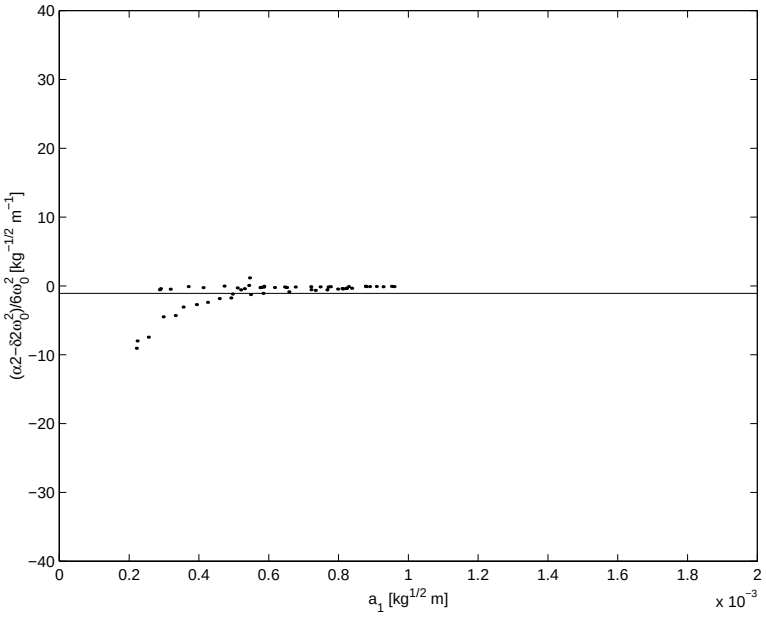

Figure 5.5: Estimates of $(\alpha_2 - 3\delta_2\omega_0^2)/6\omega_0^2$ versus the first-mode amplitude

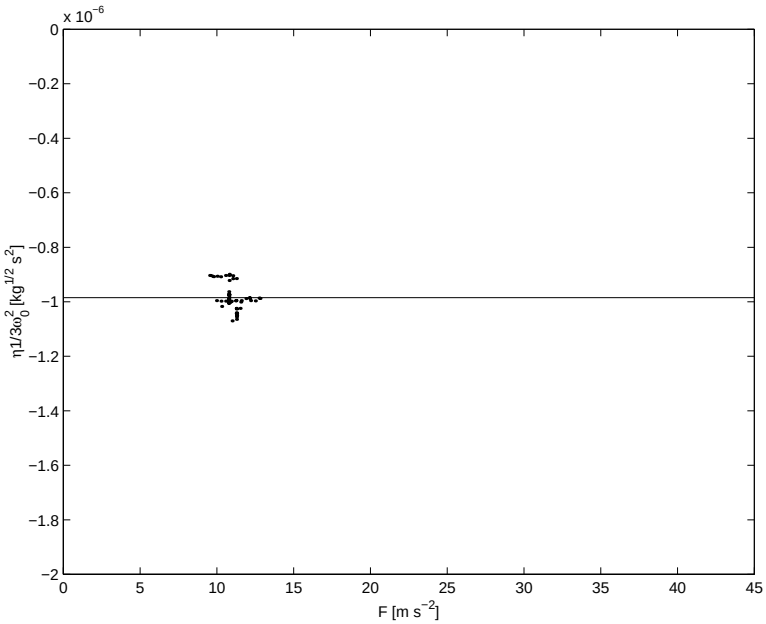

Figure 5.6: Estimates of $\eta_1/3\omega_0^2$ versus the excitation amplitude

Table 5.2: Quadratic geometric, quadratic inertia, and external excitation coefficients: () denotes the standard deviation of the preceding parameter estimate.

$(\alpha_2 - \delta_2\omega_0^2)/6\omega_0^2$ $[kg^{-1/2}m^{-1}]$	$\eta_1/3\omega_0^2$ $[kg^{1/2}s^2]$
$-1.070(2.022)$	$-0.985 \times 10^{-6}(0.0482 \times 10^{-6})$

Table 5.3: Effective nonlinear stiffness and effective coefficient of parametric excitation.

α_e $[kg^{-1}m^{-2}s^{-2}]$	$\lvert\eta_e\rvert$ $[m^{-1}]$
-42.5×10^6	1.922

The frequency-response curve, shown in Figure 5.7, contains 110 experimental data points, which represent ten ensembles from each of eleven excitation conditions. In a forward frequency sweep, the response becomes nontrivial and *jumps-up* as the excitation frequency exceeds 24.74 Hz ($\Omega/2 = 12.37$ Hz). In a reverse sweep, the response becomes nontrivial as the excitation frequency decreases below 24.82 Hz ($\Omega/2 = 12.41$ Hz).

If we take the linear estimate of the natural frequency as 12.419 Hz from Table 2.4, we obtain poor results. Therefore, we are motivated to use other means. The intersections of the stable and unstable solutions with the null solution are symmetric, see Equation (5.27). Thereby, we take the nonlinear estimate of the natural frequency as the average value of the first nontrivial response frequencies on the forward and reverse frequency sweeps; that is, we take $\omega_0 = 12.39$ Hz ($\omega_0 = (12.37 + 12.41)/2$ Hz). Furthermore, this frequency estimate is within one standard deviation of the linear-frequency estimate in Table 4.2 and provides reasonable results.

Equation (5.39) is used to obtain estimates of α_e and $|\eta_e|$ by minimizing a Euclidean norm according to

$$\left\{ \begin{array}{c} \alpha_e \\ |\eta_e| \end{array} \right\} = \left[\begin{array}{cc} a_1^2 & -\tilde{F}_1 \\ a_2^2 & -\tilde{F}_2 \\ \vdots & \vdots \\ a_{110}^2 & -\tilde{F}_{110} \end{array} \right]^+ \left[\begin{array}{c} \frac{1}{2}\omega_0\sigma_1 \\ \frac{1}{2}\omega_0\sigma_2 \\ \vdots \\ \frac{1}{2}\omega_0\sigma_{110} \end{array} \right] \tag{5.40}$$

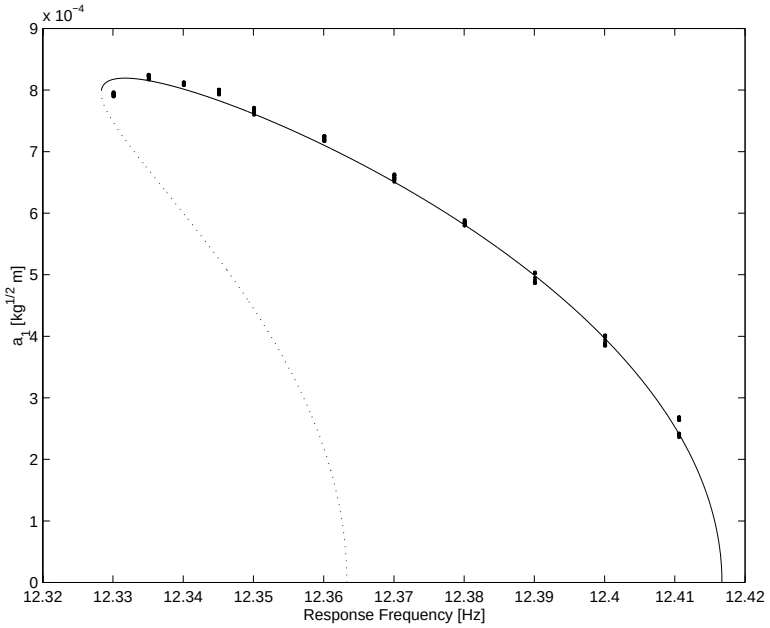

Figure 5.7: Frequency-response curve, $F = 22.55m \ \ s^{-2}$

Table 5.4: Summary of results: () denotes the standard deviation of the preceding parameter estimate.

$\alpha_e \ [kg^{-1}m^{-2}s^{-2}]$	-10.62×10^6
$(\alpha_2 - \delta_2\omega_0^2)/6\omega_0^2 \ [kg^{-1/2}m^{-1}]$	$-0.535(1.011)$
$\mu_1 \ [s^{-1}]$	0.222
$\mu_3 \ [kg^{-1}m^{-2}s]$	36.87
$\eta_e \ [m^{-1}]$	1.922
$\eta_1 \ [kg^{1/2}]$	$-17.99 \times 10^{-3}(0.877 \times 10^{-3})$

where $\tilde{F}_k = \left[F_k^2 - (\omega_o \mu_1/|\eta_e| + 3\omega_0^3 \mu_3 a_k^2/8|\eta_e|)^2\right]^{1/2}$. The results are provided in Tables 5.3. We note that we are not able to separate the components of the effective nonlinear coefficient α_e. A summary of all of the parameters that were estimated in this section are provided in Table 5.4. An overlay of the experimental and estimated frequency-response curves are shown in Figure 5.7. The experimental and estimated frequency-response curves are generally in good agreement.

5.6 Summary

In this chapter, we describe a procedure that exploits nonlinear resonances (principal parametric resonance and subharmonic resonance of order one-half) to identify the nonlinear parameters of a single structural mode. This procedure utilizes observed spectral amplitudes and an approximate solution obtained using the method of multiple scales to identify the parameters of the first mode of a two-mass structure. The dynamic characteristics of this mode are modeled with a second-order ordinary-differential equation possessing quadratic and cubic geometric and inertia nonlinearities, linear and cubic damping, and multiplicative and additive excitation terms with the excitation frequency being near twice the linear natural frequency of this mode. The linear natural frequency and damping coefficient are estimated using very small-amplitude free-oscillation data. Then, the structure is excited near twice the natural frequency of its first mode, and a saddle-node diagram and a frequency-response curve are generated. We also use the method of multiple scales to determine a second-order uniform expansion of the solution of the model equation. Then, we form regressive relationships between the theoretically obtained response relations and the experimental results and estimate the linear and cubic damping coefficients, the external excitation coefficient, a lumped estimate of the quadratic geometric and inertia nonlinearity, the effective nonlinearity, and the effective principal-parametric excitation amplitude. We utilize these parameter estimates to generate a saddle-node diagram and a frequency-response curve. Comparison between the experimental data and the model are generally good.

Chapter 6

Nonlinear Identification of Two Modes

In this chapter, we attempt to estimate the linear and nonlinear parameters of the first and second modes of a two-mass structure. The essential concept of this chapter involves exploiting a combination resonance of the additive type to uncover the nature of the linear and nonlinear coupling parameters between the first and second modes because this nonlinear resonance is believed to emphasize this coupling. We estimate the linear and cubic damping terms for each mode, the direct and parametric excitation terms for each mode, the linear damping coupling term between modes one and two, and the geometric and inertia quadratic and cubic terms involving modes one and two. We compare the estimated linear damping term of the first mode with the values obtained in Chapters 2 and 5. Additionally, we compare the estimated external and parametric excitation coefficients and the cubic damping term with those in Chapter 5. These comparisons serve as a check on the procedure outlined in this chapter.

6.1 Introduction

In Chapter 5, we estimated the linear and nonlinear parameters of the first mode of a two-mass structure. We exploited a nonlinear resonance that emphasizes these terms; namely, a combination of a principal parametric resonance and a sub-harmonic resonance of order one-half. We pursued an approximate solution via the method of multiple scales [57, 58, 60, 63, 65]. We estimated some of the parameters by comparing the observed harmonic content to that expected theoretically. Then, we estimated the remaining parameters by comparing the observed response of the first mode with that obtained from the frequency-response equation, which is obtained by manipulating the fixed points or equilibrium solutions of the corresponding modulation equations. Here, we extend these techniques to estimate the linear and nonlinear coefficients of two modes by exploiting a combination response of the additive type involving the first two modes of the same two-mass structure, see [60]

In Chapter 5, we found that the energy dissipation of the first mode is consistent with a combination of linear viscous damping and nonlinear cubic damping. Here, we suspect that the second mode exhibits the same damping mechanisms. Furthermore, both modes one and two are nearly orthogonal to the direction of the motion of the shaker. Hence, the frame is principally excited by a parametric (multiplicative) component and a small external (additive) component due to asymmetries. The curvature of the structure suggests that the analytical model should include quadratic and cubic geometric terms. Moreover, the concentrated masses lead to quadratic and cubic inertia nonlinearities. These terms can be found by formulating the equations of motion for this system. We show that this model satisfactorily describes observed moderate-amplitude motions.

In Chapter 3, we excited the structure at the sum of the frequencies of the first and second modes. This resulted in a moderate-amplitude motion of the first mode at its natural frequency and a moderate-amplitude motion of the second mode at its natural frequency, which we demonstrated in Figure 3.15. Each of the first three modes exhibited a response component at the excitation frequency. However, the third mode does not appear to have signification spectral content away from the excitation frequency. This suggests that the

third mode response is merely the linear superposition of its linear response to external excitations; that is, it does not exhibit a behavior that suggests a significant interaction with either mode one or mode two. Hence, we choose to model the structure's behavior as a combination resonance of the additive type involving modes one and two only.

If v_1 and v_2 denote the generalized coordinates in terms of the modal displacements for the first and second modes, then we assume that they are governed by the following mass-normalized nonlinear second-order ordinary-differential equations:

$$\begin{aligned}
\ddot{v}_1 + \omega_1^2 v_1 &+ 2\mu_{11}\dot{v}_1 + \mu_{12}\dot{v}_2 + \mu_{13}\dot{v}_1^3 + \left(\alpha_{21}v_1^2 + 2\alpha_{22}v_1v_2 + \alpha_{23}v_2^2\right) \\
&+ \left(\delta_{21}\dot{v}_1^2 + 2\delta_{21}v_1\ddot{v}_1 + 2\delta_{22}\dot{v}_1\dot{v}_2 + 2\delta_{22}\ddot{v}_1v_2 - \delta_{23}\dot{v}_2^2\right) \\
&+ \left(\alpha_{31}v_1^3 + 3\alpha_{32}v_1^2v_2 + \alpha_{33}v_1v_2^2 + \alpha_{34}v_2^3\right) \\
&+ \left(\delta_{31}v_1\dot{v}_1^2 + \delta_{31}v_1^2\ddot{v}_1 + \delta_{32}\dot{v}_1^2v_2 + 2\delta_{32}v_1\ddot{v}_1v_2 + 2\delta_{32}v_1\dot{v}_1\dot{v}_2\right. \\
&\quad \left. + 2\delta_{33}\dot{v}_1v_2\dot{v}_2 + \delta_{33}\ddot{v}_1v_2^2 - \delta_{34}v_1\dot{v}_2^2 - \delta_{35}v_2\dot{v}_2^2\right) \\
&= \eta_{11}F\cos(\Omega t) + \eta_{12}v_1F\cos(\Omega t) \qquad (6.1) \\
\ddot{v}_2 + \omega_2^2 v_2 &+ 2\mu_{22}\dot{v}_2 + \mu_{21}\dot{v}_1 + \mu_{23}\dot{v}_2^3 + \left(\alpha_{22}v_1^2 + 2\alpha_{23}v_1v_2 + \alpha_{24}v_2^2\right) \\
&+ \left(-\delta_{22}\dot{v}_1^2 + 2\delta_{23}\dot{v}_1\dot{v}_2 + 2\delta_{23}v_1\ddot{v}_2 + \delta_{24}\dot{v}_2^2 + 2\delta_{24}v_2\ddot{v}_2\right) \\
&+ \left(\alpha_{32}v_1^3 + \alpha_{33}v_1^2v_2 + 3\alpha_{34}v_1v_2^2 + \alpha_{35}v_2^3\right) \\
&+ \left(-\delta_{32}v_1\dot{v}_1^2 - \delta_{33}\dot{v}_1^2v_2 + 2\delta_{34}v_1\dot{v}_1\dot{v}_2 + \delta_{34}v_1^2\ddot{v}_2\right. \\
&\quad \left. + \delta_{35}v_1\dot{v}_2^2 + 2\delta_{35}\dot{v}_1v_2\dot{v}_2 + 2\delta_{35}v_1v_2\ddot{v}_2 + \delta_{36}v_2\dot{v}_2^2 + \delta_{36}v_2^2\ddot{v}_2\right) \\
&= \eta_{21}F\cos(\Omega t) + \eta_{22}v_2F\cos(\Omega t) \qquad (6.2)
\end{aligned}$$

where ω_1 is the linear natural frequency of the first mode; ω_2 is the natural frequency of the second mode; $2\mu_{11}$ is the first-mode linear damping coefficient; $2\mu_{22}$ is the second-mode linear damping coefficient; μ_{12} and $\mu_{21}(=\mu_{12})$ are linear damping coupling coefficients; μ_{13} and μ_{23} are cubic damping coefficients; $\alpha_{21}, \alpha_{22}, \alpha_{23}$, and α_{24} are the coefficients of the quadratic geometric nonlinearities; $\delta_{21}, \delta_{22}, \delta_{23}$, and δ_{24} are the coefficients of the quadratic inertia nonlinearities; $\alpha_{31}, \alpha_{32}, \alpha_{33}, \alpha_{34}$, and α_{35} are the coefficients of the cubic geometric nonlinearities; $\delta_{31}, \delta_{32}, \delta_{33}, \delta_{34}, \delta_{35}$, and δ_{36} are the coefficients of the cubic inertia nonlinearities; $F\cos(\Omega t)$ is the excitation; $\eta_{11}F\cos(\Omega t)$ and $\eta_{21}F\cos(\Omega t)$ are the external (additive) components of the

excitation; and $\eta_{12}v_1F\cos(\Omega t)$ and $\eta_{22}v_2F\cos(\Omega t)$ are the parametric (multiplicative) components of the excitation. Here, ω_1, ω_2, μ_{11}, μ_{22}, μ_{12}, μ_{21}, α_{21}, α_{22}, α_{23}, α_{24}, δ_{21}, δ_{22}, δ_{23}, δ_{24}, α_{31}, α_{32}, $\alpha_{33}, \alpha_{34}, \alpha_{35}$, δ_{31}, δ_{32}, δ_{33}, δ_{34}, δ_{35}, δ_{36}, η_{11}, η_{12}, η_{21}, and η_{22} are assumed to be constants.

There are a number of symmetries in Equations (6.1) and (6.2), which, in the absence of damping, are derivable from a Lagrangian or Hamiltonian formulation of the problem. If we had not specified v_1 and v_2 to be the mass-normalized modal displacements in the normal mode sense, these symmetries would still be present, but in a less obvious form. The transformation from a set of physical coordinates to the mass-normalized modal displacement requires significant initial effort. However, it greatly simplifies the description of, and improves our ability to interpret, the dynamics of the system.

We use the method of multiple scales [57, 58, 60, 63, 65] to generate a second-order approximate solution of Equations (6.1) and (6.2) when $\Omega \approx \omega_1+\omega_2$. We use this approximate solution to construct the modulation equations, which provide the first modal amplitude a_1, the second modal amplitude a_2, and the so-called *phase difference* parameter γ. They are formally defined in Section 6.2 as functions of the system parameters ω_1, ω_2, $2\mu_{11}$, $2\mu_{22}$, μ_{12}, μ_{21}, μ_{13}, μ_{23}, $\alpha_{21}, \alpha_{22}, \alpha_{23}$, α_{24}, $\delta_{21}, \delta_{22}, \delta_{23}$, δ_{24}, $\alpha_{31}, \alpha_{32}, \alpha_{33}, \alpha_{34}$, α_{35}, $\delta_{31}, \delta_{32}, \delta_{33}, \delta_{34}, \delta_{35}$, and δ_{36} and the excitation parameters η_{11}, η_{21} , η_{12}, η_{22} , Ω, and F. Then, we excite the structure and observe its response to a number of different levels of excitation and excitation frequencies. Finally, we attempt to estimate the parameters of the model from regressive fits between experimentally obtained and theoretically generated response relations.

6.2 Approximate Solution

To determine a solution for Equations (6.1) and (6.2) for weak nonlinearity, we introduce a small dimensionless parameter ϵ as a bookkeeping device and rewrite them as

$$\begin{aligned}
\ddot{v}_1 + \omega_1^2 v_1 &+2\epsilon^2\mu_{11}\dot{v}_1 + \epsilon\mu_{12}\dot{v}_2 + \epsilon^2\mu_{13}\dot{v}_1^3 + \epsilon\left(\alpha_{21}v_1^2 + 2\alpha_{22}v_1v_2 + \alpha_{23}v_2^2\right)\\
&+\epsilon\left(\delta_{21}\dot{v}_1^2 + 2\delta_{21}v_1\ddot{v}_1 + 2\delta_{22}\dot{v}_1\dot{v}_2 + 2\delta_{22}\ddot{v}_1v_2 - \delta_{23}\dot{v}_2^2\right)\\
&+\epsilon^2\left(\alpha_{31}v_1^3 + 3\alpha_{32}v_1^2v_2 + \alpha_{33}v_1v_2^2 + \alpha_{34}v_2^3\right)\\
&+\epsilon^2\left(\delta_{31}v_1\dot{v}_1^2 + \delta_{31}v_1^2\ddot{v}_1 + \delta_{32}\dot{v}_1^2v_2 + 2\delta_{32}v_1\ddot{v}_1v_2 + 2\delta_{32}v_1\dot{v}_1\dot{v}_2\right.\\
&\quad\left.+2\delta_{33}\dot{v}_1v_2\dot{v}_2 + \delta_{33}\ddot{v}_1v_2^2 - \delta_{34}v_1\dot{v}_2^2 - \delta_{35}v_2\dot{v}_2^2\right)\\
&= \epsilon\eta_{11}F\cos(\Omega t) + \epsilon\eta_{12}v_1F\cos(\Omega t) \qquad (6.3)\\
\ddot{v}_2 + \omega_2^2 v_2 &+2\epsilon^2\mu_{22}\dot{v}_2 + \epsilon\mu_{21}\dot{v}_1 + \epsilon^2\mu_{23}\dot{v}_2^3 + \epsilon\left(\alpha_{22}v_1^2 + 2\alpha_{23}v_1v_2 + \alpha_{24}v_2^2\right)\\
&+\epsilon\left(-\delta_{22}\dot{v}_1^2 + 2\delta_{23}\dot{v}_1\dot{v}_2 + 2\delta_{23}v_1\ddot{v}_2 + \delta_{24}\dot{v}_2^2 + 2\delta_{24}v_2\ddot{v}_2\right)\\
&+\epsilon^2\left(\alpha_{32}v_1^3 + \alpha_{33}v_1^2v_2 + 3\alpha_{34}v_1v_2^2 + \alpha_{35}v_2^3\right)\\
&+\epsilon^2\left(-\delta_{32}v_1\dot{v}_1^2 - \delta_{33}\dot{v}_1^2v_2 + 2\delta_{34}v_1\dot{v}_1\dot{v}_2 + \delta_{34}v_1^2\ddot{v}_2\right.\\
&\quad\left.+\delta_{35}v_1\dot{v}_2^2 + 2\delta_{35}\dot{v}_1v_2\dot{v}_2 + 2\delta_{35}v_1v_2\ddot{v}_2 + \delta_{36}v_2\dot{v}_2^2 + \delta_{36}v_2^2\ddot{v}_2\right)\\
&= \epsilon\eta_{21}F\cos(\Omega t) + \epsilon\eta_{22}v_2F\cos(\Omega t) \qquad (6.4)
\end{aligned}$$

Using the method of multiple scale [57, 58, 60, 63, 65], we seek a uniform solution of Equations (6.3) and (6.4) in the form

$$v_1 = v_{11}(T_0, T_1, T_2) + \epsilon v_{12}(T_0, T_1, T_2) + \epsilon^2 v_{13}(T_0, T_1, T_2) + O(\epsilon^3) \qquad (6.5)$$

$$v_2 = v_{21}(T_0, T_1, T_2) + \epsilon v_{22}(T_0, T_1, T_2) + \epsilon^2 v_{23}(T_0, T_1, T_2) + O(\epsilon^3) \qquad (6.6)$$

where $T_0 = t$ is a fast time scale and $T_1 = \epsilon t$ and $T_2 = \epsilon^2 t$ are slow time scales. In terms of T_0, T_1, and T_2, the time derivatives become

$$\frac{d}{dt} = D_0 + \epsilon D_1 + \epsilon^2 D_2 + O(\epsilon^3) \qquad (6.7)$$

$$\frac{d^2}{dt^2} = D_0^2 + 2\epsilon D_0D_1 + \epsilon^2 D_1^2 + 2\epsilon^2 D_0D_2 + O(\epsilon^3) \qquad (6.8)$$

where $D_n = \partial/\partial T_n$. To describe quantitatively the closeness of Ω to $\omega_1 + \omega_2$, we introduce a detuning parameter σ defined by

$$\Omega = \omega_1 + \omega_2 + \epsilon^2\sigma \tag{6.9}$$

Substituting Equations (6.7)-(6.9) into Equations (6.3) and (6.4) and equating coefficients of like powers of ϵ, we have

Order ϵ^0

$$D_0^2 v_{11} + \omega_1^2 v_{11} = 0 \tag{6.10}$$

$$D_0^2 v_{21} + \omega_2^2 v_{21} = 0 \tag{6.11}$$

Order ϵ^1

$$\begin{aligned} D_0^2 v_{12} + \omega_1^2 v_{12} = & -2D_0 D_1 v_{11} - \mu_{12} D_0 v_{21} \\ & -\alpha_{21} v_{11}^2 - 2\alpha_{22} v_{11} v_{21} - \alpha_{23} v_{21}^2 - \delta_{21}(D_0 v_{11})^2 - 2\delta_{21} v_{11} D_0^2 v_{11} \\ & -2\delta_{22} D_0 v_{11} D_0 v_{21} - 2\delta_{22} D_0^2 v_{11} v_{21} + \delta_{23}(D_0 v_{21})^2 \\ & +\eta_{11} F\cos(\Omega T_0) + \eta_{12} v_{11} F\cos(\Omega T_0) \end{aligned} \tag{6.12}$$

$$\begin{aligned} D_0^2 v_{22} + \omega_2^2 v_{22} = & -2D_0 D_1 v_{21} - \mu_{21} D_0 v_{11} \\ & -\alpha_{22} v_{11}^2 - 2\alpha_{23} v_{11} v_{21} - \alpha_{24} v_{21}^2 + \delta_{22}(D_0 v_{11})^2 \\ & -2\delta_{23} D_0 v_{11} D_0 v_{21} - 2\delta_{23} v_{11} D_0^2 v_{21} - \delta_{24}(D_0 v_{21})^2 - 2\delta_{24} v_{21} D_0^2 v_{21} \\ & +\eta_{21} F\cos(\Omega T_0) + \eta_{22} v_{21} F\cos(\Omega T_0) \end{aligned} \tag{6.13}$$

Order ϵ^2

$$
\begin{aligned}
D_0^2 v_{13} + \omega_1^2 v_{13} = & -2D_0D_1v_{12} - 2D_0D_2v_{11} - D_1^2v_{11} - 2\mu_{11}D_0v_{11} \\
& -\mu_{12}\left(D_1v_{21} + D_0v_{22}\right) - \mu_{13}(D_0v_{11})^3 \\
& -2\left(\alpha_{21}v_{11}v_{12} + \alpha_{22}v_{12}v_{21} + \alpha_{22}v_{11}v_{22} + \alpha_{23}v_{21}v_{22}\right) \\
& -2\left[\delta_{21}(D_0v_{11})(D_0v_{12}) + \delta_{21}v_{12}(D_0^2v_{11}) + \delta_{21}v_{11}(D_0^2v_{12})\right. \\
& \quad +2\delta_{21}v_{11}(D_0D_1v_{11}) + \delta_{21}(D_0v_{11})(D_1v_{11}) + \delta_{22}(D_0v_{12})(D_0v_{21}) \\
& \quad +\delta_{22}(D_0v_{11})(D_0v_{22}) + \delta_{22}(D_0^2v_{12})v_{21} + \delta_{22}(D_0v_{11})(D_1v_{21}) \\
& \quad +\delta_{22}(D_0v_{21})(D_1v_{11}) + 2\delta_{22}v_{21}(D_0D_1v_{11}) + \delta_{22}(D_0^2v_{11})v_{22} \\
& \quad \left.-\delta_{23}(D_0v_{21})(D_0v_{22}) - \delta_{23}(D_0v_{21})(D_1v_{21})\right] \\
& -\alpha_{31}v_{11}^3 - 3\alpha_{32}v_{11}^2v_{21} - \alpha_{33}v_{11}v_{21}^2 - \alpha_{34}v_{21}^3 \\
& -\delta_{31}v_{11}(D_0v_{11})^2 - \delta_{31}v_{11}^2(D_0^2v_{11}) - \delta_{32}(D_0v_{11})^2v_{21} \\
& -2\delta_{32}v_{11}(D_0^2v_{11})v_{21} - 2\delta_{32}v_{11}(D_0v_{11})(D_0v_{21}) - 2\delta_{33}(D_0v_{11})v_{21}(D_0v_{21}) \\
& -\delta_{33}(D_0^2v_{11})v_{21}^2 + \delta_{34}v_{11}(D_0v_{21})^2 + \delta_{35}v_{21}(D_0v_{21})^2 \\
& +\eta_{12}v_{12}F\cos\left(\Omega T_0\right)
\end{aligned}
\tag{6.14}
$$

$$
\begin{aligned}
D_0^2 v_{23} + \omega_2^2 v_{23} = & -2D_0D_1v_{22} - 2D_0D_2v_{21} - D_1^2v_{21} - 2\mu_{22}D_0v_{21} \\
& -\mu_{21}\left(D_1v_{11} + D_0v_{12}\right) - \mu_{23}\left(D_0v_{21}\right)^3 \\
& -2\left(\alpha_{22}v_{11}v_{12} + \alpha_{23}v_{12}v_{21} + \alpha_{23}v_{11}v_{22} + \alpha_{24}v_{21}v_{22}\right) \\
& -2\left[-\delta_{22}(D_0v_{11})(D_0v_{12}) - \delta_{22}(D_0v_{11})(D_1v_{11}) + \delta_{23}(D_0v_{12})(D_0v_{21})\right. \\
& \quad +\delta_{23}(D_0v_{11})(D_0v_{22}) + \delta_{23}v_{12}(D_0^2v_{21}) + \delta_{23}(D_0v_{21})(D_1v_{11}) \\
& \quad +\delta_{23}(D_0v_{11})(D_1v_{21}) + 2\delta_{23}v_{11}(D_0D_1v_{21}) + \delta_{23}v_{11}(D_0^2v_{22}) \\
& \quad +\delta_{24}(D_0v_{21})(D_0v_{22}) + \delta_{24}v_{22}(D_0^2v_{21}) + \delta_{24}v_{21}(D_0^2v_{22}) \\
& \quad \left.+2\delta_{24}v_{21}(D_0D_1v_{21}) + \delta_{24}(D_0v_{21})(D_1v_{21})\right] \\
& -\alpha_{32}v_{11}^3 - \alpha_{33}v_{11}^2v_{21} - 3\alpha_{34}v_{11}v_{21}^2 - \alpha_{35}v_{21}^3 \\
& +\delta_{32}v_{11}(D_0v_{11})^2 + \delta_{33}(D_0v_{11})^2v_{21} - 2\delta_{34}v_{11}(D_0v_{11})(D_0v_{21}) \\
& -\delta_{34}v_{11}^2(D_0^2v_{21}) - \delta_{35}v_{11}(D_0v_{21})^2 - 2\delta_{35}(D_0v_{11})v_{21}(D_0v_{21}) \\
& -2\delta_{35}v_{11}v_{21}(D_0^2v_{21}) - \delta_{36}v_{21}(D_0v_{21})^2 - \delta_{36}v_{21}^2(D_0^2v_{21}) \\
& +\eta_{22}v_{22}F\cos\left(\Omega T_0\right)
\end{aligned}
\tag{6.15}
$$

It follows from Equations (6.10) and (6.11) that

$$v_{11} = A_1(T_1, T_2)e^{i\omega_1 T_0} + cc \tag{6.16}$$

$$v_{21} = A_2(T_1, T_2)e^{i\omega_2 T_0} + cc \tag{6.17}$$

where cc denotes the complex conjugate of the preceding terms. The functions $A_1(T_1, T_2)$ and $A_2(T_1, T_2)$ are unknown at this level of approximation; they will be determined by eliminating the secular terms from v_{12}, v_{22}, v_{13}, and v_{23}.

Substituting Equations (6.16) and (6.17) into Equations (6.12) and (6.13), we have

$$\begin{aligned}
D_0^2 v_{12} + \omega_1^2 v_{12} = & -2i\omega_1 D_1 A_1 e^{i\omega_1 T_0} - i\omega_2 \mu_{12} A_2 e^{i\omega_2 T_0} \\
& -(\alpha_{21} - 3\omega_1^2 \delta_{21}) A_1^2 e^{i2\omega_1 T_0} - (\alpha_{21} - \omega_1^2 \delta_{21}) A_1 \bar{A}_1 \\
& -2(\alpha_{22} - \omega_1 \omega_2 \delta_{22} - \omega_1^2 \delta_{22}) A_1 A_2 e^{i(\omega_1 + \omega_2) T_0} \\
& -2(\alpha_{22} + \omega_1 \omega_2 \delta_{22} - \omega_1^2 \delta_{22}) A_1 \bar{A}_2 e^{i(\omega_1 - \omega_2) T_0} \\
& -(\alpha_{23} + \omega_2^2 \delta_{23}) A_2^2 e^{i2\omega_2 T_0} - (\alpha_{23} - \omega_2^2 \delta_{23}) A_2 \bar{A}_2 \\
& + \frac{1}{2} \eta_{11} F e^{i\Omega T_0} + \frac{1}{2} \eta_{12} A_1 F e^{i(\Omega + \omega_1) T_0} \\
& + \frac{1}{2} \eta_{12} \bar{A}_1 F e^{i(\Omega - \omega_1) T_0} + cc
\end{aligned} \tag{6.18}$$

$$\begin{aligned}
D_0^2 v_{22} + \omega_2^2 v_{22} = & -2i\omega_2 D_1 A_2 e^{i\omega_2 T_0} - i\omega_1 \mu_{21} A_1 e^{i\omega_1 T_0} \\
& -(\alpha_{22} + \omega_1^2 \delta_{22}) A_1^2 e^{i2\omega_1 T_0} - (\alpha_{22} - \omega_1^2 \delta_{22}) A_1 \bar{A}_1 \\
& -2(\alpha_{23} - \omega_1 \omega_2 \delta_{23} - \omega_2^2 \delta_{23}) A_1 A_2 e^{i(\omega_1 + \omega_2) T_0} \\
& -2(\alpha_{23} + \omega_1 \omega_2 \delta_{23} - \omega_2^2 \delta_{23}) \bar{A}_1 A_2 e^{i(\omega_2 - \omega_1) T_0} \\
& -(\alpha_{24} - 3\omega_2^2 \delta_{24}) A_2^2 e^{i2\omega_2 T_0} - (\alpha_{24} - \omega_2^2 \delta_{24}) A_2 \bar{A}_2 \\
& + \frac{1}{2} \eta_{21} F e^{i\Omega T_0} + \frac{1}{2} \eta_{22} A_2 F e^{i(\Omega + \omega_2 T_0} \\
& + \frac{1}{2} \eta_{22} \bar{A}_2 F e^{i(\Omega - \omega_2) T_0} + cc
\end{aligned} \tag{6.19}$$

Eliminating the terms that would otherwise produce secular terms provides

$$D_1 A_1 = D_1 A_2 = 0 \tag{6.20}$$

which imply that A_1 and A_2 are independent of T_1. Then, the solution of Equations (6.18)

and (6.19) can be expressed as

$$
\begin{aligned}
v_{12} = & -\frac{i\omega_2\mu_{12}A_2}{\omega_1^2-\omega_2^2}e^{i\omega_2 T_0} \\
& -\frac{(\alpha_{21}-\omega_1^2\delta_{21})A_1\bar{A}_1+(\alpha_{23}-\omega_2^2\delta_{23})A_2\bar{A}_2}{\omega_1^2}+\frac{(\alpha_{21}-3\omega_1^2\delta_{21})A_1^2}{3\omega_1^2}e^{i2\omega_1 T_0} \\
& +\frac{2(\alpha_{22}+\omega_1\omega_2\delta_{22}-\omega_1^2\delta_{22})A_1\bar{A}_2}{\omega_2^2-2\omega_1\omega_2}e^{i(\omega_1-\omega_2)T_0} \\
& +\frac{2(\alpha_{22}-\omega_1\omega_2\delta_{22}-\omega_1^2\delta_{22})A_1A_2}{\omega_2^2+2\omega_1\omega_2}e^{i(\omega_1+\omega_2)T_0} \\
& -\frac{(\alpha_{23}+\omega_2^2\delta_{23})A_2^2}{\omega_1^2-4\omega_2^2}e^{i2\omega_2 T_0} \\
& +\frac{\eta_{11}F}{2(\omega_1^2-\Omega^2)}e^{i\Omega T_0}+\frac{\eta_{12}\bar{A}_1F}{2(2\omega_1\Omega-\Omega^2)}e^{i(\Omega-\omega_1)T_0} \\
& -\frac{\eta_{12}A_1F}{2(\Omega^2+2\omega_1\Omega)}e^{i(\Omega+\omega_1)T_0}+cc
\end{aligned}
\tag{6.21}
$$

$$
\begin{aligned}
v_{22} = & -\frac{i\omega_1\mu_{21}A_1}{\omega_2^2-\omega_1^2}e^{i\omega_1 T_0} \\
& -\frac{(\alpha_{22}-\omega_1^2\delta_{22})A_1\bar{A}_1+(\alpha_{24}-\omega_2^2\delta_{24})A_2\bar{A}_2}{\omega_2^2}-\frac{(\alpha_{22}+\omega_1^2\delta_{22})A_1^2}{\omega_2^2-4\omega_1^2}e^{i2\omega_1 T_0} \\
& +\frac{2(\alpha_{23}+\omega_1\omega_2\delta_{23}-\omega_2^2\delta_{23})\bar{A}_1A_2}{\omega_1^2-2\omega_1\omega_2}e^{i(\omega_2-\omega_1)T_0} \\
& +\frac{2(\alpha_{23}-\omega_1\omega_2\delta_{23}-\omega_2^2\delta_{23})A_1A_2}{\omega_1^2+2\omega_1\omega_2}e^{i(\omega_1+\omega_2)T_0} \\
& +\frac{(\alpha_{24}-3\omega_2^2\delta_{24})A_2^2}{3\omega_2^2}e^{i2\omega_2 T_0} \\
& +\frac{\eta_{21}F}{2(\omega_2^2-\Omega^2)}e^{i\Omega T_0}+\frac{\eta_{22}\bar{A}_2F}{2(2\omega_2\Omega-\Omega^2)}e^{i(\Omega-\omega_2)T_0} \\
& -\frac{\eta_{22}A_2F}{2(\Omega^2+2\omega_2\Omega)}e^{i(\Omega+\omega_2)T_0}+cc
\end{aligned}
\tag{6.22}
$$

where use has been made of the fact that $\Omega \approx \omega_1 + \omega_2$.

Substituting Equations (6.16),(6.17),(6.21), and (6.22) into Equations (6.14) and (6.15)

yields

$$
\begin{aligned}
D_0^2 v_{13} + \omega_1^2 v_{13} = & -2i\omega_1 D_2 A_1 e^{i\omega_1 T_0} - 2i\omega_1 \mu_{11} A_1 e^{i\omega_1 T_0} \\
& -3i\omega_1^3 \mu_{13} A_1^2 \bar{A}_1 e^{i\omega_1 T_0} - \frac{\omega_1^2 \mu_{12}\mu_{21} A_1}{\omega_2^2 - \omega_1^2} e^{i\omega_1 T_0} \\
& - \left[3\alpha_{31} - 2\omega_1^2 \delta_{31} - \frac{10\alpha_{21}^2}{3\omega_1^2} + 4\alpha_{21}\delta_{21} + 2\omega_1^2 \delta_{21}^2 \right. \\
& \quad - \frac{2(3\omega_2^2 - 8\omega_1^2)\alpha_{22}^2}{\omega_2^2(\omega_2^2 - 4\omega_1^2)} + \frac{4\omega_1^2(\omega_2^2 - 8\omega_1^2)\alpha_{22}\delta_{22}}{\omega_2^2(\omega_2^2 - 4\omega_1^2)} \\
& \quad \left. - \frac{8\omega_1^4(\omega_2^2 - 2\omega_1^2)\delta_{22}^2}{\omega_2^2(\omega_2^2 - 4\omega_1^2)} \right] A_1^2 \bar{A}_1 e^{i\omega_1 T_0} \\
& - \left[2\alpha_{33} - 2\omega_1^2 \delta_{33} - 2\omega_2^2 \delta_{34} - \frac{4\alpha_{21}\alpha_{23}}{\omega_1^2} + 4\alpha_{23}\delta_{21} \right. \\
& \quad + \frac{4\omega_2^2 \alpha_{21}\delta_{23}}{\omega_1^2} - 4\omega_2^2 \delta_{21}\delta_{23} + \frac{8(\alpha_{22}^2 + 2\omega_1^2 \alpha_{22}\delta_{22} + \omega_1^2\omega_2^2\delta_{22}^2 - 3\omega_1^4 \delta_{22}^2)}{\omega_2^2 - 4\omega_1^2} \\
& \quad - \frac{4\alpha_{22}\alpha_{24}}{\omega_2^2} - 4\omega_1^2 \delta_{22}\delta_{24} + \frac{4\alpha_{24}\delta_{22}}{\omega_2^2} + 4\alpha_{22}\delta_{24} \\
& \quad \left. + \frac{8(\alpha_{23}^2 + 2\omega_2^2 \alpha_{23}\delta_{23} + \omega_1^2\omega_2^2\delta_{23}^2 - 3\omega_2^4 \delta_{23}^2)}{\omega_1^2 - 4\omega_2^2} \right] A_1 A_2 \bar{A}_2 e^{i\omega_1 T_0} \\
& - \frac{\eta_{12}^2 A_1 F^2}{2(\Omega^2 - 4\omega_1^2)} e^{i\omega_1 T_0} \\
& - \left[\frac{(\alpha_{22} - \Omega^2\delta_{22} + \omega_2\Omega\delta_{22})\eta_{11}}{\omega_1^2 - \Omega^2} + \frac{(\alpha_{23} - \omega_2\Omega\delta_{23})\eta_{21}}{\omega_2^2 - \Omega^2} \right] \bar{A}_2 F e^{i(\Omega - \omega_2)T_0} \\
& - i \left[\frac{(\Omega - \omega_2)\mu_{12}\eta_{22}}{2\Omega(2\omega_2 - \Omega)} - \frac{\omega_2 \mu_{12}\eta_{12}}{2(\omega_1^2 - \omega_2^2)} \right] \bar{A}_2 F e^{i(\Omega - \omega_2)T_0} + cc + NST \qquad (6.23)
\end{aligned}
$$

and

$$
\begin{aligned}
D_0^2 v_{23} + \omega_2^2 v_{23} = & -2i\omega_2 D_2 A_2 e^{i\omega_2 T_0} - 2i\omega_2 \mu_{22} A_2 e^{i\omega_2 T_0} \\
& -3i\omega_2^3 \mu_{23} A_2^2 \bar{A}_2 e^{i\omega_2 T_0} - \frac{\omega_2^2 \mu_{21}\mu_{12} A_2}{\omega_1^2 - \omega_2^2} e^{i\omega_2 T_0} \\
& - \Bigg[3\alpha_{35} - 2\omega_2^2 \delta_{36} - \frac{10\alpha_{24}^2}{3\omega_2^2} + 4\alpha_{24}\delta_{24} + 2\omega_2^2 \delta_{24}^2 \\
& \quad - \frac{2(3\omega_1^2 - 8\omega_2^2)\alpha_{23}^2}{\omega_1^2(\omega_1^2 - 4\omega_2^2)} + \frac{4\omega_2^2(\omega_1^2 - 8\omega_2^2)\alpha_{23}\delta_{23}}{\omega_1^2(\omega_1^2 - 4\omega_2^2)} \\
& \quad - \frac{8\omega_2^4(\omega_1^2 - 2\omega_2^2)\delta_{23}^2}{\omega_1^2(\omega_1^2 - 4\omega_2^2)} \Bigg] A_2^2 \bar{A}_2 exp(i\omega_2 T_0) \\
& - \Bigg[2\alpha_{33} - 2\omega_1^2 \delta_{33} - 2\omega_2^2 \delta_{34} - \frac{4\alpha_{22}\alpha_{24}}{\omega_2^2} + 4\alpha_{22}\delta_{24} \\
& \quad + \frac{4\omega_1^2 \alpha_{24}\delta_{22}}{\omega_2^2} - 4\omega_1^2 \delta_{22}\delta_{24} + \frac{8(\alpha_{23}^2 + 2\omega_2^2\alpha_{23}\delta_{23} + \omega_1^2\omega_2^2\delta_{23}^2 - 3\omega_2^4\delta_{23}^2)}{\omega_1^2 - 4\omega_2^2} \\
& \quad - \frac{4\alpha_{21}\alpha_{23}}{\omega_1^2} - 4\omega_2^2\delta_{21}\delta_{23} + \frac{4\omega_2^2\alpha_{21}\delta_{23}}{\omega_1^2} + 4\alpha_{23}\delta_{21} \\
& \quad + \frac{8(\alpha_{22}^2 + 2\omega_1^2\alpha_{22}\delta_{22} + \omega_1^2\omega_2^2\delta_{22}^2 - 3\omega_1^4\delta_{22}^2)}{\omega_2^2 - 4\omega_1^2} \Bigg] A_1 \bar{A}_1 A_2 exp(i\omega_2 T_0) \\
& - \frac{\eta_{22}^2 A_2 F^2}{2(\Omega^2 - 4\omega_2^2)} e^{i\omega_2 T_0} \\
& - \left[\frac{(\alpha_{22} - \omega_1\Omega\delta_{22})\eta_{11}}{\omega_1^2 - \Omega^2} + \frac{(\alpha_{23} - \Omega^2\delta_{23} + \omega_1\Omega\delta_{23})\eta_{21}}{\omega_2^2 - \Omega^2} \right] \bar{A}_1 F e^{i(\Omega - \omega_1 T_0)} \\
& - i \left[\frac{(\Omega - \omega_1)\mu_{21}\eta_{12}}{2\Omega(2\omega_1 - \Omega)} - \frac{\omega_1 \mu_{21}\eta_{22}}{2(\omega_2^2 - \omega_1^2)} \right] \bar{A}_1 F e^{i(\Omega - \omega_1)T_0} + cc + NST
\end{aligned} \tag{6.24}
$$

where NST denotes terms that do not produce secular terms. Using Equation (6.9) and eliminating the terms that produce secular terms from Equations (6.23) and (6.24), we obtain

$$
\begin{aligned}
2i\omega_1 (A_1' + \mu_{11} A_1) & + 3i\omega_1^3 \mu_{13} A_1^2 \bar{A}_1 + 2\Gamma_1 A_1 + 8\Gamma_2 A_1^2 \bar{A}_1 + 8\Gamma_3 A_1 A_2 \bar{A}_2 \\
& + 2\Gamma_4 A_1 F^2 + 2\Gamma_5 \bar{A}_2 F e^{i\sigma T_2} + 2i\Gamma_6 \bar{A}_2 F e^{i\sigma T_2} = 0
\end{aligned} \tag{6.25}
$$

$$
\begin{aligned}
2i\omega_2 (A_2' + \mu_{22} A_2) & + 3i\omega_2^2 \mu_{23} A_2 \bar{A}_2 + 2\Gamma_7 A_2 + 8\Gamma_8 A_2^2 \bar{A}_2 + 8\Gamma_9 A_1 \bar{A}_1 A_2 \\
& + 2\Gamma_{10} A_2 F^2 + 2\Gamma_{11} \bar{A}_1 F e^{i\sigma T_2} + 2i\Gamma_{12} \bar{A}_1 F e^{i\sigma T_2} = 0
\end{aligned} \tag{6.26}
$$

where the prime denotes differentiation with respect to T_2 and

$$
\begin{aligned}
2\Gamma_1 &= \frac{\omega_1^2\mu_{12}\mu_{21}}{\omega_2^2-\omega_1^2}\\
8\Gamma_2 &= 3\alpha_{31}-2\omega_1^2\delta_{31}-\frac{10\alpha_{21}^2}{3\omega_1^2}+4\alpha_{21}\delta_{21}+2\omega_1^2\delta_{21}^2\\
&\quad -\frac{2(3\omega_2^2-8\omega_1^2)\alpha_{22}^2}{\omega_2^2(\omega_2^2-4\omega_1^2)}+\frac{4\omega_1^2(\omega_2^2-8\omega_1^2)\alpha_{22}\delta_{22}}{\omega_2^2(\omega_2^2-4\omega_1^2)}-\frac{8\omega_1^4(\omega_2^2-2\omega_1^2)\delta_{22}^2}{\omega_2^2(\omega_2^2-4\omega_1^2)}\\
8\Gamma_3 &= 2\alpha_{33}-2\omega_1^2\delta_{33}-2\omega_2^2\delta_{34}-\frac{4\alpha_{21}\alpha_{23}}{\omega_1^2}+4\alpha_{23}\delta_{21}+\frac{4\omega_2^2\alpha_{21}\delta_{23}}{\omega_1^2}-4\omega_2^2\delta_{21}\delta_{23}\\
&\quad +\frac{8(\alpha_{22}^2+2\omega_1^2\alpha_{22}\delta_{22}+\omega_1^2\omega_2^2\delta_{22}^2-3\omega_1^4\delta_{22}^2)}{\omega_2^2-4\omega_1^2}-\frac{4\alpha_{22}\alpha_{24}}{\omega_2^2}-4\omega_1^2\delta_{22}\delta_{24}\\
&\quad +\frac{4\omega_1^2\alpha_{24}\delta_{22}}{\omega_2^2}+4\alpha_{22}\delta_{24}+\frac{8(\alpha_{23}^2+2\omega_2^2\alpha_{23}\delta_{23}+\omega_1^2\omega_2^2\delta_{23}^2-3\omega_2^4\delta_{23}^2)}{\omega_1^2-4\omega_2^2}\\
2\Gamma_4 &= \frac{\eta_{12}^2}{2(\Omega^2-4\omega_1^2)}\\
2\Gamma_5 &= \frac{(\alpha_{22}-\Omega^2\delta_{22}+\omega_2\Omega\delta_{22})\eta_{11}}{\omega_1^2-\Omega^2}+\frac{(\alpha_{23}-\omega_2\Omega\delta_{23})\eta_{21}}{\omega_2^2-\Omega^2}\\
2\Gamma_6 &= \frac{(\Omega-\omega_2)\mu_{12}\eta_{22}}{2\Omega(2\omega_2-\Omega)}-\frac{\omega_2\mu_{12}\eta_{12}}{2(\omega_1^2-\omega_2^2)}\\
2\Gamma_7 &= \frac{\omega_2^2\mu_{21}\mu_{12}}{\omega_1^2-\omega_2^2}\\
8\Gamma_8 &= 3\alpha_{35}-2\omega_2^2\delta_{36}-\frac{10\alpha_{24}^2}{3\omega_2^2}+4\alpha_{24}\delta_{24}+2\omega_2^2\delta_{24}^2\\
&\quad -\frac{2(3\omega_1^2-8\omega_2^2)\alpha_{23}^2}{\omega_1^2(\omega_1^2-4\omega_2^2)}-\frac{4\omega_2^2(\omega_1^2-8\omega_2^2)\alpha_{23}\delta_{23}}{\omega_1^2(\omega_1^2-4\omega_2^2)}-\frac{8\omega_2^4(\omega_1^2-2\omega_2^2)\delta_{23}^2}{\omega_1^2(\omega_1^2-4\omega_2^2)}\\
8\Gamma_9 &= 2\alpha_{33}-2\omega_1^2\delta_{33}-2\omega_2^2\delta_{34}-\frac{4\alpha_{22}\alpha_{24}}{\omega_2^2}+4\alpha_{22}\delta_{24}+\frac{4\omega_1^2\alpha_{24}\delta_{22}}{\omega_2^2}-4\omega_1^2\delta_{22}\delta_{24}\\
&\quad +\frac{8(\alpha_{23}^2+2\omega_2^2\alpha_{23}\delta_{23}+\omega_1^2\omega_2^2\delta_{23}^2-3\omega_2^4\delta_{23}^2)}{\omega_1^2-4\omega_2^2}-\frac{4\alpha_{21}\alpha_{23}}{\omega_1^2}-4\omega_2^2\delta_{21}\delta_{23}\\
&\quad +\frac{4\omega_2^2\alpha_{21}\delta_{23}}{\omega_1^2}+4\alpha_{23}\delta_{21}+\frac{8(\alpha_{22}^2+2\omega_1^2\alpha_{22}\delta_{22}+\omega_1^2\omega_2^2\delta_{22}^2-3\omega_1^4\delta_{22}^2)}{\omega_2^2-4\omega_1^2}\\
2\Gamma_{10} &= \frac{\eta_{22}^2}{2(\Omega^2-4\omega_2^2)}\\
2\Gamma_{11} &= \frac{(\alpha_{22}-\omega_1\Omega\delta_{22})\eta_{11}}{\omega_1^2-\Omega^2}+\frac{(\alpha_{23}-\Omega^2\delta_{23}+\omega_1\Omega\delta_{23})\eta_{21}}{\omega_2^2-\Omega^2}\\
2\Gamma_{12} &= \frac{(\Omega-\omega_1)\mu_{21}\eta_{12}}{2\Omega(2\omega_1-\Omega)}-\frac{\omega_1\mu_{21}\eta_{22}}{2(\omega_2^2-\omega_1^2)}
\end{aligned}
\tag{6.27}
$$

However, we note that not all of the Γ_i are independent; for instance, $\omega_2^2\Gamma_1 = -\omega_1^2\Gamma_7$, $\Gamma_3 = \Gamma_9$, $\Gamma_5 \approx \Gamma_{11}$, and $\Gamma_6 \approx \Gamma_{12}$.

Next, we express A_1 and A_2 in polar form as

$$A_1 = \frac{1}{2}a_1 e^{i\beta_1} \tag{6.28}$$

$$A_2 = \frac{1}{2}a_2 e^{i\beta_2} \tag{6.29}$$

Substituting Equations (6.28) and (6.29) into Equations (6.25) and (6.26) and separating real and imaginary parts, we have

$$\omega_1 a_1' = -\omega_1\mu_{11}a_1 - \frac{3\omega_1^3\mu_{13}}{8}a_1^3 - (\Gamma_5\sin\gamma + \Gamma_6\cos\gamma)Fa_2 \tag{6.30}$$

$$\omega_1 a_1\beta_1' = \Gamma_1 a_1 + \Gamma_2 a_1^3 + \Gamma_3 a_1 a_2^2 + \Gamma_4 a_1 F^2 + (\Gamma_5\cos\gamma - \Gamma_6\sin\gamma)Fa_2 \tag{6.31}$$

$$\omega_2 a_2' = -\omega_2\mu_{22}a_2 - \frac{3\omega_2^3\mu_{23}}{8}a_2^3 - (\Gamma_{11}\sin\gamma + \Gamma_{12}\cos\gamma)Fa_1 \tag{6.32}$$

$$\omega_2 a_2\beta_2' = \Gamma_7 a_2 + \Gamma_8 a_2^3 + \Gamma_9 a_1^2 a_2 + \Gamma_{10} a_2 F^2 + (\Gamma_{11}\cos\gamma - \Gamma_{12}\sin\gamma)Fa_1 \tag{6.33}$$

We note that Equations (6.31) and (6.33) can be combined into

$$\begin{aligned}\omega_1\omega_2 a_1 a_2\gamma' = {} & \omega_1\omega_2 a_1 a_2\sigma + (\omega_2\Gamma_1 + \omega_1\Gamma_7)a_1 a_2 \\ & + (\omega_2\Gamma_2 + \omega_1\Gamma_9)a_1^3 a_2 + (\omega_2\Gamma_3 + \omega_1\Gamma_8)a_1 a_2^3 + (\omega_2\Gamma_4 + \omega_1\Gamma_{10})a_1 a_2 F^2 \\ & + \omega_2(\Gamma_5\cos\gamma - \Gamma_6\sin\gamma)Fa_2^2 + \omega_1(\Gamma_{11}\cos\gamma - \Gamma_{12}\sin\gamma)Fa_1^2\end{aligned} \tag{6.34}$$

where

$$\gamma = \sigma T_2 - \beta_1 - \beta_2 \tag{6.35}$$

Combining Equations (6.5), (6.6), (6.16), (6.17), (6.21), (6.22), (6.28), (6.29), and (6.35),

we obtain

$$
\begin{aligned}
v_1 = a_1 \cos(\omega_1 t + \beta_1) - \epsilon \Bigg\{ & \frac{(\alpha_{21} - \omega_1^2 \delta_{21}) a_1^2 + (\alpha_{23} - \omega_2^2 \delta_{23}) a_2^2}{2\omega_1^2} \\
& - \frac{\omega_2 \mu_{12} a_2}{\omega_1^2 - \omega_2^2} \sin(\omega_2 t + \beta_2) - \frac{\eta_{12} a_1 F}{2(2\omega_1 \Omega - \Omega^2)} \cos[(\Omega - \omega_1)t - \beta_1] \\
& - \frac{(\alpha_{21} - 3\omega_1^2 \delta_{21}) a_1^2}{6\omega_1^2} \cos(2\omega_1 t + 2\beta_1) + \frac{(\alpha_{23} + \omega_2^2 \delta_{23}) a_2^2}{2(\omega_1^2 - 4\omega_2^2)} \cos(2\omega_2 t + 2\beta_2) \\
& - \frac{(\alpha_{22} + \omega_1 \omega_2 \delta_{22} - \omega_1^2 \delta_{22}) a_1 a_2}{\omega_2^2 - 2\omega_1 \omega_2} \cos[(\omega_1 - \omega_2)t + \beta_1 - \beta_2] \\
& - \frac{(\alpha_{22} - \omega_1 \omega_2 \delta_{22} - \omega_1^2 \delta_{22}) a_1 a_2}{\omega_2^2 + 2\omega_1 \omega_2} \cos[(\omega_1 + \omega_2)t + \beta_1 + \beta_2] \\
& - \frac{\eta_{11} F}{\omega_1^2 - \Omega^2} \cos(\Omega t) + \frac{\eta_{12} a_1 F}{2(\Omega^2 + 2\omega_1 \Omega)} \cos[(\Omega + \omega_1)t + \beta_1] \Bigg\} + O(\epsilon^2)
\end{aligned} \tag{6.36}
$$

$$
\begin{aligned}
v_2 = a_2 \cos(\omega_2 t + \beta_2) - \epsilon \Bigg\{ & \frac{(\alpha_{22} - \omega_1^2 \delta_{22}) a_1^2 + (\alpha_{24} - \omega_2^2 \delta_{24}) a_2^2}{2\omega_2^2} \\
& - \frac{\omega_1 \mu_{21} a_1}{\omega_2^2 - \omega_1^2} \sin(\omega_1 t + \beta_1) - \frac{\eta_{22} a_2 F}{2(2\omega_2 \Omega - \Omega^2)} \cos[(\Omega - \omega_2)t - \beta_2] \\
& - \frac{(\alpha_{24} - 3\omega_2^2 \delta_{24}) a_2^2}{6\omega_2^2} \cos(2\omega_2 t + 2\beta_2) + \frac{(\alpha_{22} + \omega_1^2 \delta_{22}) a_1^2}{2(\omega_2^2 - 4\omega_1^2)} \cos(2\omega_1 t + 2\beta_1) \\
& - \frac{(\alpha_{23} + \omega_1 \omega_2 \delta_{23} - \omega_2^2 \delta_{23}) a_1 a_2}{\omega_1^2 - 2\omega_1 \omega_2} \cos[(\omega_2 - \omega_1)t - \beta_1 + \beta_2] \\
& - \frac{(\alpha_{23} - \omega_1 \omega_2 \delta_{23} - \omega_2^2 \delta_{23}) a_1 a_2}{\omega_1^2 + 2\omega_1 \omega_2} \cos[(\omega_1 + \omega_2)t + \beta_1 + \beta_2] \\
& - \frac{\eta_{21} F}{\omega_2^2 - \Omega^2} \cos(\Omega t) + \frac{\eta_{22} a_2 F}{2(\Omega^2 + 2\omega_2 \Omega)} \cos[(\Omega + \omega_2)t + \beta_2] \Bigg\} + O(\epsilon^2)
\end{aligned} \tag{6.37}
$$

where a_1, a_2, and γ are governed by Equations (6.30), (6.32), and (6.34).

It is clear from Equation (6.36) that the response of the first mode is expected to contain components at DC and near ω_2, $2\omega_1$, $2\omega_2$, $\omega_1 + \omega_2$, $\omega_2 - \omega_1$, and $2\omega_1 + \omega_2$. The components near $2\omega_1$, $2\omega_2$, and $\omega_2 - \omega_1$ are either very small or not present, which we demonstrate in Figure 6.1. It is clear from Equation (6.37) that the response of the second mode is expected to contain components at DC and near ω_1, $2\omega_1$, $2\omega_2$, $\omega_1 + \omega_2$, $\omega_2 - \omega_1$, and $\omega_1 + 2\omega_2$. The components near $2\omega_1$, $2\omega_2$, and $\omega_2 - \omega_1$ are either very small or not present. Furthermore, the level of approximation does not capture the entire harmonic character. This approach

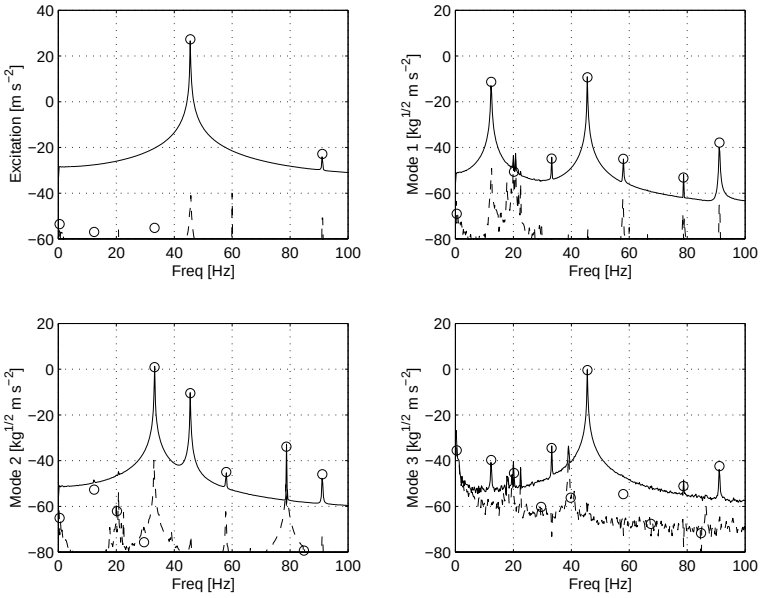

Figure 6.1: Typical discrete Fourier transform and circular-hyperbolic decomposition based power spectral densities of the excitation and modal accelerations: – DFT PSD; o CHD PSD; and - - - error DFT PSD

is justified by observing that the most significant frequencies can be explained, by several orders of magnitude, by Equations (6.36) and (6.37), as predicted.

6.3 Two-Period Quasiperiodic Motions

Two-Period quasiperiodic motions correspond to constant a_1, a_2, and γ; that is, the fixed points or equilibrium solutions of Equations (6.30), (6.32), and (6.34). Letting $a_1' = 0$,

$a_2' = 0$, and $\gamma' = 0$ in Equations (6.30), (6.32), and (6.34), we obtain either $a_1 = a_2 = 0$ or

$$a_1 = \frac{3\omega_1^2\mu_{13}}{8\mu_{11}} + \frac{\Gamma_5}{\omega_1\mu_{11}}Fa_2\sin\gamma + \frac{\Gamma_6}{\omega_1\mu_{11}}Fa_2\cos\gamma \tag{6.38}$$

$$a_2 = \frac{3\omega_2^2\mu_{23}}{8\mu_{22}} + \frac{\Gamma_{11}}{\omega_2\mu_{22}}Fa_1\sin\gamma + \frac{\Gamma_{12}}{\omega_2\mu_{22}}Fa_1\cos\gamma \tag{6.39}$$

$$\begin{aligned} -\omega_1\omega_2 a_1 a_2\sigma = {} & (\omega_2\Gamma_1 + \omega_1\Gamma_7)a_1a_2 \\ & + (\omega_2\Gamma_2 + \omega_1\Gamma_9)a_1^3a_2 + (\omega_2\Gamma_3 + \omega_1\Gamma_8)a_1a_2^3 + (\omega_2\Gamma_4 + \omega_1\Gamma_{10})a_1a_2F^2 \\ & + \omega_2(\Gamma_5\cos\gamma - \Gamma_6\sin\gamma)Fa_2^2 + \omega_1(\Gamma_{11}\cos\gamma - \Gamma_{12}\sin\gamma)Fa_1^2 \end{aligned} \tag{6.40}$$

where use has been made of the fact that $\mu_{11} \neq 0$ and $\mu_{22} \neq 0$. Equations (6.38)-(6.40) are known collectively as the modulation or evolution equations.

Mathematically, it is trivial to pursue the frequency-response equations from the modulation equations. First, one solves Equations (6.38) and (6.39) for γ, see [61]. This provides two relations for γ as a function of a_1, a_2, and F. However, both of these relations must be satisfied, which provides a constraint $a_1 = a_1(a_2, F)$ or $a_2 = a_2(a_1, F)$. This constraint and one of the solutions for γ are substituted into Equation (6.40), which represents one expression of the frequency-response equation.

Although this procedure is mathematically straightforward, the resulting frequency-response equation is difficult to work with for parameter estimation purposes. For instance, the inclusion of nonlinear damping results in the solution for γ to include trigonometric terms of the model parameters to be estimated and renders the constraint $a_1 = a_1(a_2, F)$ to be nonlinear. This is not to say that utilization of the frequency-response equation is without hope, even under these circumstances. Rather, I think that there is a more straightforward approach. Knowing a_1, a_2, and γ, we can estimate the system parameters directly from the modulation equations, which is the avenue pursued here.

6.4 Experiment

Figures 2.1 and 2.2 illustrate the geometry of the structure. The experimental apparatus is described in Chapter 2. Briefly, the excitation is measured by an accelerometer studded to the base and the response of the structure is measured using three accelerometers. The locations for these three accelerometers are chosen with the intent to distinguish among the responses of the first three modes. The placement of the accelerometers are shown in Figure 2.2 and further documented in Table 2.1. The other modes of the structure are ignored with the justification that their frequencies are well separated from the first and second modes and that their responses were not observed in preliminary test, as described in Chapter 3.

The structure is fixed to a vertical 4000 N (900 lbf) shaker table, as shown in Figure 2.2. The structure is excited via base excitation. A signal generator is used to drive the shaker amplifier. The data are acquired using a four-channel dynamic signal analyzer in the time-capture mode, which also provides amplification and signal conditioning for the accelerometers. The structure is excited near the sum of the natural frequencies of the first and second modes. The experiment includes two testing sequences, which are run during several different days. For each excitation condition, 10 ensembles are acquired. Each ensemble involves four channels of simultaneous data sampled at 256 Hz with a duration of 4 seconds each.

In the first test sequence, the excitation amplitude is held nearly constant, at approximately $23.3ms^{-2}$, as the frequency is swept. First, the frequency is swept forward from low-to-high values. Initially, there is no significant response away from the excitation frequency. Then, at $\Omega = 45.53$ Hz, the structure apparently underwent a bifurcation, resulting in a *jump* to a moderate-amplitudes motion involving the first and second modes near their natural frequencies. For each excitation frequency, we waited a significant period of time, typically between 20 minutes and 2 hours, to ensure stationary motions. Even at these lengths, there is noticeable variance in the data, which we illustrate in Figures 6.2 and 6.3. As the excitation frequency is increased, these motions continue to decrease to the point that there is no significant response away from the excitation frequency. Subsequently, the

excitation frequency is swept in reverse from high-to-low values. Initially, there is no significant observed response away from the excitation frequency. Then, between $\Omega = 45.575$ Hz and $\Omega = 45.59$ Hz, the response of the structure apparently underwent a bifurcation, resulting in moderate-amplitude motions involving the first and second modes near their natural frequencies. This time there is no large initial upward jump. As the frequency is decreased further, the response amplitudes continue to grow. Ultimately, as Ω is decreased below 45.525 Hz, the response amplitudes bifurcate again and the response *falls-down* sharply. At this juncture, there is no significant observed response away from the excitation frequency. This frequency sweep is documented by the experimental frequency-response curves of Figure 6.2. The multiple estimates for a given frequency represent individual ensembles, recalling that we acquired 10 ensembles for each excitation condition.

For parameter estimation purposes, we take $\omega_1 + \omega_2 = 45.56$ Hz, which is the midpoint between the *jump-up* frequencies and the intersection of the nontrivial and null solutions. From Table 2.4, we expected this value to be 45.738 Hz, which represents only a 0.39% difference in absolute terms, but is significant when considering the detuning, or frequency, range of the observed combination resonance.

In the second test sequence, the excitation frequency is held constant at 45.54 Hz and the amplitude of excitation is varied. For each level of excitation, we waited a significant period of time to ensure stationary motions. Initially, there is no significant observed response away from the excitation frequency. As the amplitude excitation is increased, the structure undergoes a bifurcation, resulting in small-amplitude motions of the first and second modes near their natural frequencies. As the excitation amplitude is increased, the small-amplitude motions grow to be moderate-amplitude motions. As the excitation amplitude is decreased, the motions decay and ultimately there are no significant responses away from the excitation frequency. The time required precludes executing both a forward and reverse amplitude sweep during the same day. Hence, we choose only to conduct a reverse amplitude sweep due to the time involved. However, we are encouraged that, during preliminary testing, a few abridged forward and reverse amplitude sweeps demonstrated that the response ampli-

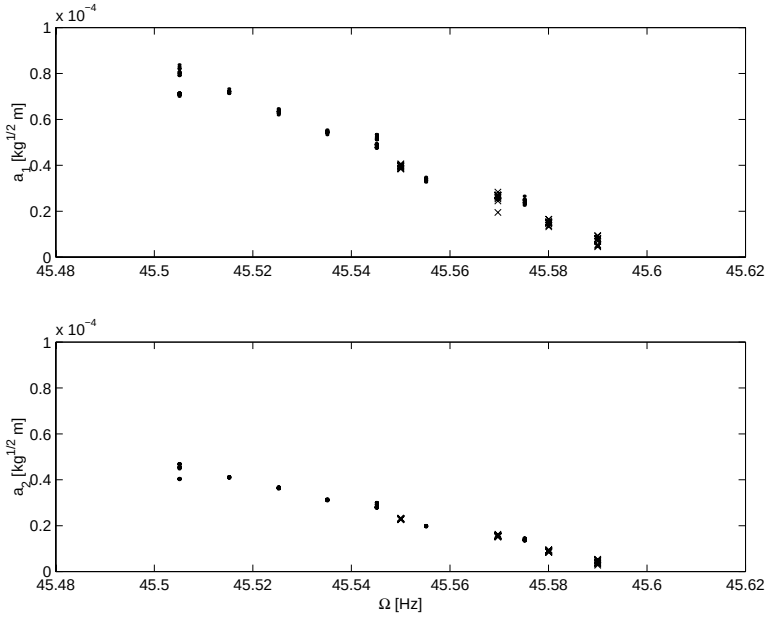

Figure 6.2: Experimental frequency-response curves for $F \approx 23.3ms^{-2}$: x forward sweep; . reverse sweep

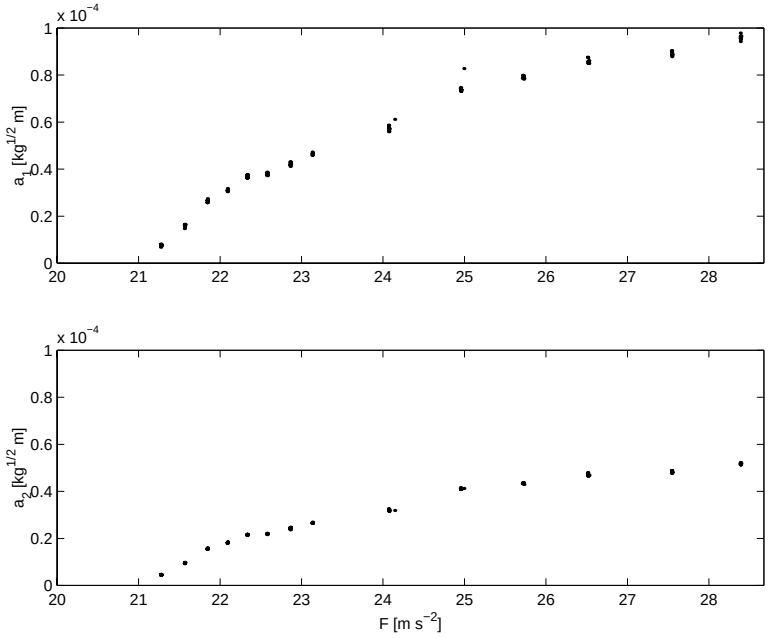

Figure 6.3: Experimental force-response curves with decreasing levels of excitation for $\Omega \approx$ 45.54 Hz

tudes generally agreed, given the same excitation conditions, and are independent of the direction of the sweep. We show the experimental force-response curves in Figure 6.3, which demonstrates supercritical behavior.

In Figure 6.1, we report results in terms of modal accelerations. In Figure 6.2 and 6.3, we report results in terms of modal displacements. However, we obtain our data in terms of physical accelerations. Obviously, we transform from the physical accelerations to the modal accelerations, which is accomplished via Equation (3.19). Then, we obtain the corresponding Fourier coefficients via the circular-hyperbolic decomposition (CHD) of Chapter 4. In order to transform from acceleration to displacement, we divide these Fourier coefficients by the square of their corresponding complex circular frequencies.

Here, CHD is vital because the discrete Fourier transform (DFT) gives a biased result due to leakage. CHD also improves the consistency of the Fourier coefficients. We can certainly select Ω to be periodic within a sampling window, in which case the DFT provides the correct result for that frequency component. However, the nature of the structure defines ω_1 and ω_2, which will not generally be periodic in any sampling window for which Ω is periodic. The reason is that neither ω_1 nor ω_2 can be ensured to be rational multiples of Ω; that is, the response is two-period quasiperiodic. The obvious exception is internal resonance, (i.e. $2\omega_1 = \omega_2$), which is not the present case.

6.5 Parameter Identification

In this section, we attempt to estimate the model parameters for the first two modes of the two-mass structure. We use the data obtained for the force- and frequency-response curves in Figures 6.2 and 6.3 along with a few additional sets of data that were not part of these sweeps. We take advantage of the harmonic distortion explained by Equations (6.36) and (6.37) to estimate some of the parameters. Then, we minimize the sum of the squared errors of approximate expressions based on the modulation equations for the remaining parameters.

We repeatedly make use of the so-called pseudo-matrix inverse, denoted $[\ ]^+$, as an

integral part of the parameter estimation process. As explained in Chapter 4, the expression

$$\{A\} = [X]^{+}[Y] \tag{6.41}$$

is equivalent to solving the least-squares problem for

$$[Y] - [X]\{A\} = \{E\} \tag{6.42}$$

where in the statistics community X, Y, A, and E are known as control variables, observation variables, model parameters, and the differences, or errors, between the observation variables and the model, respectively. Assuming real quantities, one can take the least square problem as: finding A such that $E^T E$ is a minimum. The quantity $E^T E$ is also know as the Euclidean norm.

We begin by exploiting the *observable* frequency content of the first mode response at ω_2, $\omega_2 + \omega_1$, and $\omega_2 + 2\omega_1$ for each excitation condition; that is, we consider the sum of the experimental data in groups of 10 ensembles. From Equation (6.36), we obtain the following approximate expressions:

$$\begin{Bmatrix} \mu_{12} \\ \eta_{12} \end{Bmatrix} = \begin{bmatrix} \mathrm{Re}[\frac{-i\omega_2 V_{2,1}(\omega_2)}{2(\omega_1^2-\omega_2^2)}] & \mathrm{Re}[\frac{\bar{V}_{1,1}(\omega_1)F_1(\Omega)}{4(2\omega_1\Omega-\Omega^2)}] \\ \mathrm{Re}[\frac{-i\omega_2 V_{2,2}(\omega_2)}{2(\omega_1^2-\omega_2^2)}] & \mathrm{Re}[\frac{V_{1,2}(\omega_1)F_2(\Omega)}{4(2\omega_1\Omega-\Omega^2)}] \\ \vdots & \vdots \\ \mathrm{Re}[\frac{-i\omega_2 V_{2,10}(\omega_2)}{2(\omega_1^2-\omega_2^2)}] & \mathrm{Re}[\frac{\bar{V}_{1,10}(\omega_1)F_{10}(\Omega)}{4(2\omega_1\Omega-\Omega^2)}] \\ \mathrm{Im}[\frac{-i\omega_2 V_{2,1}(\omega_2)}{2(\omega_1^2-\omega_2^2)}] & \mathrm{Im}[\frac{\bar{V}_{1,1}(\omega_1)F_1(\Omega)}{4(2\omega_1\Omega-\Omega^2)}] \\ \mathrm{Im}[\frac{-i\omega_2 V_{2,2}(\omega_2)}{2(\omega_1^2-\omega_2^2)}] & \mathrm{Im}[\frac{\bar{V}_{1,2}(\omega_1)F_2(\Omega)}{4(2\omega_1\Omega-\Omega^2)}] \\ \vdots & \vdots \\ \mathrm{Im}[\frac{-i\omega_2 V_{2,10}(\omega_2)}{2(\omega_1^2-\omega_2^2)}] & \mathrm{Im}[\frac{\bar{V}_{1,10}(\omega_1)F_{10}(\Omega)}{4(2\omega_1\Omega-\Omega^2)}] \end{bmatrix}^{+} \begin{Bmatrix} \mathrm{Re}[V_{1,1}(\omega_2)] \\ \mathrm{Re}[V_{1,2}(\omega_2)] \\ \vdots \\ \mathrm{Re}[V_{1,10}(\omega_2)] \\ \mathrm{Im}[V_{1,1}(\omega_2)] \\ \mathrm{Im}[V_{1,2}(\omega_2)] \\ \vdots \\ \mathrm{Im}[V_{1,10}(\omega_2)] \end{Bmatrix} \tag{6.43}$$

$$\begin{Bmatrix} \alpha_{22} - \omega_1\omega_2\delta_{22} - \omega_1^2\delta_{22} \\ \eta_{11} \end{Bmatrix} = \begin{bmatrix} \mathrm{Re}[\frac{V_{1,1}(\omega_1)V_{2,1}(\omega_2)}{2(\omega_2^2+2\omega_1\omega_2)}] & \mathrm{Re}[\frac{F_1(\Omega)}{2(\omega_1^2-\Omega^2)}] \\ \mathrm{Re}[\frac{V_{1,2}(\omega_1)V_{2,2}(\omega_2)}{2(\omega_2^2+2\omega_1\omega_2)}] & \mathrm{Re}[\frac{F_2(\Omega)}{2(\omega_1^2-\Omega^2)}] \\ \vdots & \vdots \\ \mathrm{Re}[\frac{V_{1,10}(\omega_1)V_{2,10}(\omega_2)}{2(\omega_2^2+2\omega_1\omega_2)}] & \mathrm{Re}[\frac{F_{10}(\Omega)}{2(\omega_1^2-\Omega^2)}] \\ \mathrm{Im}[\frac{V_{1,1}(\omega_1)V_{2,1}(\omega_2)}{2(\omega_2^2+2\omega_1\omega_2)}] & \mathrm{Im}[\frac{F_1(\Omega)}{2(\omega_1^2-\Omega^2)}] \\ \mathrm{Im}[\frac{V_{1,2}(\omega_1)V_{2,2}(\omega_2)}{2(\omega_2^2+2\omega_1\omega_2)}] & \mathrm{Im}[\frac{F_2(\Omega)}{2(\omega_1^2-\Omega^2)}] \\ \vdots & \vdots \\ \mathrm{Im}[\frac{V_{1,10}(\omega_1)V_{2,10}(\omega_2)}{2(\omega_2^2+2\omega_1\omega_2)}] & \mathrm{Im}[\frac{F_{10}(\Omega)}{2(\omega_1^2-\Omega^2)}] \end{bmatrix}^+ \begin{Bmatrix} \mathrm{Re}[V_{1,1}(\omega_1+\omega_2)] \\ \mathrm{Re}[V_{1,2}(\omega_1+\omega_2)] \\ \vdots \\ \mathrm{Re}[V_{1,10}(\omega_1+\omega_2)] \\ \mathrm{Im}[V_{1,1}(\omega_1+\omega_2)] \\ \mathrm{Im}[V_{1,2}(\omega_1+\omega_2)] \\ \vdots \\ \mathrm{Im}[V_{1,10}(\omega_1+\omega_2)] \end{Bmatrix} \tag{6.44}$$

and

$$\left\{\eta_{12}\right\} = \begin{bmatrix} \mathrm{Re}[-\frac{V_{1,1}(\omega_1)F_1(\Omega)}{4(\Omega^2+2\omega_1\Omega)}] \\ \mathrm{Re}[-\frac{V_{1,2}(\omega_1)F_2(\Omega)}{4(\Omega^2+2\omega_1\Omega)}] \\ \vdots \\ \mathrm{Re}[-\frac{V_{1,10}(\omega_1)F_{10}(\Omega)}{4(\Omega^2+2\omega_1\Omega)}] \\ \mathrm{Im}[-\frac{V_{1,1}(\omega_1)F_1(\Omega)}{4(\Omega^2+2\omega_1\Omega)}] \\ \mathrm{Im}[-\frac{V_{1,2}(\omega_1)F_2(\Omega)}{4(\Omega^2+2\omega_1\Omega)}] \\ \vdots \\ \mathrm{Im}[-\frac{V_{1,10}(\omega_1)F_{10}(\Omega)}{4(\Omega^2+2\omega_1\Omega)}] \end{bmatrix}^+ \begin{Bmatrix} \mathrm{Re}[V_{1,1}(2\omega_1+\omega_2)] \\ \mathrm{Re}[V_{1,2}(2\omega_1+\omega_2)] \\ \vdots \\ \mathrm{Re}[V_{1,10}(2\omega_1+\omega_2)] \\ \mathrm{Im}[V_{1,1}(2\omega_1+\omega_2)] \\ \mathrm{Im}[V_{1,2}(2\omega_1+\omega_2)] \\ \vdots \\ \mathrm{Im}[V_{1,10}(2\omega_1+\omega_2)] \end{Bmatrix} \tag{6.45}$$

where $V_{\ell,k}(\omega)$ and $F_k(\omega)$ are the one-side Fourier coefficients for the frequency ω of the ℓth modal displacement and excitation for the kth ensemble. It should be noted that these expressions provide two estimates of the parametric excitation coefficient η_{12}, which provide a check for the consistency of the estimation procedure. The results of the repeated application of Equations (6.43)-(6.45), for each collection of ensembles associated with an excitation condition, are documented in Figures 6.4-6.6 and summarized in Table 6.1 by the mean value.

Similarly, we exploit the *observable* frequency content of the second mode response at ω_1, $\omega_2+\omega_1$, and $2\omega_2+\omega_1$ for each excitation condition; that is, we consider the sum of the

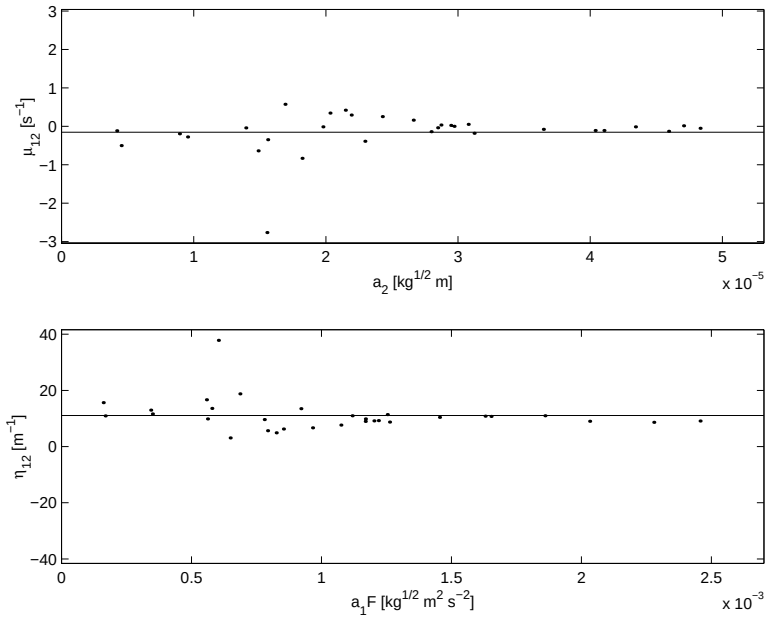

Figure 6.4: Ensemble estimates of μ_{12} and η_{12} from Equation 6.43

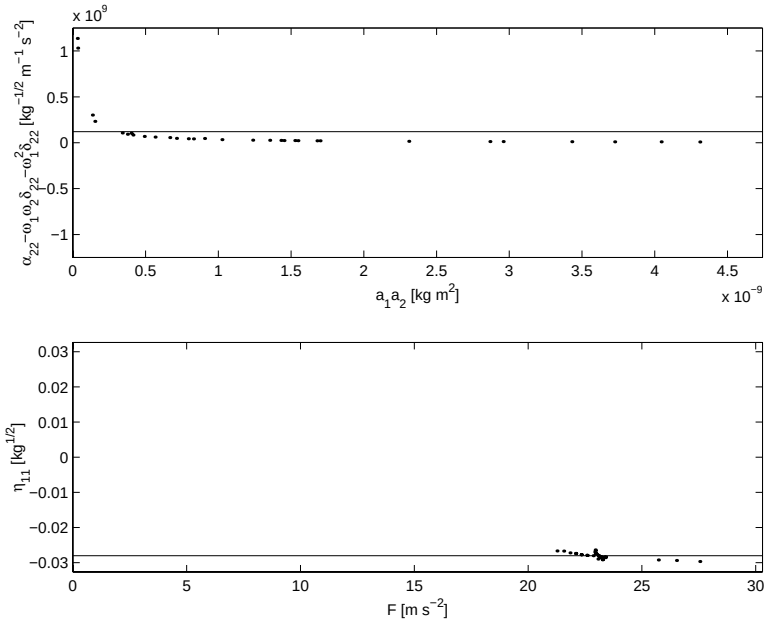

Figure 6.5: Ensemble estimates of $\alpha_{22} - \omega_1\omega_2\delta_{22} - \omega_1^2\delta_{22}$ and η_{11} from Equation 6.44

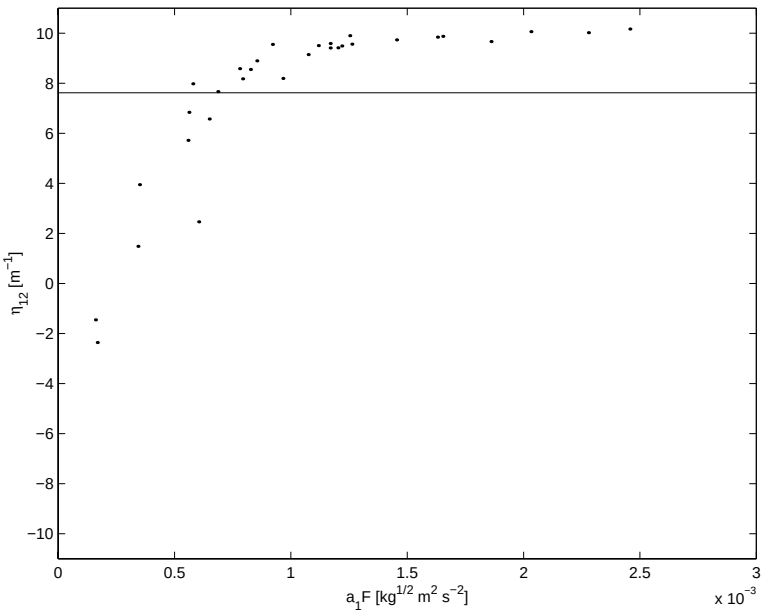

Figure 6.6: Ensemble estimates of η_{12} from Equation 6.45

data. From Equation (6.37), we obtain the following approximate expressions:

$$\begin{Bmatrix}\mu_{21}\\ \eta_{22}\end{Bmatrix} = \begin{bmatrix} \mathrm{Re}[\frac{-i\omega_1 V_{1,1}(\omega_1)}{2(\omega_2^2-\omega_1^2)}] & \mathrm{Re}[\frac{\bar{V}_{2,1}(\omega_2)F_1(\Omega)}{4(2\omega_2\Omega-\Omega^2)}] \\ \mathrm{Re}[\frac{-i\omega_1 V_{1,2}(\omega_1)}{2(\omega_2^2-\omega_1^2)}] & \mathrm{Re}[\frac{\bar{V}_{2,2}(\omega_2)F_2(\Omega)}{4(2\omega_2\Omega-\Omega^2)}] \\ \vdots & \vdots \\ \mathrm{Re}[\frac{-i\omega_1 V_{1,10}(\omega_1)}{2(\omega_2^2-\omega_1^2)}] & \mathrm{Re}[\frac{\bar{V}_{2,10}(\omega_2)F_{10}(\Omega)}{4(2\omega_2\Omega-\Omega^2)}] \\ \mathrm{Im}[\frac{-i\omega_1 V_{1,1}(\omega_1)}{2(\omega_2^2-\omega_1^2)}] & \mathrm{Im}[\frac{\bar{V}_{2,1}(\omega_2)F_1(\Omega)}{4(2\omega_2\Omega-\Omega^2)}] \\ \mathrm{Im}[\frac{-i\omega_1 V_{1,2}(\omega_1)}{2(\omega_2^2-\omega_1^2)}] & \mathrm{Im}[\frac{\bar{V}_{2,2}(\omega_2)F_2(\Omega)}{4(2\omega_2\Omega-\Omega^2)}] \\ \vdots & \vdots \\ \mathrm{Im}[\frac{-i\omega_1 V_{1,10}(\omega_1)}{2(\omega_2^2-\omega_1^2)}] & \mathrm{Im}[\frac{\bar{V}_{2,10}(\omega_2)F_{10}(\Omega)}{4(2\omega_2\Omega-\Omega^2)}] \end{bmatrix}^{+} \begin{Bmatrix} \mathrm{Re}[V_{2,1}(\omega_1)] \\ \mathrm{Re}[V_{2,2}(\omega_1)] \\ \vdots \\ \mathrm{Re}[V_{2,10}(\omega_1)] \\ \mathrm{Im}[V_{2,1}(\omega_1)] \\ \mathrm{Im}[V_{2,2}(\omega_1)] \\ \vdots \\ \mathrm{Im}[V_{2,10}(\omega_1)] \end{Bmatrix} \tag{6.46}$$

$$\begin{Bmatrix} \alpha_{23} - \omega_1\omega_2\delta_{23} - \omega_2^2\delta_{23} \\ \eta_{21} \end{Bmatrix} = \begin{bmatrix} \mathrm{Re}[\frac{V_{1,1}(\omega_1)V_{2,1}(\omega_2)}{2(\omega_1^2+2\omega_1\omega_2)}] & \mathrm{Re}[\frac{F_1(\Omega)}{2(\omega_2^2-\Omega^2)}] \\ \mathrm{Re}[\frac{V_{1,2}(\omega_1)V_{2,2}(\omega_2)}{2(\omega_1^2+2\omega_1\omega_2)}] & \mathrm{Re}[\frac{F_2(\Omega)}{2(\omega_2^2-\Omega^2)}] \\ \vdots & \vdots \\ \mathrm{Re}[\frac{V_{1,10}(\omega_1)V_{2,10}(\omega_2)}{2(\omega_1^2+2\omega_1\omega_2)}] & \mathrm{Re}[\frac{F_{10}(\Omega)}{2(\omega_2^2-\Omega^2)}] \\ \mathrm{Im}[\frac{V_{1,1}(\omega_1)V_{2,1}(\omega_2)}{2(\omega_1^2+2\omega_1\omega_2)}] & \mathrm{Im}[\frac{F_1(\Omega)}{2(\omega_2^2-\Omega^2)}] \\ \mathrm{Im}[\frac{V_{1,2}(\omega_1)V_{2,2}(\omega_2)}{2(\omega_1^2+2\omega_1\omega_2)}] & \mathrm{Im}[\frac{F_2(\Omega)}{2(\omega_2^2-\Omega^2)}] \\ \vdots & \vdots \\ \mathrm{Im}[\frac{V_{1,10}(\omega_1)V_{2,10}(\omega_2)}{2(\omega_1^2+2\omega_1\omega_2)}] & \mathrm{Im}[\frac{F_{10}(\Omega)}{2(\omega_2^2-\Omega^2)}] \end{bmatrix}^+ \begin{Bmatrix} \mathrm{Re}[V_{2,1}(\omega_1+\omega_2)] \\ \mathrm{Re}[V_{2,2}(\omega_1+\omega_2)] \\ \vdots \\ \mathrm{Re}[V_{2,10}(\omega_1+\omega_2)] \\ \mathrm{Im}[V_{2,1}(\omega_1+\omega_2)] \\ \mathrm{Im}[V_{2,2}(\omega_1+\omega_2)] \\ \vdots \\ \mathrm{Im}[V_{2,10}(\omega_1+\omega_2)] \end{Bmatrix} \quad (6.47)$$

and

$$\begin{Bmatrix} \eta_{22} \end{Bmatrix} = \begin{bmatrix} \mathrm{Re}[-\frac{V_{2,1}(\omega_2)F_1(\Omega)}{4(\Omega^2+2\omega_2\Omega)}] \\ \mathrm{Re}[-\frac{V_{2,2}(\omega_2)F_2(\Omega)}{4(\Omega^2+2\omega_2\Omega)}] \\ \vdots \\ \mathrm{Re}[-\frac{V_{2,10}(\omega_2)F_{10}(\Omega)}{4(\Omega^2+2\omega_2\Omega)}] \\ \mathrm{Im}[-\frac{V_{2,1}(\omega_2)F_1(\Omega)}{4(\Omega^2+2\omega_2\Omega)}] \\ \mathrm{Im}[-\frac{V_{2,2}(\omega_2)F_2(\Omega)}{4(\Omega^2+2\omega_2\Omega)}] \\ \vdots \\ \mathrm{Im}[-\frac{V_{2,10}(\omega_2)F_{10}(\Omega)}{4(\Omega^2+2\omega_2\Omega)}] \end{bmatrix}^+ \begin{Bmatrix} \mathrm{Re}[V_{2,1}(\omega_1+2\omega_2)] \\ \mathrm{Re}[V_{2,2}(\omega_1+2\omega_2)] \\ \vdots \\ \mathrm{Re}[V_{2,10}(\omega_1+2\omega_2)] \\ \mathrm{Im}[V_{2,1}(\omega_1+2\omega_2)] \\ \mathrm{Im}[V_{2,2}(\omega_1+2\omega_2)] \\ \vdots \\ \mathrm{Im}[V_{2,10}(\omega_1+2\omega_2)] \end{Bmatrix} \quad (6.48)$$

We note that these equations provide two separate estimates of the parametric excitation coefficient η_{22}, which provide another check for the consistency of the estimation procedure. The results of the repeated application of Equations (6.46)-(6.48) are documented by Figures 6.7-6.9 and are summarized in Table 6.1.

The parameter estimates in Table 6.1 generally provide reasonable agreement with previous results. The estimate of the external excitation coefficient η_{11} is approximately 56% greater than the value reported in Table 5.4 for η_1, which is the equivalent parameter from the previous chapter. The difference between these estimates of η_{11} is significant, but the estimates are of the same order of magnitude and the effect of this parameter on the overall system response is small. Since the effect of η_1 on η_e in Table 5.4 is small, we approximate η_2 as $4\eta_e$ for comparison purposes. The difference between the mean values of η_{12} in Table 6.1 and η_e in Table 5.4 are 44.0% and 0.8% for the estimates of Equations (6.43) and (6.45),

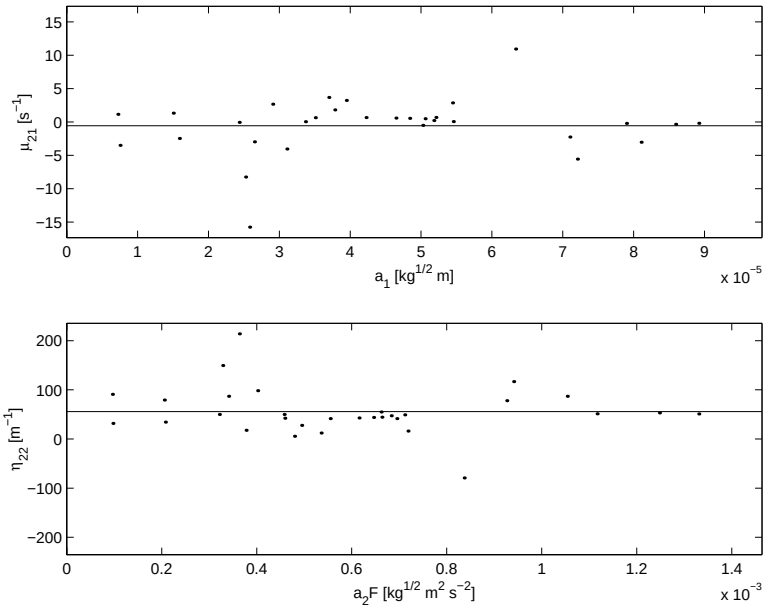

Figure 6.7: Ensemble estimates of μ_{21} and η_{22} from Equation 6.46

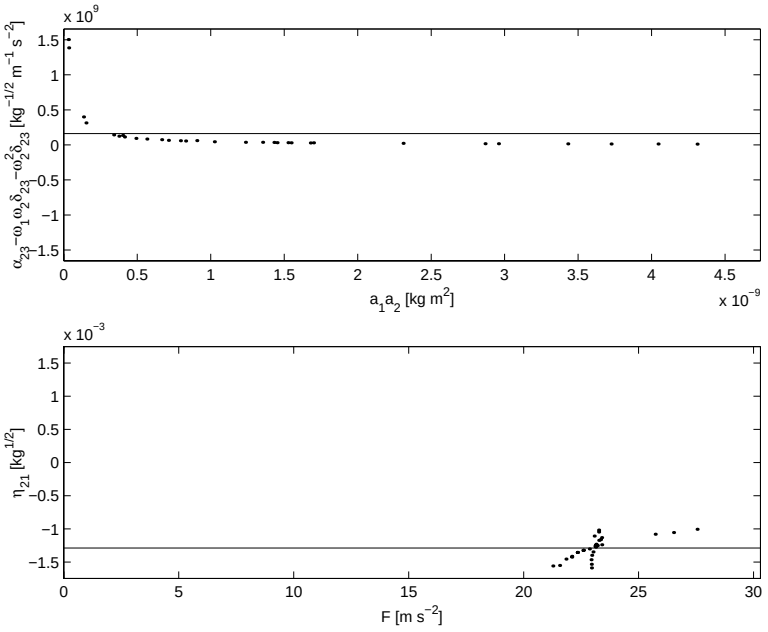

Figure 6.8: Ensemble estimates of $\alpha_{23} - \omega_1\omega_2\delta_{23} - \omega_2^2\delta_{23}$ and η_{21} from Equation 6.47

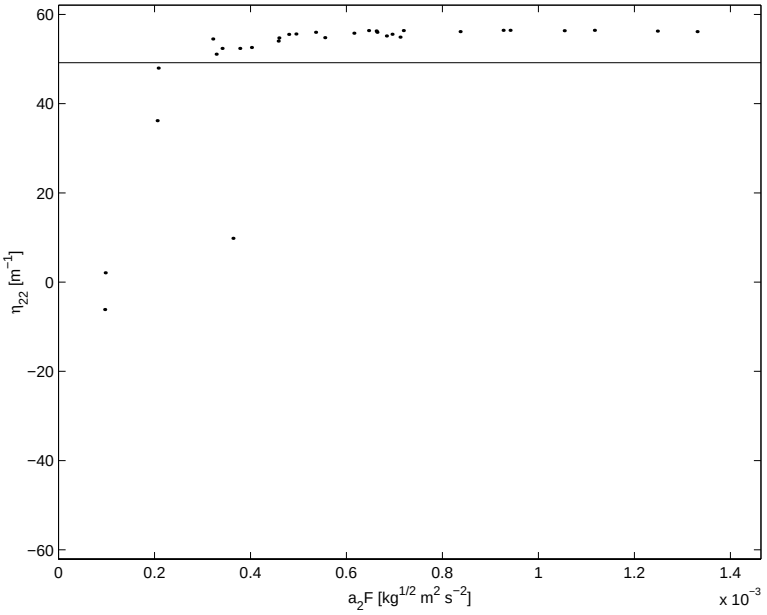

Figure 6.9: Ensemble estimates of η_{22} from Equation 6.48

Table 6.1: Parameter estimates from the frequency components of v_1 and v_2: () denotes the standard deviation of the preceding parameter estimate, and * denotes an estimate suspected of being biased.

Parameter Estimated	Parameter Estimate
μ_{12} from Eq. (6.43) $[s^{-1}]$	-0.1547 (0.564)
η_{12} from Eq. (6.43) $[m^{-1}]$	11.07 (5.96)
$\alpha_{22} - \omega_1\omega_2\delta_{22} - \omega_1^2\delta_{22}$ from Eq. (6.44) $[kg^{-1/2}m^{-1}s^{-2}]$	121.3×10^6 (265×10^6) *
η_{11} from Eq. (6.44) $[kg^{1/2}]$	-0.0280 (0.000864)
η_{12} from Eq. (6.45) $[m^{-1}]$	7.62 (3.36)
μ_{21} from Eq. (6.46) $[s^{-1}]$	-0.569 (4.33)
η_{22} from Eq. (6.46) $[m^{-1}]$	55.8 (49.1)
$\alpha_{23} - \omega_1\omega_2\delta_{23} - \omega_2^2\delta_{23}$ from Eq. (6.47) $[kg^{-1/2}m^{-1}s^{-2}]$	162.0×10^6 (353×10^6) *
η_{21} from Eq. (6.47) $[kg^{1/2}]$	-0.001287 (0.0001652)
η_{22} from Eq. (6.48) $[m^{-1}]$	49.2 (16.31)

respectively. These errors are within a standard deviation of the mean values reported in Table 6.1.

The linear damping terms μ_{12} and μ_{21} in Table 6.1 can not be reasonably distinguished from zero. This result is consistent with the conclusions drawn in Chapter 2. The quadratic nonlinearities $\alpha_{22} - \omega_1\omega_2\delta_{22} - \omega_1^2\delta_{22}$ and $\alpha_{23} - \omega_1\omega_2\delta_{23} - \omega_2^2\delta_{23}$ can not be reasonably distinguished from zero. Furthermore, examining Figures 6.5 and 6.8, we see that the estimates of the quadratic nonlinearities diverge when the response is small. The nature of this divergent behavior is not presently understood. Perhaps, the difference between the present estimate of η_{11} and the estimate of η_1 in Chapter 5 is related to this divergent behavior since η_{11} is also estimated using Equation (6.44)!

Next, we utilize the modulation equations that involve the damping parameters. We consider the sum of the experimental data. From Equations (6.30) and (6.32), we obtain the following approximate expressions:

$$\left\{ \begin{array}{c} \frac{3\omega_1^2\mu_{13}}{8\mu_{11}} \\ \frac{\Gamma_5}{\omega_1\mu_{11}} \\ \frac{\Gamma_6}{\omega_1\mu_{11}} \end{array} \right\} = - \left[\begin{array}{ccc} a_{1,1}^3 & F_1 a_{2,1} \sin\gamma_1 & F_1 a_{2,1} \cos\gamma_1 \\ a_{1,2}^3 & F_2 a_{2,2} \sin\gamma_1 & F_2 a_{2,2} \cos\gamma_2 \\ \vdots & \vdots & \dots \\ a_{1,N}^3 & F_N a_{2,N} \sin\gamma_1 & F_N a_{2,N} \cos\gamma_N \end{array} \right]^+ \left\{ \begin{array}{c} a_{1,1} \\ a_{1,2} \\ \vdots \\ a_{1,N} \end{array} \right\} \tag{6.49}$$

and

$$\left\{ \begin{array}{c} \frac{3\omega_2^2\mu_{23}}{8\mu_{22}} \\ \frac{\Gamma_{11}}{\omega_1\mu_{22}} \\ \frac{\Gamma_{12}}{\omega_1\mu_{11}} \end{array} \right\} = - \left[\begin{array}{ccc} a_{2,1}^3 & F_1 a_{1,1} \sin\gamma_1 & F_1 a_{1,1} \cos\gamma_1 \\ a_{2,2}^3 & F_2 a_{1,2} \sin\gamma_1 & F_2 a_{1,2} \cos\gamma_2 \\ \vdots & \vdots & \dots \\ a_{2,N}^3 & F_N a_{1,N} \sin\gamma_1 & F_N a_{1,N} \cos\gamma_N \end{array} \right]^+ \left\{ \begin{array}{c} a_{2,1} \\ a_{2,2} \\ \vdots \\ a_{2,N} \end{array} \right\} \tag{6.50}$$

where the phase difference $\gamma = \angle(F\bar{A}_1\bar{A}_2)$, which is actually the angle of a bispectral quantity. The second subscript following a_1 and a_2 and the subscript following F and γ are associated with a specific ensemble. The integer N is the total number of ensembles considered.

In Figures 10 and 11, we overlay the actual data with regenerated fits based on the parameter estimates obtained from Equations (6.49) and (6.50), respectively. We note that

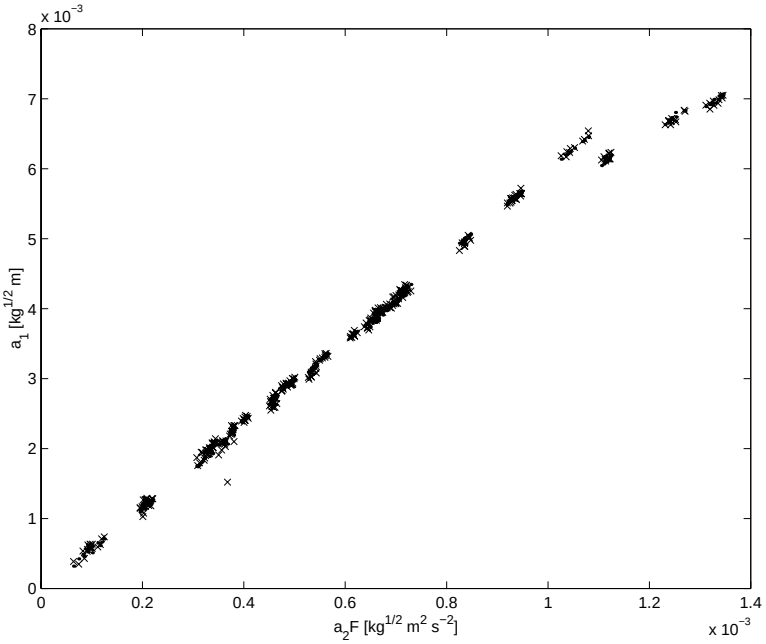

Figure 6.10: Overlay of data and fit from Equation (6.49): . data; x fit

the agreement between the original data and the regenerated fits is exceptional. The measures of correlation associated with Equations (6.49) and (6.50) are calculated to be 0.9997 and 0.9997, respectively. In Figures 12 and 13, we compare the relative contribution of the parameter estimates to the regenerated fits. In Figure 12, we also observe that the vast majority of the fit is attributable to $\Gamma_5/\omega_1\mu_{11}$, whereas $3\omega_1^2\mu_{13}/8\mu_{11}$ and $\Gamma_6/\omega_1\mu_{11}$ only account for about 1% and 2% of the regenerated fit, respectively. Considering the variance in the data, these latter estimates are suspect. In Appendix D, we pursue an analysis of the variance (ANOVA) and determine that the terms involving $3\omega_1^2\mu_{13}/8\mu_{11}$ and $\Gamma_6/\omega_1\mu_{11}$ are indeed statistically significant. In Figure 12, we observe that most of the fit is attributable to $\Gamma_{11}/\omega_2\mu_{22}$, but each of $3\omega_2^2\mu_{23}/8\mu_{22}$ and $\Gamma_{12}/\omega_2\mu_{22}$ accounts for a significant part, about 10%, of the regenerated fit.

Finally, we utilize the remaining modulation equation; that is, Equation (6.34). The terms involving $\sin\gamma$ and $\cos\gamma$ can be grouped with the observation that $\Gamma_5 \approx \Gamma_{11}$ from Equations (6.9) and (6.27) and that the ratios Γ_6/Γ_5 and Γ_{12}/Γ_{11} are known from the results of Equations (6.49) and (6.50). From Equation (6.34), we obtain the following approximate

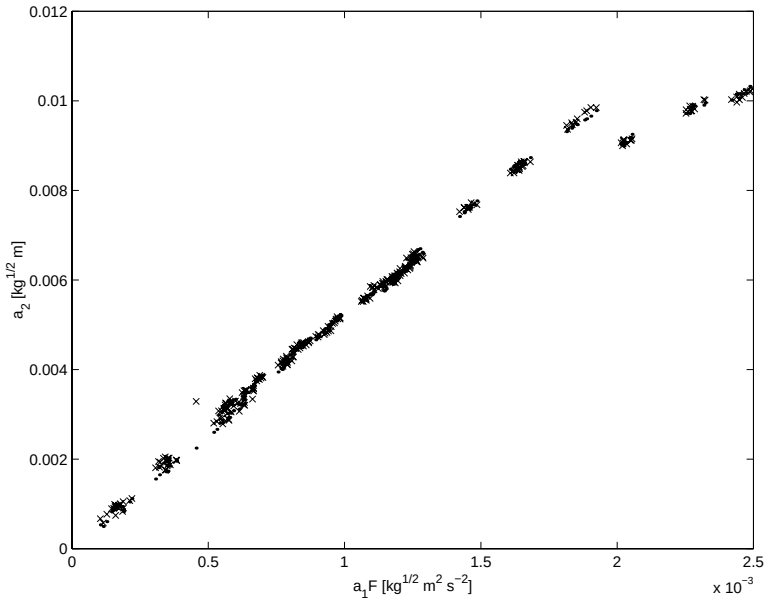

Figure 6.11: Overlay of data and fit from Equation (6.50): . data; x fit

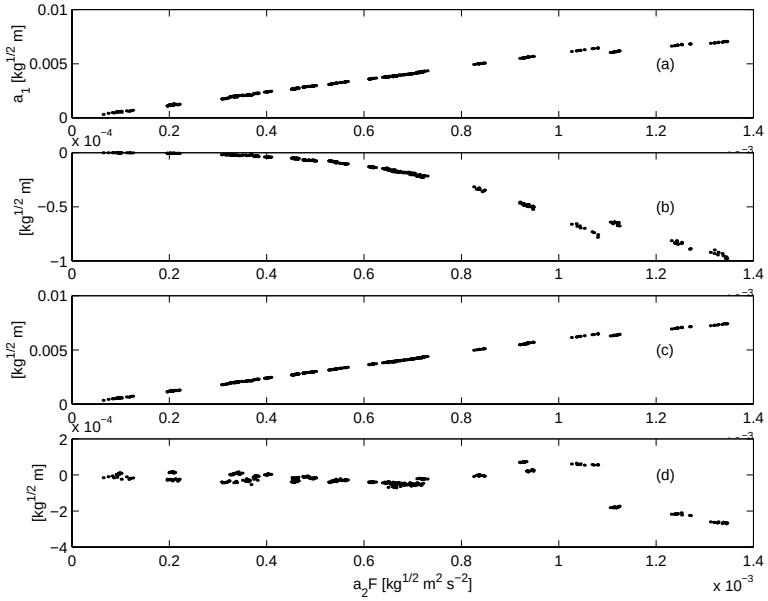

Figure 6.12: Comparison of relative contributions to the fit from Equation (6.49): (a) all parameters, (b) part attributed to $3\omega_1^2\mu_{13}/8\mu_{11}$, (c) part attributed to $\Gamma_5/\omega_1\mu_{11}$, and (d) part attributed to $\Gamma_6/\omega_1\mu_{11}$

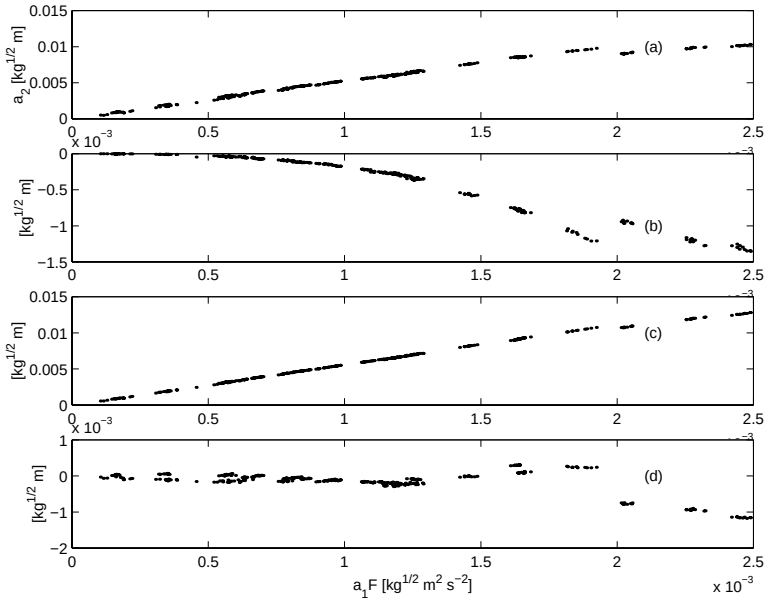

Figure 6.13: Comparison of relative contributions to the fit from Equation (6.49): (a) all parameters, (b) part attributed to $3\omega_2^2\mu_{23}/8\mu_{22}$, (c) part attributed to $\Gamma_{11}/\omega_2\mu_{22}$, and (d) part attributed to $\Gamma_{12}/\omega_2\mu_{22}$

expression:

$$\begin{Bmatrix} \omega_2\Gamma_1 + \omega_1\Gamma_7 \\ \omega_2\Gamma_2 + \omega_1\Gamma_9 \\ \omega_2\Gamma_3 + \omega_1\Gamma_8 \\ \omega_2\Gamma_4 + \omega_1\Gamma_{10} \\ \Gamma_5 \end{Bmatrix} = \tag{6.51}$$

$$- \begin{bmatrix} a_{1,1}a_{2,1} & a_{1,1}^3 a_{2,1} & a_{1,1}a_{2,1}^3 & a_{1,1}a_{2,1}F_1^2 & \tilde{F}_1 \\ a_{1,2}a_{2,2} & a_{1,2}^3 a_{2,2} & a_{1,2}a_{2,2}^3 & a_{1,2}a_{2,2}F_2^2 & \tilde{F}_2 \\ \vdots & \vdots & \vdots & \vdots & \vdots \\ a_{1,N}a_{2,N} & a_{1,N}^3 a_{2,N} & a_{1,N}a_{2,N}^3 & a_{1,N}a_{2,N}F_N^2 & \tilde{F}_N \end{bmatrix}^+ \begin{Bmatrix} \omega_1\omega_2 a_{1,1}a_{2,1}\sigma_1 \\ \omega_1\omega_2 a_{1,2}a_{2,2}\sigma_2 \\ \vdots \\ \omega_1\omega_2 a_{1,N}a_{2,N}\sigma_N \end{Bmatrix}$$

where

$$\tilde{F}_k = \omega_2 F_k a_{2,k}^2 \cos\gamma_k - \frac{\Gamma_6}{\Gamma_5}\omega_2 F_k a_{2,k}^2 \sin\gamma_k + \omega_1 F_k a_{1,k}^2 \cos\gamma_k - \frac{\Gamma_{12}}{\Gamma_5}\omega_1 F_k a_{1,k}^2 \sin\gamma_k \tag{6.52}$$

Table 6.2: Parameter estimates from the modulation equations: * denotes an estimate suspected of being biased.

Parameter Estimated	Parameter Estimate
μ_{11} $[s^{-1}]$	0.273
μ_{22} $[s^{-1}]$	0.293
μ_{13} $[kg^{-1}m^{-2}s]$	229
μ_{23} $[kg^{-1}m^{-2}s]$	1006
Γ_5,Γ_{11} $[m^{-1}]$	1.651
Γ_6 $[m^{-1}]$	-0.1351
Γ_{12} $[m^{-1}]$	-0.342
$\omega_2\Gamma_1 + \omega_1\Gamma_7$ $[s^{-3}]$	-587
$\omega_2\Gamma_2 + \omega_1\Gamma_9$ $[kg^{-1}m^{-2}s^{-3}]$	-111.8×10^9 *
$\omega_2\Gamma_3 + \omega_1\Gamma_8$ $[kg^{-1}m^{-2}s^{-3}]$	353×10^9 *
$\omega_2\Gamma_4 + \omega_1\Gamma_{10}$ $[m^{-2}s]$	7.77

and σ_k is the detuning parameter, defined in Equation (6.9), with the subscript k is associated with a specific ensemble. We provide a summary of the results obtained from Equations (6.49)-(6.51) in Table 6.2. The correlation between the data and a regenerated fit based on Equation (6.51) provides a correlation measure of 0.996, which we consider to be very good.

We encounter a dilemma in the implementation of Equation (6.51). Even with balancing columns, the pseudo-matrix inversion is not as well conditioned as we desire. By balancing, we mean weighting the columns such that the variances are equal. If we use singular value decomposition, as in Equation (3.8), $D(5)/D(1) = 0.00377$. This is quite reasonable from a numerical standpoint; yet, it is problematic from the perspective of parameter estimation. When we utilize the method of least-squares, we assume that the control parameters are statistically independent. Here, the concern is that two or more columns, or independent linear combinations of the columns, may have a similar appearance. We did not encounter this dilemma in the previous chapter. We did not encounter this dilemma in the implementation of Equations (6.49) or (6.50). In appendix D, we detail an ANOVA to establish the

statistical significance of the model parameters of Equation (6.51). From this analysis, we conclude that the columns $a_1 a_2^3$ and $a_1^3 a_2$ are not statistically independent.

The root of this dilemma comes from the fact that for, the observed data, a_1/a_2 is almost fixed. Solving Equations (6.30) and (6.32) for γ, we find a nonlinear relationship between a_1 and a_2 and conclude that a_1/a_2 is not constant. If a_1/a_2 had been constant, then we could at least merge $a_1 a_2^3$ and $a_1^3 a_2$ into a single control parameter. The resulting parameter estimate would be lumped, but statistically significant. Unfortunately, the present relation between a_1 and a_2 does not permit this in a rigorous or physically significant way.

If we used the parameter estimates in Table 6.2 to predict the observed response of the system, we would have found favorable results. However, this does not mean that the results are physically meaningful. For example, both $1 + 3$ and $24 - 20$ provide the same result, but have different underlying meanings. We accept the parameter estimates documented in Table 6.2 with the reservation that the estimates of $\omega_2\Gamma_2 + \omega_1\Gamma_9$ and $\omega_2\Gamma_3 + \omega_1\Gamma_8$ are suspect.

The estimate of μ_{13} is almost an order of magnitude different from the cubic damping coefficient μ_3 obtained in Chapter 5. This model parameter is statistically significant. But, it is poorly emphasized. The contribution of this model parameter to the overall fit is only about 1%. If we used the estimate from Chapter 5, then the contribution would be reduced to about 0.2%. Any errors in the other parameter estimates can have a significant influence on the estimate of μ_{13}. Perhaps, better agreement would have been found if the response amplitude had been larger, thus emphasizing this model parameter.

The estimates for μ_{11} and μ_{22} in Table 6.2 are very close to the linear parameter estimates documented in Table 2.4. The corresponding differences are 4.7% and 1.2%, respectively. This is well within the first standard deviation of the parameter estimates documented in Table 2.4. Here, the estimate for μ_{11} is closer to the linear estimate than the estimate of the linear damping parameter μ_1 obtained in Chapter 5.

6.6 Summary

In this chapter, we estimate the linear and nonlinear parameters of the first and second modes of a two-mass structure. We observe a combination resonance of the additive type, which emphasizes the coupling between the first and second modes. We assume that the system is governed by two coupled nonlinear second-order ordinary-differential equations, including linear and cubic damping, linear damping coupling, quadratic and cubic geometric and inertia nonlinearities, and external and parametric excitation terms. Using the method of multiple scale, we find a uniform solution for these equations when the excitation frequency Ω is near the sum $\omega_1 + \omega_2$ of the first and second modal frequencies.

From this uniform solution, we estimate the parameters involving the linear damping coupling terms, quadratic geometric and inertia nonlinearities, and external and parametric excitation terms by forming an approximate expression relating the frequency content of the response and the uniform solution itself. From the modulation equations, we estimate the parameters involving the linear and cubic damping, linear damping coupling, quadratic and cubic geometric and inertia nonlinearities, and external and parametric excitation terms.

Not all of the model parameter can be estimated with combining terms. For instance, we are unable to decouple the geometric and inertia nonlinearities. Other model parameters have an influence on the behavior of the structure that are can not be distinguished from the influence of one or more other model parameters. Still other model parameters are not statistically different from zero. However, we are able to uncover a great deal of information about the underlying nature of this structure.

Chapter 7

Final Remarks

7.1 Summary

We developed and provided proof of principle for parameter identification techniques of structural systems that can be described in terms of one or two nonlinear normal modes. We modeled the dynamics of those modes with second-order ordinary-differential equations based on the principles of mechanics, past experience, and engineering judgment. We performed a number of experiments on a two-mass structure using several different forms of excitation. First, we estimated the linear parameters using linear tests and estimation procedures. Then, we developed a mathematical model to describe the nonlinear dynamic behavior of two nonlinear normal modes. The model involves second-order ordinary-differential equations possessing quadratic and cubic geometric and inertia nonlinearities; linear, quadratic, and cubic damping; and parametric and external excitation terms. Other nonlinearities, such as material nonlinearity, could easily be incorporated. We used the method of multiple scales to determine second-order uniform expansions of the model equations and hence approximations to the response of the structure. Finally, we derived new parameter estimation procedures to obtain the linear and nonlinear parameters using regressive fits between the theoretically obtained response relations and those obtained experimentally. These procedure are classified

as frequency-domain techniques.

Additionally, we developed a new signal processing procedure for uncovering circular and hyperbolic sine and cosine functions from finite time series. This procedure was very helpful, particularly in Chapter 6, since we were unable to ensure signal periodicity for some of the nonlinear tests. Hence, using the discrete Fourier transform would have provided biased frequency, amplitude, and phase parameters. Accordingly, this difficulty was circumvented.

7.2 Parameter Estimation

We began with estimating the linear system parameters for the first several structural modes of the two-mass structure via experimental observation of the free-decay system response and the system responses to an impact excitation and a base excitation. Estimates of the resonant frequencies, damping factors, mode shapes, and modal masses were obtained. However, the results from the free-decay and base excitation data strongly suggested the presence of nonlinearities due to damping and either stiffness and/or inertia.

With the suspicion of nonlinearity, we sought and found nonlinear resonances that *emphasized* the nonlinearity. In fact, these resonances can not be explained by a linear model. The two observed forms of nonlinear resonances include a combination of a principal parametric resonance and a subharmonic resonance of order one-half and a combination resonance of the additive type.

We advocated and provided proof of principle for the novel concept of exploiting nonlinear resonances as an integral part of the estimation process, as proposed by Nayfeh [59]. To identify the parameters of the first mode, we sought and found a nonlinear phenomenon by exciting the structure near twice its natural frequency. The behavior is consistent with a combination of a principal parametric resonance and a subharmonic resonance of order one-half. We used the method of multiple scales to determine a second-order uniform expansion of the model equation and hence the response of the structure. We estimated the linear and nonlinear parameters by regressive fits of the theoretically obtained response relations to

those obtained experimentally. There is generally good agreement between the experiment and the model. In the Dissertation of Tabaddor [80], it was suggested that more work need to be done to compare the linear damping estimates obtained by linear procedures to those obtained by exploiting subharmonic resonance. We accomplished this task and found that there is good agreement between the linear parameter estimates obtained by the linear procedure and the linear parameter estimates obtained by the nonlinear procedure. This suggests that the nonlinear procedure presented in this Dissertation provides reasonable results.

We found that we were unable to separate the geometric and corresponding inertia nonlinearities by this procedure, which represents a limitation of the procedure. However, this limitation is not unique to our procedure. Most other estimation procedures suffer from the same or more extreme limitations, since the geometric and inertia (and material) nonlinearities have qualitatively similar effects on the response. Furthermore, the method of multiple scale uncovers the combined effects of the different nonlinearities on the response. Although some terms can not be separated, we avoid ill-conditioning of the estimation procedure itself, which is an important advantage.

We continued and described a new procedure for the identification of the linear and nonlinear parameters for two nonlinear normal modes of a structure, including linear and nonlinear coupling terms. We sought and found a nonlinear phenomenon by exciting the structure near the sum of the natural frequencies of the first and second modes. We used it to estimate the linear and nonlinear parameters of the first and second modes of the two-mass structure. The behavior is consistent with a combination resonance of the additive type. We used the method of multiple scales to determine a second-order uniform expansion of the model equations and hence the response of the structure. We estimated the linear and nonlinear parameters by regressive fits of the theoretically obtained response relations to those obtained experimentally, which are generally good.

We compared the estimated linear damping term of the first mode with those obtained by the linear and first nonlinear procedures; the results are favorable. Most of the nonlinear

and excitation terms obtained with the two nonlinear procedures are in good agreement. The terms that lacked agreement were, in general, poorly emphasized by the nonlinear resonances considered. As before, we were unable to separate the effects of many of the nonlinearities, which represents a significant limitation of the procedure. Again, this limitation is not unique to our procedure. The reason for this is that many of the effects of the nonlinearities on the nonlinear resonance are not qualitatively different.

In sum, comparisons of the parameter estimates among the various estimation procedures are generally good when the estimated parameters are emphasized.

7.3 Future Work

We made significant advances in this Dissertation. However, the field of mechanics is an evolving one. There is always room for further advancement. The following items are suggestions for future work:

1. Testing was extremely time consuming. Accordingly, it would be difficult to apply this technique to many practical engineering problems. Reducing the test requirements and/or the time involved with testing would facilitate greater application.

2. In our considerations, some parameters could not be distinguished from zero. A better understanding about what data is needed to emphasize given parameters would improve the ability to obtain high-quality estimates.

3. The geometric and inertia nonlinearities could not be distinguished. Developing methodologies to separate geometric and inertia nonlinearities (and other forms of nonlinearity, such as material nonlinearity) would improve the ability to understand the underlying dynamics of a structure. However, such an exercise may not be helpful for control purposes because the effect of geometric and inertia nonlinearities on the response are qualitatively similar. However, this might be helpful to control in that one has the choice of introducing either geometric or inertia actuation.

4. The parameter estimation procedures of Chapters 5 and 6 involved multiple steps. It would be helpful to simplify the estimation procedure itself, which would reduce the potential for biased errors.

5. Some parameters have quality measures, such as a standard deviation, whereas, other parameters have no quality measures. Further development of quality measures would advance the confidence, or lack of confidence, in the parameter estimates.

Appendix A

Eigensystem Realization Algorithm

In this Appendix, we detail the eigensystem realization algorithm [33], also known as the Ho-Kalman algorithm[29]. This algorithm is a multiple-reference multiple-response technique. Having chosen a sampling interval Δt, we begin our examination of this technique by considering the system of equations

$$v(k+1) = Av(k) + Bu(k) \tag{A.1}$$

$$y(k) = Cv(k) + Du(k) \tag{A.2}$$

where u, v, and y are $q \times 1$ reference or input vector, $2n \times 1$ modal response vector, and $p \times 1$ response or output vector and the p, q, n, and k are the response, reference, mode, and time indices, respectively. By definition, the A, B, C, and D are known as the $2n \times 2n$, $2n \times q$, $p \times 2n$, and $p \times q$ state-space matrices, respectively.

An unit impulse of the qth reference at time index $k = 1$ (corresponding to $t = 0$) results in the impulse-response function $y_{pq,(k)}$ of the pth response. Repeating the procedure, we obtain the response matrices

$$Y_{pq}(k) = \begin{bmatrix} y_{11,(k)} & y_{12,(k)} & \cdots & y_{1q,(k)} \\ y_{21,(k)} & y_{22,(k)} & \cdots & y_{2q,(k)} \\ \vdots & \vdots & \ddots & \vdots \\ y_{p1,(k)} & y_{p2,(k)} & \cdots & y_{pq,(k)} \end{bmatrix} \tag{A.3}$$

The response matrices can then be compactly expressed as

$$Y_{pq}(k) = [C][A]^{k-1}[B] + [D]\delta_0 \tag{A.4}$$

where δ_0 is one at time $k = 1$ and zero otherwise. Here, we place the special requirement that A is diagonal. For diagonal A, C and B are called the mode shapes and initial modal amplitudes, respectively, and D is called the initial pulse amplitudes. If the form of the response is either receptance or mobility, then D can be set to a null matrix. Conversely, if the form of the response is accelerance, then D can not be neglected, in general. The problem of ERA is to construct A, B, C, D with the smallest dimension, called a minimum realization, such that Equation (A.4) holds for all k. The sizes of p and q are the number of response and reference measures. However, the size $2n$ needs not be related to p or q.

We accomplish our task by considering the sum of the experimental data in the $r \times s$ *block* matrix ($rp \times sq$ matrix)

$$H_{rs}(k-1) = \begin{bmatrix} Y_{pq}(k) & Y_{pq}(k+1) & \dots & Y_{pq}(k+s-1) \\ Y_{pq}(k+1) & Y_{pq}(k+2) & \dots & Y_{pq}(k+s) \\ \vdots & \vdots & \ddots & \vdots \\ Y_{pq}(k+r-1) & Y_{pq}(k+r) & \dots & Y_{pq}(k+s+r-3) \end{bmatrix} \tag{A.5}$$

also called the generalized Hankel matrix whose entries are matrices themselves, explained by the term *block*. The choices of the integer values for s and r are arbitrary. However, the smallest dimension of the block Hankel matrix must be equal to or greater than $2n$. One rule of thumb is to set s equal to the smallest integer greater than or equal to $(4n/q)$ and r equal to $N - k - s + 3$; which is a reasonable, but not necessarially an optimal choice [17].

The matrix $H_{rs}(k-1)$ can be returned to the response matrix according to

$$Y_{pq}(k) = E_p^T H_{rs}(k-1) E_q \tag{A.6}$$

where $E_p^T = [I_p, \emptyset_p, \dots, \emptyset_p]_{p \times rp}$ and I_p and $\emptyset_p$ are identity and null matrices of order p, respectively. Similarly, $E_q^T = [I_q, \emptyset_q, \dots, \emptyset_q]_{q \times sq}$.

The zero-lag block matrix is resolved using singular-value decomposition; that is,

$$H_{rs}(1) = [P|P_0] \begin{bmatrix} [\backslash \not{D} \backslash] & \emptyset \\ \emptyset & [\backslash \not{D}_0 \backslash] \end{bmatrix} \left[\begin{array}{c} Q^T \\ \hline Q_0^T \end{array}\right]$$
$$\approx [P][\backslash \not{D} \backslash][Q]^T \tag{A.7}$$

where the augmented matrices on the right-hand side are $rp \times sq$, $sq \times sq$, and $sq \times sq$ from left to right when $rp \geq sq$. However, if the dynamics of a limited bandwidth process are dominated by n so-called normal modes or complex ones, then only $2n$ singular values and vectors are physically significant. By advocacy, the smallest singular values are truncated. One speaks of $\not{D}$ as the significant singular values, and one speaks of P and Q as the significant left and right singular vectors, respectively.

Then, the system eigenvalues can be uncovered by finding A. It follows from Equations (A.4), (A.6), and (A.7) that

$$H_{rs}(2) = P \not{D}^{1/2} \tilde{A} \not{D}^{1/2} Q^T \tag{A.8}$$

where $\tilde{A}$ is given within a rotation of A by $\tilde{A}\psi = \psi A$. Hence,

$$\tilde{A} = \not{D}^{-1/2} P^T H_{rs}(2) Q \not{D}^{-1/2} \tag{A.9}$$

$$\psi^{-1}[\not{D}^{-1/2} P^T H_{rs}(2) Q \not{D}^{-1/2}]\psi = [\backslash A \backslash] \tag{A.10}$$

and the matrix A is given as $[\backslash z_1 \ldots z_{2n} \backslash]$ in the desired diagonal form. The z-plane roots z_k are equivalent to the system poles

$$\lambda_k = \frac{1}{2\pi\Delta t} \ln(z_k) \tag{A.11}$$

in cycles per second or Hz, or

$$\lambda_k = \frac{1}{\Delta t} \ln(z_k) \tag{A.12}$$

in radians per second.

Subsequently, the mode shapes and initial modal amplitudes are determined by *designing* the two identity matrices

$$\left[\not{D}^{1/2} \psi \psi^{-1} \not{D}^{-1/2} P^T P\right] = I_{2n}$$
$$\left[Q^T Q \not{D}^{-1/2} \psi A A^{-1} \psi^{-1} \not{D}^{1/2}\right] = I_{2n}$$

where we used the property that P and Q are self-orthogonal ($P^TP = I, Q^TQ = I$), which does not generally extend to PP^T or QQ^T. Inserting these matrices into the right-hand side of Equation (A.8) produces

$$P\left[\mathbb{D}^{1/2}\psi\psi^{-1}\mathbb{D}^{-1/2}P^TP\right]\mathbb{D}^{1/2}\tilde{A}\mathbb{D}^{1/2}\left[Q^TQ\mathbb{D}^{-1/2}\psi AA^{-1}\psi^{-1}\mathbb{D}^{1/2}\right]Q^T$$

Then, Equations (A.8), (A.10), (A.4), and (A.6) provide

$$\left[E_p^TP\,\mathbb{D}^{1/2}\psi\right]\left[\backslash z\backslash\right]\left[A^{-1}\psi^{-1}\,\mathbb{D}^{1/2}Q^TE_q\right] = [C][\backslash A\backslash][B] \tag{A.13}$$

Finally, substituting Equations (A.4), (A.10), and (A.13) into Equation (A.6) for $k = 1$ results in

$$[D] = E_p^TH_{rs}(0)E_q - [B][C] \tag{A.14}$$

Equations (A.10), (A.13), and (A.14) represent the basic implementation of the eigensystem realization algorithm, thereby providing the poles, mode shapes, initial modal amplitudes, and initial pulse amplitudes.

Appendix B

Residue Conversion

In this appendix, we detail how to convert the residue parameters in the receptance, mobility, and accelerance forms of the impulse-response function for the underdamped single-degree-of-freedom and normal mode cases from one another. The receptance, mobility, and accelerance impulse-response functions are defined, respectively, as the displacement, velocity, and acceleration response of the system to an unit impulse applied at time $t = 0$.

We detail this procedure because it is helpful when the observed system response is not in the same form as the analytic model. However, similar discussions can be found in many introductory texts on ordinary-differential equations. A summary is provided in Table B.

We consider the system

$$\ddot{v} + \frac{c}{m}\dot{v} + \frac{k}{m}v = \frac{1}{m}u(t) \tag{B.1}$$

where u and v denote the excitation and system displacement, respectively. The initial conditions are

$$u(t) = \delta_0 \tag{B.2}$$

$$v = 0 \text{ for all } t < 0 \tag{B.3}$$

$$\dot{v} = 0 \text{ for all } t < 0 \tag{B.4}$$

where δ_0 denotes the Dirac delta function applied at time $t = 0$. When $c < 2\sqrt{km}$, also

known as the underdamped case, the system poles of the homogeneous part of Equation (B.1) are the complex conjugate pair

$$\begin{aligned}\{\lambda, \lambda^*\} &= -\frac{c}{2m} \pm \sqrt{\frac{c^2}{4m^2} - \frac{k}{m}} \\ &= -\zeta\omega \pm j\omega\sqrt{1-\zeta^2}\end{aligned} \tag{B.5}$$

where the "*", ω , and ζ denote the complex conjugate operator, the damped natural frequency, and the damping ratio, respectively. We suppose that

$$v(t) = j\frac{1}{2}u_0 a \exp[\lambda t] + cc \tag{B.6}$$

where u_0 is the Heaviside function applied at time $t = 0$, $j = \sqrt{-1}$, a is a real-valued constant that needs to be determined, and cc denotes the complex conjugate of the preceding terms. By taking the time derivative of Equation (B.6),we obtain

$$\begin{aligned}\dot{v}(t) &= j\frac{1}{2}\delta_0 a \exp(\lambda t) + j\frac{1}{2}u_0 a\lambda \exp(\lambda t) + cc \\ &= j\frac{1}{2}u_0 a\lambda \exp(\lambda t) + cc\end{aligned} \tag{B.7}$$

which implies that the initial velocity $\dot{v}(0+)$ is $-a\omega\sqrt{1-\zeta^2}$. Subsequently, taking the time derivative of Equation (B.7), we obtain

$$\begin{aligned}\ddot{v}(t) &= j\frac{1}{2}\delta_0 a\lambda \exp(\lambda t) + j\frac{1}{2}u_0 a\lambda^2 \exp(\lambda t) + cc \\ &= -\frac{1}{2}\delta_0 a\omega\sqrt{1-\zeta^2} + j\frac{1}{2}u_0 a\lambda^2 \exp(\lambda t) + cc\end{aligned} \tag{B.8}$$

Substituting Equations (B.6)-(B.8) into Equation (B.1) and examining the response at time $t = 0$, we have

$$a = -\frac{1}{m\omega\sqrt{1-\zeta^2}} \tag{B.9}$$

It follows from Equations (B.6)-(B.8) that one can transform a residue estimate obtained from one form of the response into another, when required. Let the receptance, mobility, and accelerance forms of the impulse-response function be expressed as $u_0 A \exp[\lambda t] + cc$, $u_0 B \exp[\lambda t] + cc$, and $u_0 C \exp[\lambda t] + cc + D\delta_0$, respectively. Then, a summary of these is provided in Table B.

Table B.1: Residue conversion

From	To	Multiply by
A	B	λ
A	C	λ^2
A	D	$2\omega\sqrt{1-\zeta^2}$
B	A	$1/\lambda$
B	C	λ
B	D	$2\omega\sqrt{1-\zeta^2}/\lambda$
C	A	$1/\lambda^2$
C	B	$1/\lambda$
C	D	$2\omega\sqrt{1-\zeta^2}/\lambda^2$

Appendix C

Auto-Regressive Moving-Average Technique

This appendix explains why one might not want to use the classical auto-regressive moving-average (ARMA) technique to uncover the nonlinear parameters of a system undergoing a principal parametric resonance. However, ARMA is a very popular and useful linear parameter estimation technique [53]. In fact, the circular-hyperbolic decomposition of Chapter 4 is a special case of ARMA, where the MA terms are neglected and the AR terms are constrained. ARMA encompasses an extremely broad field of study in signal processing. A comprehensive discussion of ARMA is beyond our scope. However, we note briefly that there are several specialized versions of ARMA that have been used successfully to uncover nonlinear system parameters; the list includes NARMA, NARMAX, and the work of Yasuda [87, 88, 89, 90]. This appendix only addresses the question: Why should not one use classical ARMA to uncover the nonlinear system parameters of a system undergoing a principal parametric resonance?

In the classical sense, ARMA is an estimation algorithm for linear systems. Some have applied ARMA techniques to obtain linearized parameters for observed nonlinear system responses. Such an application would be akin to our exercise in Chapter 2 of obtaining

linearized frequency and damping estimates as a function of the modal response amplitude.

In Chapter 2, we examine the nonlinear response of a two-mass structure undergoing primary resonance. In Chapter 5, we examine the nonlinear response of the same structure undergoing principal parametric resonance. In Chapter 2, we at least would have a chance to uncover some useful information from ARMA. In Chapter 5, we are simply unable to obtain an understanding of the input-output relation using ARMA. Why?

By definition [53], the ARMA model is

$$\sum_{k=0}^{n} \alpha_k v(i+k) = \sum_{k=0}^{m} \beta_k u(i+k), \text{ for all } i \in \{1, 2, ..., N\} \tag{C.1}$$

where u, v, α, β, n, and m are an input, an output, the auto-regressive parameters, the moving-average parameters, the auto-regressive model order, and the moving-average model order, respectively. An important assumption involved with the ARMA model is that the input and output are correlated in the sense of a second-order cummulant. In other words, the expected value $E[u(i+k)v(i+\ell)]$ for the product of $u(i+k)$ and $v(i+\ell)$ is zero for all k and ℓ. In the case of primary resonance, the input and output are indeed correlated. However, in the case of principal parametric resonance, the input and output are generally uncorrelated.

In Figure C.1, we observe the input (excitation) and output (second-mode acceleration response) in primary resonance. When estimating the ARMA parameters, we begin by forming two Hankel matrices

$$V(i,k) = \begin{bmatrix} v(1) & v(2) & \dots & v(n+1) \\ v(2) & v(3) & \dots & v(n+2) \\ \vdots & \vdots & \dots & \vdots \\ v(N) & v(N+1) & \dots & v(N+n) \end{bmatrix} \tag{C.2}$$

$$U(i,k) = \begin{bmatrix} u(1) & u(2) & \dots & u(m+1) \\ u(2) & u(3) & \dots & u(m+2) \\ \vdots & \vdots & \dots & \vdots \\ u(N) & u(N+1) & \dots & u(N+m) \end{bmatrix} \tag{C.3}$$

from which we develop the paired Hankel matrix

$$H(i,k) = [V(1:N, 1:n+1)|U(1:N, 1:m+1)] \tag{C.4}$$

In the noiseless case

$$\left\{ \begin{array}{c} \alpha_1 \\ \alpha_2 \\ \vdots \\ \alpha_n \\ \hline \beta_0 \\ \beta_1 \\ \vdots \\ \beta_m \end{array} \right\} = -H(:, 2:n+m+2)^{+} H(:,1) \tag{C.5}$$

where $\alpha_0 = 1$ and $[\ \ ]^{+} \equiv [[\ \ ]^T[\ \ ]]^{-1}[\ \ ]^T$. Obviously, the columns of H must be correlated to obtain meaningful parameter estimates. In Figure C.2, we show the correlation matrix, defined in the usual sense for the columns of H, which demonstrates that the columns generally have some correlation. We note that the correlation among all of the columns does not need to be unity, some may even be zero. Rather, there should be correlation in an overall sense.

On the other hand, in Figure C.3, we observe the input (excitation) and output (second-mode acceleration response), for the same structure as before, to a principal parametric resonance. In Figure C.4, we observe that the input and output are largely uncorrelated. The correlation between the input and output is not significantly different from zero. However, the input is well correlated with itself and the output is well correlated with itself. Noise is not the reason for the lack of correlation between the input and output. There is very little noise ($S/N \cong 80dB$).

The principal parametric resonance emphasizes the nonlinearity of the structure. In Chapter 5, we specifically choose to exploit principal parametric resonance for this reason. ARMA does not exploit this emphasis and provides a poor description of the system dynamics. We could use an AMRA model to describe the input and output signals. But, ARMA

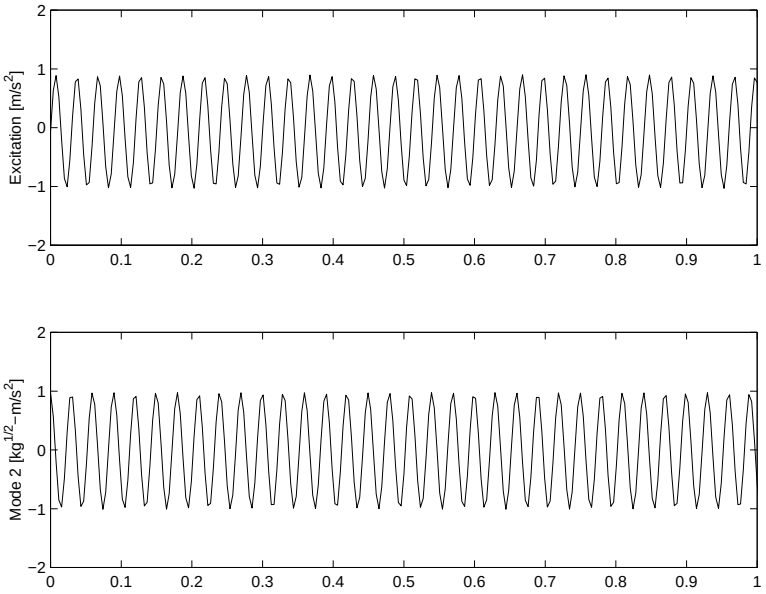

Figure C.1: Time history of excitation and second-mode response to a primary resonance

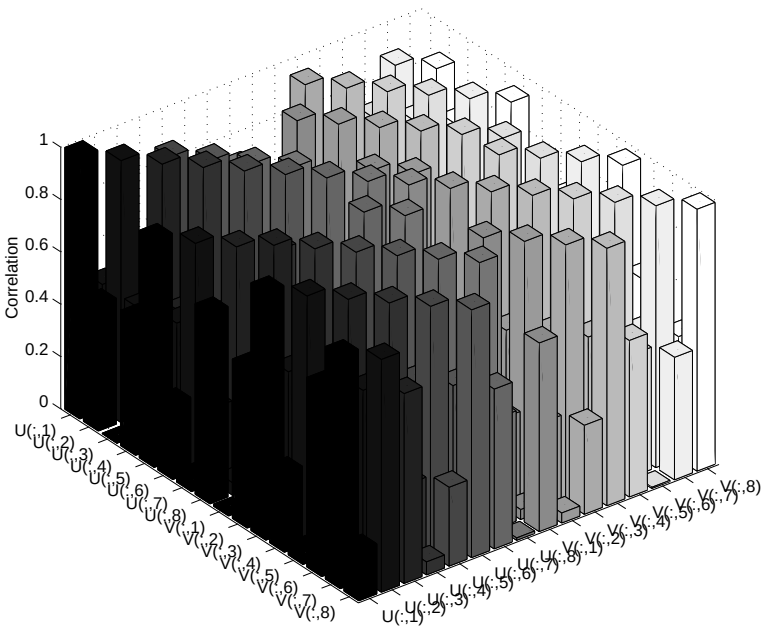

Figure C.2: Correlation of delayed excitation and mode-two response to a primary resonance

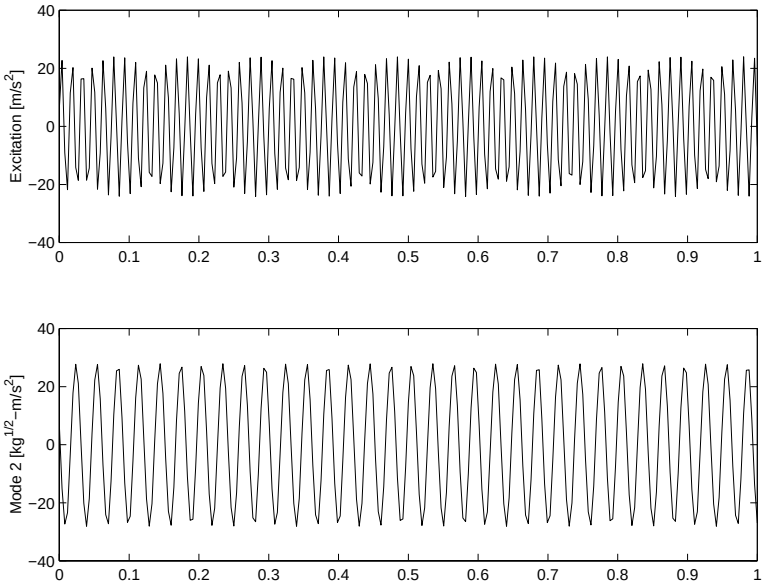

Figure C.3: Time history of excitation and second-mode response to a principal parametric resonance

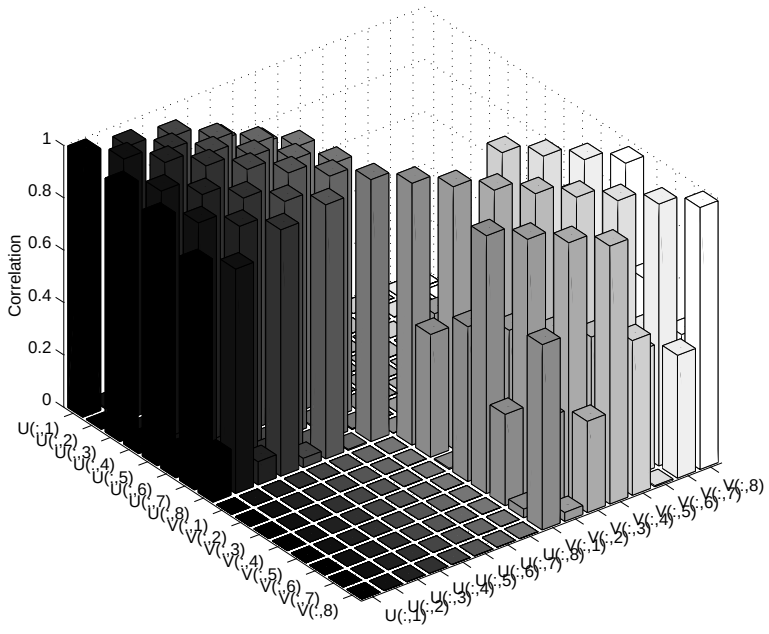

Figure C.4: Correlation of delayed excitation and mode-two response to a principal parametric resonance

would describe the output based on the output alone. ARMA would also describe the input based on the input alone. In this particular application of ARMA, our ability to predict and describe the input-output relationship would be lost.

Appendix D

ANOVA Considerations

In this appendix, we test the statistical significance of the model parameters in Equations (6.49)-(6.51). To accomplish this task, we use the partial F test, which is a standard multivariable method. We select the critical value of 0.05, which implies that the probability of an incorrect decision is 5% or less.

In order to establish statistical significance, we set each model parameter equal to zero individually and examine the variance. We compare the variance when a model parameter is included in the model versus when a model parameter is set equal to zero. If the variance does not change significantly, then the estimate of the model parameter is not statistically significant. The F test is our metric of significance. This general methodology is referred to as *added-last* analysis of variance (ANOVA).

In Table D.1, we summarize the models used in our consideration of the model parameter in Equation (6.49). In Table D.2, we summarize the computations required for the regression sum of squares. Here, the details of ANOVA procedures are brief. The book by Kleinbaum et al. [39] is recommended for further details of multivariable statistics. In Table D.3, we summarize the result of the F test for the results from Equation (6.49). For example, the F

test for $\frac{3\omega_1^2\mu_{13}a_1^3}{8\mu_{11}}$ is calculated according to

$$F = \frac{\text{SS}(\frac{3\omega_1^2\mu_{13}a_1^3}{8\mu_{11}}|\frac{\Gamma_5 F a_2 \sin\gamma}{\omega_1\mu_{11}}, \frac{\Gamma_6 F a_2 \cos\gamma}{\omega_1\mu_{11}})/1}{\text{SS(Residual)}/(307-1)} \tag{D.1}$$

If the value of the F test is greater than the critical value, then the associated model parameter is considered to be statistically significant. If the value of the F test is less than the critical value, then the associated model parameter is considered to be statistically insignificant. We find that all of the model parameters obtained from Equation (6.49) are statistically significant based on the results of the F test summarized in Table D.3.

In Table D.4, we summarize the results of the F test for the model parameters in Equations (6.50). We find that all of the model parameters obtained from Equation (6.50) are statistically significant based on the results of the F test summarized in Table D.4.

In Table D.5, we summarize the results of the F test for the model parameters in Equations (6.51). We find that not all of the model parameters obtained from Equation (6.51) are statistically significant. The model parameters $\omega_2\Gamma_2 + \omega_1\Gamma_9$ and $\omega_2\Gamma_3 + \omega_1\Gamma_8$ fail to demonstrate statistical significance. However, the remaining model parameters are found to have statistical significance.

In Table D.5, we detail the results of an additional F test. We simultaneously set $\omega_2\Gamma_2 + \omega_1\Gamma_9$ and $\omega_2\Gamma_3 + \omega_1\Gamma_8$ equal to zero in order to determine if their combined effect is significant or not. The results demonstrate that the combination of $\omega_2\Gamma_2 + \omega_1\Gamma_9$ and $\omega_2\Gamma_3 + \omega_1\Gamma_8$ is statistically significant. It turns out that a_1/a_2 is almost fixed, which can be observed in Figures 6.2 and 6.3. However, eliminating γ from Equations (6.30) and (6.32) demonstrates that a_1/a_2 is not constant. Here, $a_1a_2^3$ and $a_1^3a_2$ can not be statistically distinguished, which is the root of our dilemma.

Table D.1: Models used for partial F test of Equation (6.49) parameters.

Model No.	Model	SSE
1	$a_1 = -\frac{3\omega_1^2\mu_{13}a_1^3}{8\mu_{11}} - \frac{\Gamma_5 F a_2 \sin\gamma}{\omega_1\mu_{11}} - \frac{\Gamma_6 F a_2 \cos\gamma}{\omega_1\mu_{11}} + E$	1.246×10^{-6}
2	$a_1 = -\frac{\Gamma_5 F a_2 \sin\gamma}{\omega_1\mu_{11}} - \frac{\Gamma_6 F a_2 \cos\gamma}{\omega_1\mu_{11}} + E$	1.309×10^{-6}
3	$a_1 = -\frac{3\omega_1^2\mu_{13}a_1^3}{8\mu_{11}} - \frac{\Gamma_6 F a_2 \cos\gamma}{\omega_1\mu_{11}} + E$	1.051×10^{-3}
4	$a_1 = -\frac{3\omega_1^2\mu_{13}a_1^3}{8\mu_{11}} - \frac{\Gamma_5 F a_2 \sin\gamma}{\omega_1\mu_{11}} + E$	2.24×10^{-6}

Table D.2: Computation for regression sum of squares.

Parameter	Computation	Regression SS
$\frac{3\omega_1^2\mu_{13}a_1^3}{8\mu_{11}}$	SSE(2)-SSE(1)	63.0×10^{-9}
$\frac{\Gamma_5 F a_2 \sin\gamma}{\omega_1\mu_{11}}$	SSE(3)-SSE(1)	1.050×10^{-3}
$\frac{\Gamma_6 F a_2 \cos\gamma}{\omega_1\mu_{11}}$	SSE(4)-SSE(1)	993×10^{-9}

Table D.3: ANOVA table for added-last F test of Equation (6.49) parameters: ** Exceeds 0.05 critical value of 3.87 for F with 1 numerator and 306 denominator degrees of freedom.

Source	DOF	SS	F	R^2
$\frac{3\omega_1^2\mu_{13}a_1^3}{8\mu_{11}} \mid \frac{\Gamma_5 F a_2 \sin\gamma}{\omega_1\mu_{11}}, \frac{\Gamma_6 F a_2 \cos\gamma}{\omega_1\mu_{11}}$	1	63.0×10^{-9}	15.48 **	0.9997
$\frac{\Gamma_5 F a_2 \sin\gamma}{\omega_1\mu_{11}} \mid \frac{3\omega_1^2\mu_{13}a_1^3}{8\mu_{11}}, \frac{\Gamma_6 F a_2 \cos\gamma}{\omega_1\mu_{11}}$	1	1.050×10^{-3}	258×10^3 **	
$\frac{\Gamma_6 F a_2 \cos\gamma}{\omega_1\mu_{11}} \mid \frac{3\omega_1^2\mu_{13}a_1^3}{8\mu_{11}}, \frac{\Gamma_5 F a_2 \sin\gamma}{\omega_1\mu_{11}}$	1	993×10^{-9}	244 **	
Residual	307	1.246×10^{-6}		
Total	310	4.68×10^{-3}		

Table D.4: ANOVA table for added-last F test of Equation (6.50) parameters: ** Exceeds 0.05 critical value of 3.87 for F with 1 numerator and 306 denominator degrees of freedom.

Source	DOF	SS	F	R^2
$\frac{3\omega_2^2\mu_{23}a_2^3}{8\mu_{22}} \mid \frac{\Gamma_{11}Fa_1\sin\gamma}{\omega_2\mu_{22}}, \frac{\Gamma_{12}Fa_1\cos\gamma}{\omega_2\mu_{22}}$	1	12.42×10^{-6}	1148 **	0.9997
$\frac{\Gamma_{11}Fa_1\sin\gamma}{\omega_2\mu_{22}} \mid \frac{3\omega_2^2\mu_{23}a_2^3}{8\mu_{22}}, \frac{\Gamma_6Fa_1\cos\gamma}{\omega_2\mu_{22}}$	1	2.26×10^{-3}	209×10^3 **	
$\frac{\Gamma_{12}Fa_1\cos\gamma}{\omega_2\mu_{22}} \mid \frac{3\omega_2^2\mu_{23}a_2^3}{8\mu_{22}}, \frac{\Gamma_{11}Fa_1\sin\gamma}{\omega_2\mu_{22}}$	1	19.44×10^{-6}	1797 **	
Residual	307	3.32×10^{-6}		
Total	310	10.77×10^{-3}		

Table D.5: ANOVA table for added-last F test of balanced Equation (6.51) parameters: ** Exceeds 0.05 critical value of 3.87 for F with 1 numerator and 304 denominator degrees of freedom or 3.03 for F with 2 numerator and 304 denominator degrees of freedom, as appropriate.

Source	DOF	SS	F	R^2
$\omega_2\Gamma_1 + \omega_1\Gamma_7 \mid \omega_2\Gamma_2 + \omega_1\Gamma_9, \omega_2\Gamma_3 + \omega_1\Gamma_8, \omega_2\Gamma_4 + \omega_1\Gamma_{10}, \Gamma_5$	1	52.6×10^-6	3.88 **	0.996
$\omega_2\Gamma_2 + \omega_1\Gamma_9 \mid \omega_2\Gamma_1 + \omega_1\Gamma_7, \omega_2\Gamma_3 + \omega_1\Gamma_8, \omega_2\Gamma_4 + \omega_1\Gamma_{10}, \Gamma_5$	1	24.5×10^-6	1.808	
$\omega_2\Gamma_3 + \omega_1\Gamma_8 \mid \omega_2\Gamma_1 + \omega_1\Gamma_7\omega_2\Gamma_2 + \omega_1\Gamma_9, \omega_2\Gamma_4 + \omega_1\Gamma_{10}, \Gamma_5$	1	10.30×10^-6	0.761	
$\omega_2\Gamma_2 + \omega_1\Gamma_9, \omega_2\Gamma_3 + \omega_1\Gamma_8 \mid \omega_2\Gamma_1 + \omega_1\Gamma_7\omega_2\Gamma_4 + \omega_1\Gamma_{10}, \Gamma_5$	2	6.90×10^-3	255 **	
$\omega_2\Gamma_4 + \omega_1\Gamma_{10} \mid \omega_2\Gamma_1 + \omega_1\Gamma_7, \omega_2\Gamma_2 + \omega_1\Gamma_9, \omega_2\Gamma_3 + \omega_1\Gamma_8, \Gamma_5$	1	920×10^-6	67.9 **	
$\Gamma_5 \mid \omega_2\Gamma_1 + \omega_1\Gamma_7, \omega_2\Gamma_2 + \omega_1\Gamma_9, \omega_2\Gamma_3 + \omega_1\Gamma_8, \omega_2\Gamma_4 + \omega_1\Gamma_{10}$	1	17.76×10^-3	1311 **	
Residual	305	4.12×10^-3		
Total	310	1.000		

Bibliography

[1] R.J. Allemang and D.L. Brown. A correlation coefficient for modal vector analysis. In *International Modal Analysis Conference*, pages 110–116, Orlando, Florida, 1982.

[2] R.E.A. Arndt, D.F. Long, and M.N. Glauser. The proper orthogonal decomposition of pressure fluctuations surrounding a turbulent jet. *Journal of Fluid Mechanics*, 340:1–33, 1997.

[3] N. Aubry, W-Y. Lian, and E.S. Titi. Preserving symmetries in the proper orthogonal decomposition. *SIAM Journal of Scientific Computing*, 14:483–505, 1993.

[4] J.-G.L. Béliveau. *Structural Dynamics Course Notes*. The University of Vermont, Department of Civil and Environmental Engineering, 1996.

[5] G. Berkooz. An observation on the probability density equations, or, when do simulations reproduce statistics. *Nonlinearity*, 7:313–328, 1994.

[6] G. Berkooz, J. Elezgaray, P. Holmes, J. Lumley, and A. Poje. The proper orthogonal decomposition, wavelets and modal approaches to the dynamics of coherent structures. *Applied Scientific Research*, 53:321–338, 1994.

[7] J.P. Bonnet, D.R. Cole, M.N. Glauser, and L.S. Ukeiley. Stochastic estimation and proper orthogonal decomposition: complementary technique for identifying structure. *Experiments in Fluids*, 17:307–314, 1994.

[8] K. Carney, I. Yunis, K. Smith, and C.Y. Peng. Nonlinear dynamic behavior in the cassini spacecraft modal survey. In *International Modal Analysis Conference*, pages 811–817, Orlando, Florida, 1997.

[9] J-C. Chen and M. Trubert. Galileo modal test and pre-test analysis. In *International Modal Analysis Conference*, pages 796–802, Orlando, Florida, February 1984.

[10] K.M. Cipolla, A. Liakopoulos, and D.O. Rockwell. Quantitative imaging in proper orthogonal decomposition of flow past a delta wing. *AIAA Journal*, 36:1247–1255, 1998.

[11] J.P. Cusumano, M.T. Sharkady, and B.W. Kimble. Experimental measurements of dimensionality and spatial coherence in the dynamics of a flexible-beam impact oscillator. *Philosophical Transactions of the Royal Society of London A*, 347:421–438, 1994.

[12] J. Delville, L. Ukiley, L. Cordier, J.P. Bonnet, and M. Glauser. Examination of large-scale structures in a turbulent plane mixing layer. Part I. proper orthogonal decomposition. *Journal of Fluid Mechanics*, 391:91–122, 1999.

[13] J.P. den Hartog. *Mechanical Vibration*. Dover, New York, 1985.

[14] A. Einstein. *Relativity, The Special and The General Theory*. Crown Publishers, New York, 1961.

[15] A.A. El-Badawy and A.H. Nayfeh. Nonlinear active control of a parametrically excited structural model of an F-15 tail section. *AIAA Paper no. 2000-1542*, in press.

[16] S.O'F. Fahey and A.H. Nayfeh. Experimental nonlinear identification of a single structural mode. In *International Modal Analysis Conference*, pages 737–745, Orlando, Florida, February 1998.

[17] S.O'F. Fahey and J. Pratt. Time domain modal estimation techniques. *Experimental Techniques*, 22:45–49, 1998.

[18] J. Fung. *Parameter Identification of Nonlinear Systems using Perturbation Techniques and Higher-Order Statistics, MS thesis.* Engineering Science and Mechanics, Virginia Polytechnic Institute and State University, 1998.

[19] J. Fung, M.R. Hajj, A.H. Nayfeh, and S.O'F. Fahey. Damping identification using perturbation techniques and higher-order spectra. In *International Modal Analysis Conference*, Santa Barbara, CA, February 2-5 1998.

[20] H. Goldstein. *Classical Mechanics.* Addison-Wesley, Reading, Massachusetts, 2nd edition, 1980.

[21] G.H. Golub and C.F.Ṽan Loan. *Matrix Computation.* The Johns Hopkins University Press, Baltimore, MD, 3rd edition, 1996.

[22] M.D. Graham, S.L. Lane, and D. Luss. Proper orthogonal decomposition analysis of spatiotemporal temperature patterns. *Journal of Physical Chemistry*, 97:889–894, 1993.

[23] M.D. Graham, J. Peraire, and K.Y. Tang. Optimal control of vortex shedding using low-order models. Part I – open-loop model development. *International Journal for Numberical Methods in Engineering*, 44:945–972, 1999.

[24] H. Gunes, A. Liakopoulos, and R.A. Sahan. Low-dimensional description of oscillatory thermal convection: the small prantl number limit. *Theoretical and Computational Fluid Dynamics*, 9:1–16, 1997.

[25] H.R. Hajj, A.H. Nayfeh, and P. Popovic. Identification of nonlinear system parameters using polyspectral measurements and analysis. In *ASME 15th Biennial Conference on Mechanical Vibration and Noise*, Boston, MA, September 1995.

[26] M.R. Hajj, J. Fung, A.H. Nayfeh, and S.O'F. Fahey. Damping identification using perturbation techniques and higher-order spectra. *Nonlinear Dynamics*, 23:189–203, 2000.

[27] N.H. Hanna and S.A. Tobias. A theory of nonlinear regenerative chatter. *ASME Journal of Engineering Industry*, 96:247–255, 1974.

[28] F.J. Harris. On the use of windows for harmonic analysis with the Discrete Fourier Transform. *Proceedings of IEEE*, 66:51–84, 1978.

[29] B.L. Ho and R.E. Kalman. Effective construction of linear state-variable models from input/output data. In *Proceedings of the Third Annual Allerton Conference on Curcuit and System Theory*, pages 449–459, 1965.

[30] H. Hotelling. The most predictable criterion. *Journal of Educational Psychology*, 26:139–142, 1933.

[31] S.R. Ibrahim and E.C. Mikulcik. A method for the direct identification of vibration parameters from the free response. *Sound & Vibration Bulletin*, 47:183–198, 1977.

[32] R.C. Johnson. *Optimum Design of Mechanical Elements*. Wiley, New York, 1961.

[33] J-N. Juang and R.S. Pappa. An eigensystem realization algorithm for modal parameter identification and model reduction. *Journal of Guidance, Control, and Dynamics*, 8:620–627, 1985.

[34] T.R. Kane and D.A. Levinson. *Dynamics: Theory and Applications*. McGraw-Hill, New York, 1996.

[35] R.K. Kapania and S. Park. Parametric identification of nonlinear structural dynamic systems using time finite element method. *AIAA Journal*, 35:719–726, 1997.

[36] R. Kappagantu and B.F. Feeny. An optimal modal reduction of a system with fractional excitation. *Journal of Sound and Vibration*, 224:863–877, 1999.

[37] S.M. Kay and S.L. Marple. Spectrum analysis – a modern perspective. *Proceedings of IEEE*, 69:1380–1419, 1981.

[38] H. Kikuchi, Y. Tamura, H. Ueda, and K. Hibi. Dynamic wind pressures acting on a tall building model proper orthogonal decomposition (sic). *Journal of Wind Engineering and Industrial Aerodynamics*, 69-71:631–646, 1997.

[39] D.G. Kleinbaum, L.L. Kupper, and K.E. Muller. *Applied Regression Analysis and Other Multivariable Methods*. Duxbury Press, Belmont, CA, 2nd edition, 1988.

[40] V.C. Klema and A.J. Laub. The singular value decomposition: It computation and some applications. *IEEE Transactions on Automatic Control*, AC-25:164–176, 1980.

[41] R. Krauss. *Experimental Identifcation of Nonlinear Systems, MS thesis*. Engineering Science and Mechanics, Virginia Polytechnic Institute and State University, 1998.

[42] R.W. Krauss and A.H. Nayfeh. Experimental nonlinear identification of a single mode of a transversely excited beam. *Nonlinear Dynamics*, 18:69–87, 1999.

[43] E. Kreuzer and O. Kust. Analysis of long torsional springs by proper orthogonal decomposition. *Archive of Applied Mechanics*, 67:68–80, 1996.

[44] K. Krischer, R. Rico-Martinez, I.G. Kevrekidis, H.H. Rotermund, G. Ertl, and J.L. Hudson. Model identification of a spatiotemporally varying catalytic reaction. *American Institute of Chemical Engineers Journal*, 39:89–98, 1993.

[45] K. Kunisch and S. Volkwein. Control of the Burgers equation by a reduced-order approach using proper othogonal decomposition. *Journal of Optimization Theory and Applications*, 102:345–371, 1999.

[46] S.L. Lane, M.D. Graham, and D. Luss. Spatiotemporal temperature patterns during hydrogen oxidation. *American Institute of Chemical Engineers Journal*, 39:1497–1508, 1993.

[47] G-M. Lee. Estimation of non-linear system parameters using higher-order frequency response functions. *Mechanical Systems and Signal Processing*, 11:219–228, 1997.

[48] F. Lembregts, J. Leuridan, L. Zhang, and H. Kanda. Multiple input modal analysis of frequency response functions based on direct parameter identification. In *International Modal Analysis Conference*, Schenectady, NY, 1986.

[49] J.M. Leuridan. *Some Direct Parameter Model Identification Methods Applicable for Multiple Input Modal Analysis*. PhD thesis, The University of Cincinnati, 1984.

[50] M. Link and A. Vollan. Identification of structural system parameters. *Zeitscrift Für Flugwissenschaften und Weltraumforschung*, 2:165–174, 1978.

[51] L.E. Marlvern. *Introduction to the Mechanics of a Continuous Medium*. Prentice-Hall, Englewood Cliffs, New Jersey, 1969.

[52] L. Marple. Spectral line analysis by Pisarenko and Prony methods. In *IEEE International Conference on Acoustics, Speech & Signal Processing*, pages 159–161, 1979.

[53] S.L. Marple. *Digital Spectral Analysis with Applications*. Prentice-Hall, Englewood Cliffs, New Jersey, 1987.

[54] K.G. McConnell. *Vibration Testing: Theory and Practice, Chapter 5*. Wiley, New York, 1995.

[55] L. Meirovitch. *Analytical Methods in Vibrations*. MacMillian, New York, 1971.

[56] K.S. Mohammad, K. Worden, and G.R. Tomlinson. Direct parameter estimation for linear and nonlinear systems. *Journal of Sound and Vibration*, 152:471–499, 1992.

[57] A.H. Nayfeh. *Perturbation Methods*. Wiley, New York, 1973.

[58] A.H. Nayfeh. *Introduction to Perturbation Techniques*. Wiley, New York, 1981.

[59] A.H. Nayfeh. Parametric identification of nonlinear dynamic systems. *Computers & Structures*, 20:487–493, 1985.

[60] A.H. Nayfeh. *Nonlinear Interactions*. John Wiley Interscience, New York, 1999.

[61] A.H. Nayfeh and H.N. Arafat. Nonlinear response of cantilever beam to combination and subcombination resonances. *Shock and Vibration*, 5:277–288, 1998.

[62] A.H. Nayfeh and B. Balachandran. *Applied Nonlinear Dynamics: Analytic, Computational and Experimental Methods*. Wiley, New York, 1995.

[63] A.H. Nayfeh and C-M. Chin. *Perturbation Methods with Mathematica*. Dynamics Press, Virginia, 1999.

[64] A.H. Nayfeh, M.R. Hajj, J. Fung, and S.O'F. Fahey. Characterization and identification of damping and nonlinear system parameters with bispectral analysis. In *ASME Design Engineering Technical Conferences, ASME DETC97/VIB-4407*, Sacramento, CA, September 1997.

[65] A.H. Nayfeh and D.T. Mook. *Nonlinear Oscillations*. Wiley, New York, 1979.

[66] A.H. Nayfeh and I.G. Oh. Nonlinearity coupled pitch and roll motion in the presence of internal resonance; Part I, theory. *International Shipbuilding Progress*, 42:295–324, 1995.

[67] R.S. Pappa. Some statistical performance characteristics of the "ITD" modal identification algorithm. *AIAA Paper No. 82-0768*, pages 1–19, 1982.

[68] V.E. Pisarenko. The retrieval of harmonics from a covariance function. *The Geophysical Journal of the Royal Astronomical Society*, 33:347–366, 1973.

[69] B. Podvin and J. Lumley. A low-dimensional approach for the minimal flow unit. *Journal of Fluid Mechanics*, 362:121–155, 1998.

[70] J.R. Pratt and A.H. Nayfeh. Design and modeling for chatter. *Nonlinear Dynamics*, 19:49–69, 1999.

[71] R. Prony. Essai expérimental et analytique: Sur les lois de la dilatabilité des fluides élastiques et sur celles de la force expansive de la vapeur de l'eau et de la vapeur de l'alkool, à différentes températures. *Journal de l'École Polytechnique, Paris*, 1:24–76, 1795.

[72] L. Pust, F. Peterka, G. Stépán, G.R. Tomlinson, and A. Tondl. Nonlinear oscillation in machines and mechanisms theory. *Mechanism and Machine Theory*, 34:1237–1253, 1999.

[73] B. Ravindra. Comments on on (sic) the physical interpretation of proper orthogonal modes in vibration. *Journal of Sound and Vibration*, 219:189–192, 1999.

[74] D. Rempfer and H.F. Fasel. Evolution of three-dimensional coherent structures in a flat-plate boundary layer. *Journal of Fluid Mechanics*, 260:351–375, 1994.

[75] N. Smaoui and D. Armbruster. Symmetry and the Karhunen-Loève analysis. *SIAM Journal of Scientific Computing*, 18:1526–1532, 1997.

[76] F.R. Spitznogle and A.H. Quazi. Representation and analysis of time-limited signals using a complex exponential algorithm. *Journal of the Acoustical Society of America*, 47:1150–1155, 1970.

[77] S. Sridhar, A.H. Nayfeh, and D.T. Mook. Nonlinear resonance in a class of multi-degree-of-freedom systems. *Journal of the Acoustical Society of America*, 58:113–123, 1975.

[78] D. Stewart and W. Love. A general canonical correlation index. *Psychological Bulliten*, 70:160–163, 1968.

[79] G. Strang. *Linear Algebra and Its Applications*. Academic Press, 2nd edition, 1980.

[80] M.M. Tabaddor. *Nonlinear Vibration of Beam and Multibeam Systems*. PhD thesis, Virginia Polytechnic Institute and State University, 1996.

[81] Y. Tamura, S. Suganuma, H. Kikuchi, and K. Hibi. Proper orthogonal decomposition of random wind pressure field. *Journal of Fluids and Structures*, 13:1069–1095, 1999.

[82] G.E.B. Tan and S. Pellegrino. Non-linear dynamic identification: An application to prestressed cable structures. *Journal of Sound and Vibration*, 208:33–45, 1997.

[83] S.P. Timoshenko. *History of Strength of Materials*. McGraw-Hill, New York, 1953.

[84] Y. Uematsu, M. Yamada, A. Inoue, and T. Hongo. Wind loads and wind-induced dynamic behavior of a single-layer laticed dome. *Journal of Wind Engineering and Industrial Aerodynamics*, 66:227–248, 1997.

[85] G.N. Vanderplaats. *Numerical Optimization Techniques for Engineering Design.* McGraw-Hill, New York, 1984.

[86] Y. Yang and S.R. Ibrahim. A nonparametric identifaction technique for a variety of discrete nonlinear vibrating systems. *Journal of Vibration, Acoustics, Stress, and Reliability Design*, 107:60–66, 1985.

[87] K. Yasuda, K. Kamiya, and M. Komakine. Experimental identification technique of vibrating structure with geometrical nonlinearity. *Journal of Applied Mechanics*, 64:275–280, 1997.

[88] K. Yasuda and S. Kawamura. A nonparametric identification technique for nonlinear vibratory systems (proposition of the technique). *JSME International Journal*, 32:365–372, 1989.

[89] K. Yasuda, S. Kawamura, and K. Watanabe. Identification of nonlinear multi-degree-of-freedom systems (identification under noisy measurements). *JSME International Journal*, 31:502–509, 1988.

[90] K. Yasuda and J. Ye. A nonparametric identification technique in time domain for multi-degree-of-freedom vibratory systems. *JSME International Journal*, 36:9–16, 1993.

VITA

Sean O'Flaherty Fahey was born on December 4, 1972 in Burlington, Vermont. He earned his Bachelor of Science and Master of Science in Mechanical Engineering from the University of Vermont in 1994 and 1996, respectively. He worked briefly as an acoustic test engineer for the Electric Boat Corporation of Groton, Connecticut. In January of 1999, he decided to pursue the degree of Doctor of Philosophy in Engineering Mechanics at Virginia Tech under the supervision of Dr. Ali H. Nayfeh. He is currently a project engineer with CSA Engineering, Inc. of Mountain View, California.